Bachelor Thesis

Degree Project in
Geology 30 hp

Structural Analysis and Kinematics Across a Nappe Contact near Livigno (Italy)

Claudio Rudolf Gruler

Stockholm 2026

Department of Geological Sciences
Stockholm University

SE-106 91 Stockholm

.

Structural Analysis and Kinematics Across a Nappe Contact near Livigno (Italy)

Abstract

This thesis presents a structural and kinematic analysis of a nappe contact near Livigno, Italy, within the Ortler-Campo nappe complex. The Ortler Nappe was thrust over Campo/Languard enabling the Albula-Zebrù movement zone (a reactivated crustal discontinuity). Microscopic, mesoscopic, and structural analysis reveals a dominant **Top-to-the-NW/West** tectonic transport direction (reverse kinematics).

- **Kinematic indicators** such as S-C Fabrics, asymmetric and rotated porphyroclasts reveal a consistent angular relationship that confirms west-directed thrusting.
- **Structural Convergence:** Systematic measurements across the nappes reveal that fold axes and lineations progressively rotate toward the final Top-to-the-NW/West transport. The westward transport extends into the footwall units.
- **Nappe Contact Intensity:** This direction of fold axes and lineations reaches maximum convergence towards the final transport direction at the Ortler/Languard Nappe contact, showing stronger rotation just below the Nappe contact – possibly due to high strain in this area.
- **Fold Axis Determination**: Average lineation (109°/6°) close to the Ortler/Languard nappe contact is a good indicator of the transport directions. Kinematic modeling reveals an ENE-trending fold axis (77°/16°), oriented at an angle of 32° to the lineation. In low-strain environments, these features are typically 90° apart. The reduction to 32° indicates significant rotation of the fold axis toward the transport direction, signaling a regime of high stress and high strain.

Petrographic analysis indicates that tectonic transport occurred under lower greenschist-facies conditions. The deformation is characterized by dynamic quartz recrystallization and the stability of Mg- and Fe-rich chlorite and feldspar. The occurrence of prograde biotite in only one thin section suggests that temperatures generally remained close to the biotite-in isograd. The temperature range is therefore approximately 280 - 400 °C. Overprinting foliations and opposing shear indicators suggest polyphase deformation.

(**Cover image:** Raibl-beds located in the study area near Livigno (Italy)).

Table of Contents

1. Introduction

The Alpine orogen is a young and well-studied mountain belt formed by the convergence of the African (Adriatic) and Eurasian plates (Schmid et al., 2004). The complex tectonic architecture of this region has been recently mapped and synthesized in detail by Bernoulli et al. (2024), providing an updated framework for understanding nappe distributions and structural domains in Switzerland and adjacent areas. The orogen preserves a complex history of crustal deformation, plate interactions, and rheological responses of rocks under varying pressure-temperature-strain (P–T–ε) conditions (Dewey and Bird, 1970; Fossen, 2016). A key structural feature of collisional orogens such as the Alps is the presence of nappes, large thrust sheets transported far from their original position (Pfiffner, 2024). These nappe systems record the imprint of both compressional emplacement and subsequent overprinting processes such as post-collisional extension or strike-slip reactivation.

Nappe contacts are tectonically significant thrust surfaces along which large displacements occur **(Figure 1)**. They function as major boundaries separating distinct crustal domains with different lithological and metamorphic histories. The geometry and kinematics of these contacts provide insights into the evolution of tectonic processes. They record not only nappe emplacement mechanisms but also interactions between successive deformation phases. Mapping and analyzing deformation structures across such tectonic boundaries can therefore provide insights into the broader evolution of orogenic belts (Boyer and Elliott, 1982; Schmid et al., 2004).

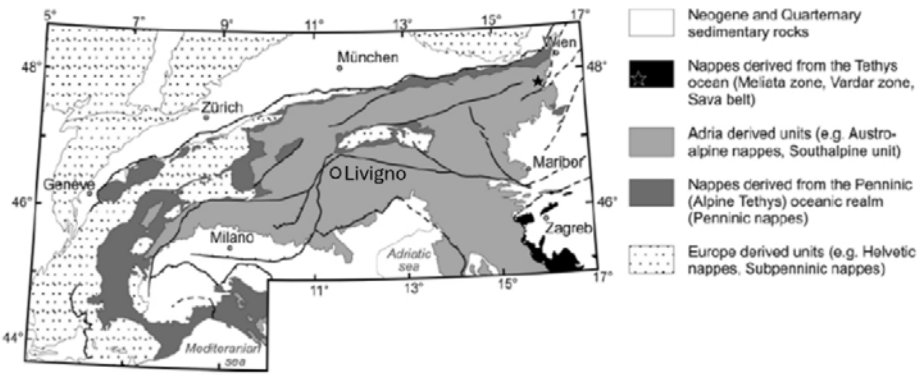

Figure 1: *Tectonic map and paleographic units of the European alps (Schmid et al., 2004), modified after (Schuster et al., 2013).*

This study focuses on a region in the Eastern Central Alps, at the Swiss Italian border near the town of Livigno. The study area is situated within the Austroalpine nappe stack, where upper crustal units were thrust over deeper domains during the Alpine orogeny (Froitzheim et al., 1994; Schmid et al., 2004). The mapping area is part of the Ortler-Campo nappe complex, one of the principal nappe systems of the middle to upper Austroalpine domain (Bigi et al., 1990) **(Figure 2)**.

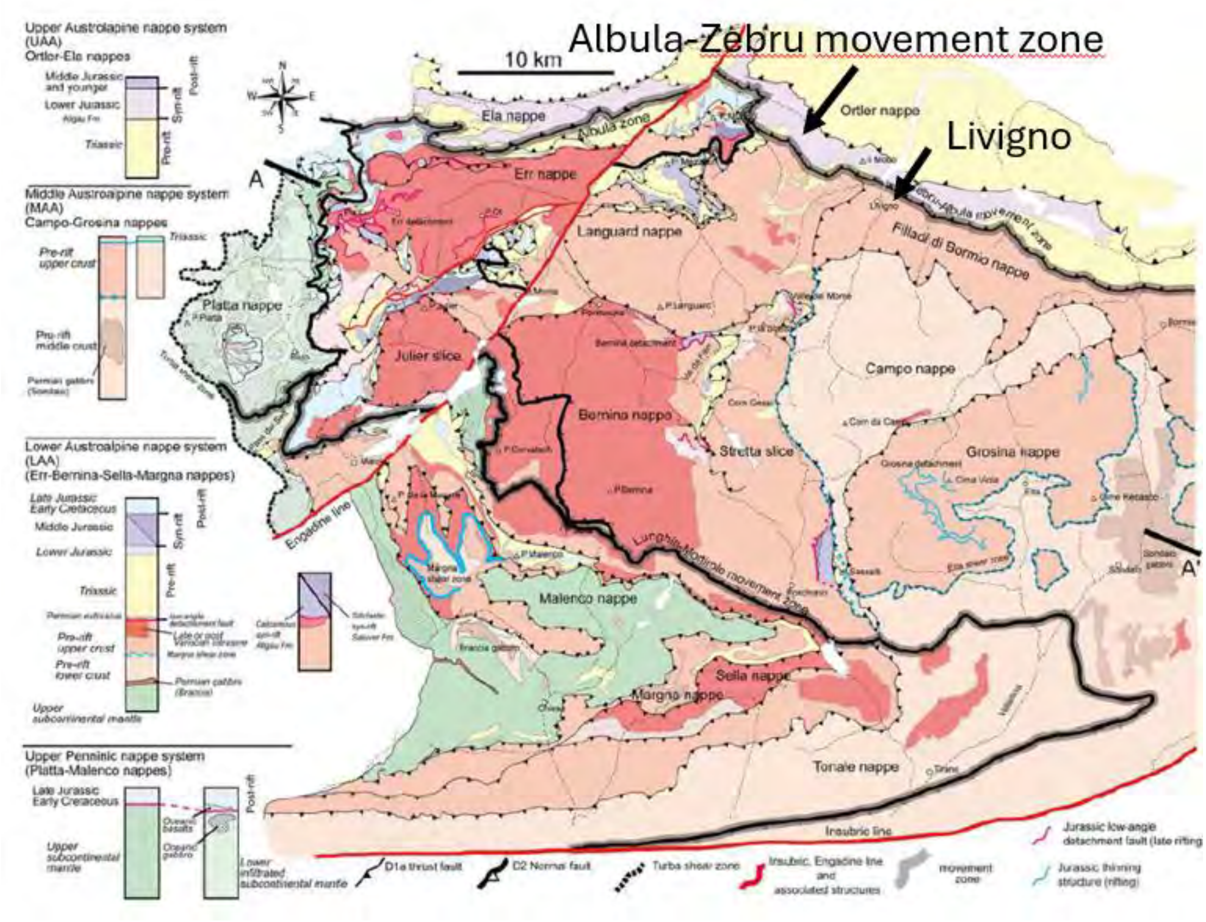

Figure 2: Geological map of the Austroalpine-Penninic nappe stack. Map compiled after (Cornelius,1932; 1935; 1950); (Staub, 1946); (Bonsignore at al., 1969 a, b); (Montrasio et al., 1969); (Bearth et al., 1987): (Liniger. 1992); (Spillmann,(1993; 2005); (Froitzhein et al, 1994); (Meier, 2003); (Trommsdorff et al., 2005); (Peters, 2005 ;2007), modified from (Mohn et al.; 2011).

The Austroalpine nappes evolved into an "orogenic lid" during Tertiary collision, as they were thrust over the underlying Penninic domains. Previous work in nearby regions, such as the Engadine Dolomites (Conti, 1992, 1994, 1997), has documented a complex polyphase tectonic evolution, including early nappe emplacement of the Ortler over the Campo nappe, followed by strike-slip and transpressional overprinting. These later events are often associated with major fault zones like the Engadine Line, a significant strike-slip system that played an important role in post-collisional deformation (Schmid and Froitzheim, 1993).

Field observations **(Figure 3)** indicate that the study area is transected by a thrust surface that separates lithologies with distinct deformation characteristics and rheological responses.

*Figure 3: **(a - b)** Overview of the outcrop, showing the structural relationship between two contrasting rock units. Indicated by an arrow: folded rocks with steeply dipping layers. In contrast, the upper part (grey indicated by white lines) gently dipping, weakly or undeformed rocks, indicating significantly less deformation and suggesting a distinct structural history or tectonic origin. **(c)** Zone just below the upper unit (Ortler nappe).*

The structural fabric developed along and adjacent to this contact provides key kinematic indicators that allow reconstruction of the transport direction and shear sense associated with movement along the reactivated Albula–Zebrù movement zone **(cf. Figure 2)**. The geometry of S–C fabrics, asymmetric folds, and shear bands can determine whether reactivation occurred under normal (extensional) or reverse (compressional) kinematics (cf. Passchier and Trouw, 2005). Because of the repeated reactivation of the structural boundary, these contrasting movements often overprint one another, making it difficult to assign a single tectonic event to the observed deformation.

The study area offers an opportunity to investigate these relationships across an exposed nappe contact by combining structural mapping with micro- and mesostructural analysis.

The main research question addressed in this thesis is therefore:

What transport direction and shear sense associated with the Albula–Zebrù movement zone are recorded by deformation structures along the studied nappe contact, and do they indicate normal or reverse kinematics during reactivation?

2. Tectonic Evolution of the Central Alps

The tectonic history of the Alpine orogen **(Figure 4)** started with a phase of Permian-Triassic lithospheric extension, which led to the Mid-Jurassic opening and spreading of the Tethys-related Piemont-Liguria Ocean. During this extensional regime, the passive continental margins - specifically the European plate to the north and the Gondwana-affiliated Adriatic plate to the south - were fragmented into distinct crustal blocks, or microcontinents originally separated by narrow marine seaways.

The Alps as known today are a collisional orogen resulting from the convergence of the European and African (Adriatic) plates, a process that has been active since the Cretaceous period (Dewey et al., 1989). Estimates suggest a start of the geodynamic transition from lithospheric extension to convergence around 100 Ma ago. A regime of sinistral wrenching between the Eurasian and Gondwana plates was tectonically inverted to kinematics of convergence (Savostin et al., 1986). Driven by south-dipping subduction, fragments of the former continental margins were dragged to significant depths, reaching eclogite-facies metamorphic conditions (13–27 kbar and 520–750 °C) by approximately 90 Ma (cf. Thöni, 2006).

By the Paleogene to early Eocene (ca. 45 - 40 Ma), the continuous south-directed subduction changed to continental collision (stratigraphically recorded by the initiation of continental sedimentation in the adjacent foreland basins (Kempf and Pross, 2005)). The collision drove thrusting toward the Molasse foreland; meanwhile, the deeper units of the accumulating nappe stack were overprinted by regional Barrovian metamorphism.

Between 35 and 30 Ma, the orogen experienced a major tectono-magmatic event characterized by pronounced plutonism and the rapid exhumation of deeply buried crustal units. This dynamic phase is interpreted to be the result of lithospheric slab break-off (Von Blanckenburg and Davies, 1995). The consequent isostatic rebound likely generated the highest topographic elevations in the history of the Alps, triggering dramatic erosional rates.

This strong erosion is reflected by the deposition of thick, coarse conglomeratic delta deposits in the northern Molasse foreland basin (Kempf and Pross, 2005). Thermochronological data indicate that the rocks exposed today had cooled below low-temperature conditions by around 15 Ma (cf. Hansmann, 1996). Meanwhile, deformation continued to migrate outward, leading to the formation of the Jura Mountains.

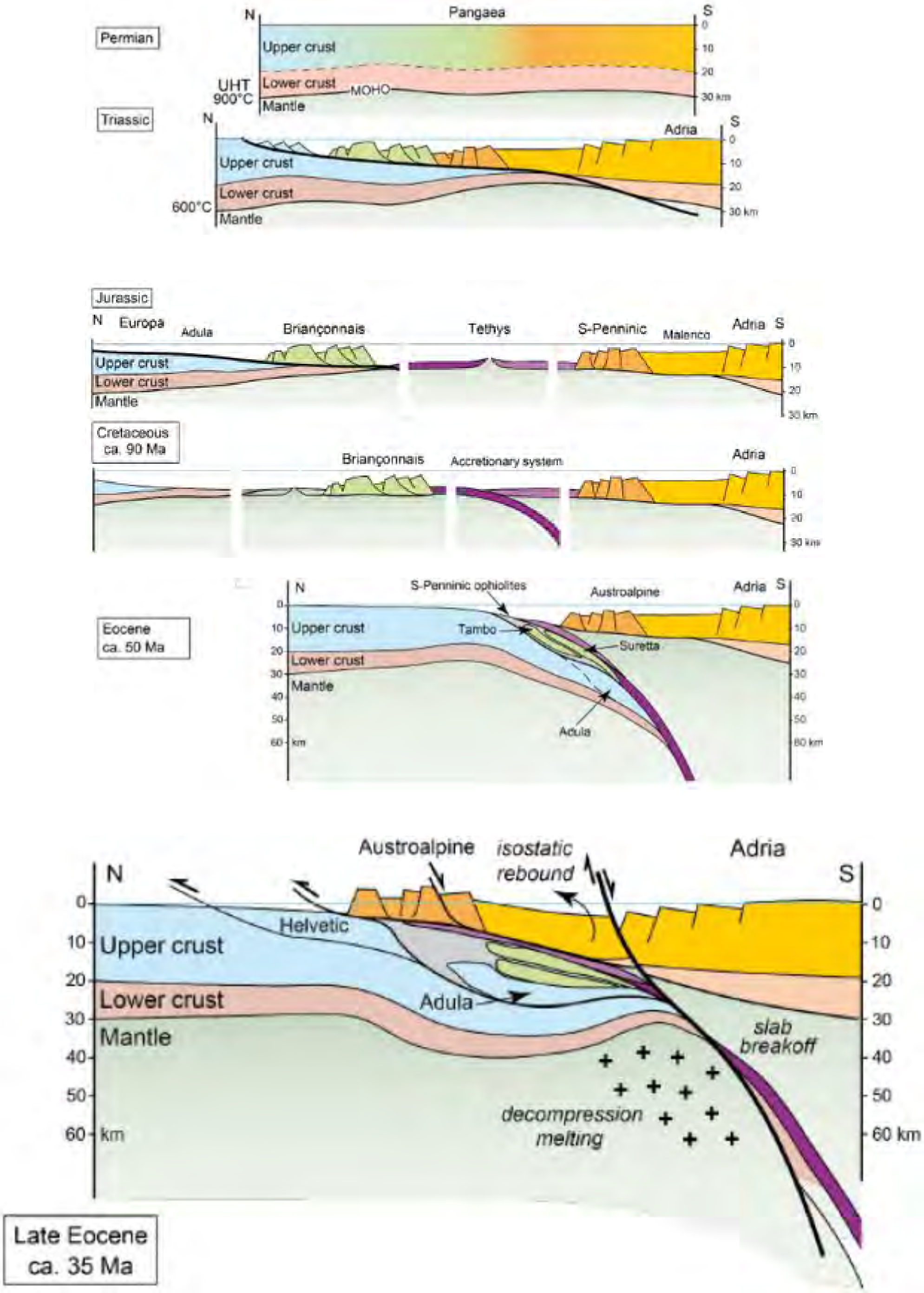

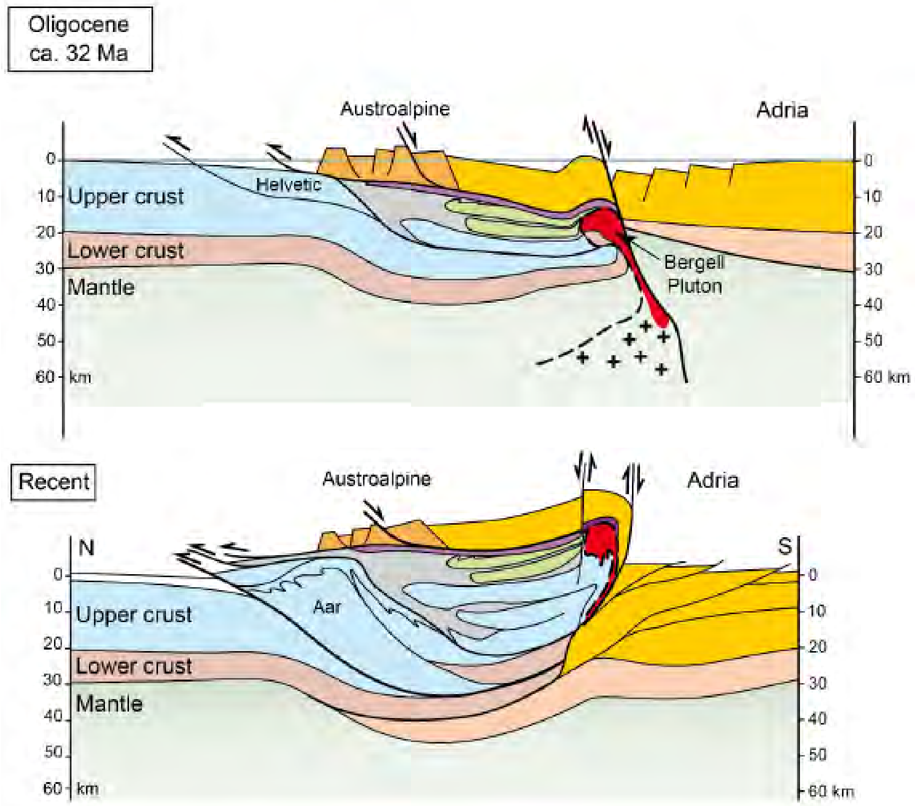

Figure 4: Tectonic evolution of the Alps (Burg et al, 2016).

The geodynamic development led to the current structural framework of the mountain belt, characterized by a massive stack of nappe units thrust northwards onto the European foreland. In the Central and Eastern Alps, this complex architecture is systematically organized into three principal tectono-stratigraphic domains **(cf. Figure 1)** that directly reflect their distinct paleogeographic origins (Schmid et al., 2004).

Structurally lowest is the **Helvetic Zone**, which comprises the deformed proximal sequences of the former European continental margin. Overlying this is the highly heterogeneous **Penninic Zone**, encompassing the subducted and exhumed remnants of the Alpine Tethys - specifically the Valais and Piemont-Liguria oceanic basins - along with the Briançonnais microcontinent located between them. The orogenic sequence is capped by the **Austroalpine Zone**, representing the passive continental margin of the Adriatic (Apulian) microplate, which acted as the rigid overriding upper plate throughout the Alpine collisional history. This Austroalpine domain forms the structural "lid" of the Alpine nappe stack in the Eastern Alps. While it is largely eroded in the Western Alps, it covers vast areas east of the Rhine Valley (Pfiffner, 2024). Tectonically, the Austroalpine is traditionally subdivided into the lower and middle Austroalpine (representing the distal, thinned margin of Adria) and the upper Austroalpine (representing the main continental crust).

3. Tectonic Architecture of the Livigno Region

3.1 Overview

Located within the Austroalpine domain of the Central Alps, the nappes of the Livigno area represent the Adriatic continental margin, comprising crystalline basement and Mesozoic cover (Schmid et al., 2004). The study area is located at a critical tectonic intersection within the middle to upper Austroalpine domain. It is defined by the interaction between two major crystalline basement units - the Languard nappe and the Campo nappe (belonging to the middle Austroalpine domain) - and the Ortler nappe (belonging to the upper Austroalpine domain) **(Figure 2)**. They are separated by the Albula-Zebrù movement zone **(Figure 2)**.

- **Languard nappe (Lower Unit):** In the southwestern part of the study area, the Languard nappe represents the structurally lowest crystalline unit. It is characterized by its distinct basement lithologies and forms the footwall to the overriding Campo nappe. This unit consists largely of polymetamorphic micaschists and gneisses (Spitz & Dyhrenfurth, 1914).
- **Campo nappe (Middle Unit):** The Campo nappe represents a massive crystalline basement block. The tectonic contact with the underlying Languard nappe is marked by a clear thrust, placing the Campo basement structurally above the Languard unit. The contact between the Languard and Campo basement units is not a simple planar fault but a complex tectonic zone, often marked by mylonites or sandwiched sedimentary slices (Froitzheim et al., 1994).
- **Ortler nappe (Upper Unit):** The Ortler nappe, primarily consisting of a thick Mesozoic sedimentary cover, represents the highest tectonic element in this local stack. It overprints the contact between the Campo and Languard nappes, acting as an "orogenic lid." The basal contact of the Ortler nappe is the Albula-Zebrù movement zone, which facilitated the large-scale transport of the sedimentary sequence over the underlying basement units. The separation of the Ortler sediments from their crystalline substrate occurred along weak Carnian evaporite horizons (Rauhwacke/Carnioles), also referred as Raibl Group (Raibl beds) (cf. Bernoulli et al.,2024). While the basement units deformed in a semi-brittle to ductile manner, the

Ortler carbonate platform (consisting of the massive *Hauptdolomit*) was folded and thrust westward during the Alpine orogeny (Schmid and Haas, 1989).

The cross section in **Figure 5 and 6** preserves evidence of inherited Mesozoic extensional tectonics. These Jurassic detachment faults are represented by the Ducan (Du), Trupchun (Tr), and Turba (Tu) detachments, which are shown as low-angle normal faults within the central and southeastern parts of the profile. The detachments developed during Late Triassic to Jurassic rifting associated with the opening of the Alpine Tethys and controlled crustal thinning and the formation of hyperextended continental margins. During subsequent Alpine convergence, these former extensional structures were partially reactivated and incorporated into the nappe stack, resulting in a complex superposition of compressional and extensional geometries.

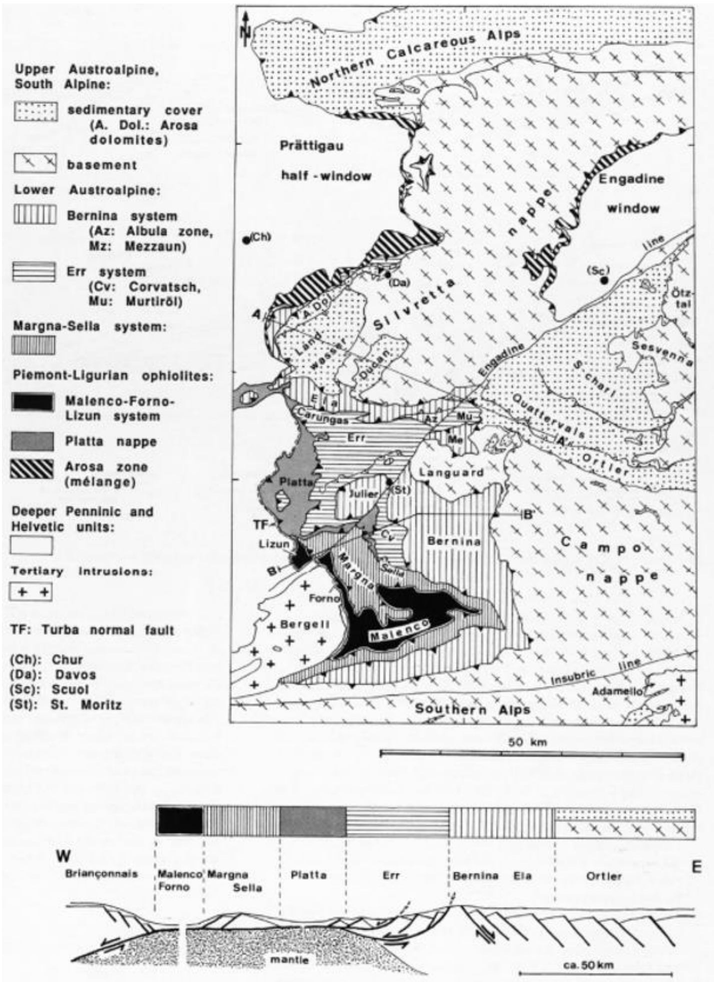

__Figure 5:__ Tectonic map and reconstructed E–W cross-section of the Austroalpine realm in Graubünden, illustrating the architecture of the preserved passive continental margin. The current distribution shows the fragments of this margin dislocated toward the west. Triangles on tectonic boundaries indicate the structurally higher unit (hanging wall), regardless of the fault's kinematic nature (adapted from Schmid et al., 1997 and Froitzheim et al., 1994).

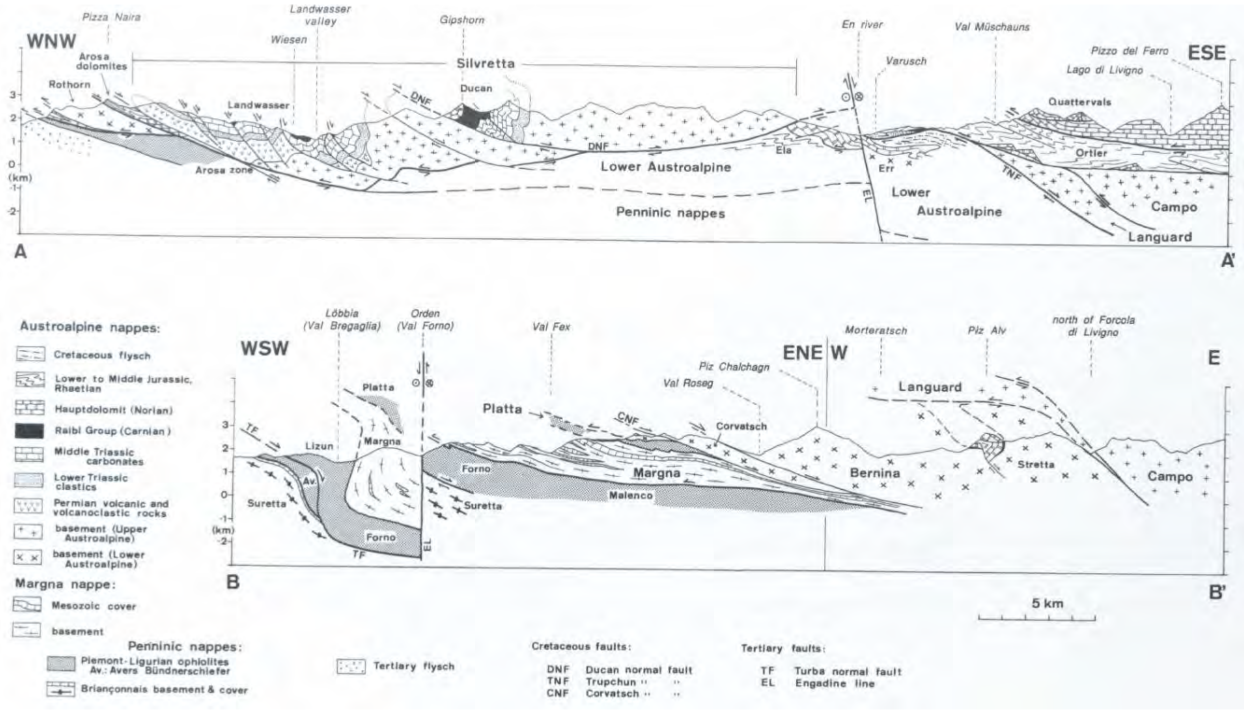

Figure 6: *Two structural cross-sections A–A' and B–B' through the Austroalpine nappe stack of eastern Switzerland. Profile A–A' (WNW–ESE) displays the tectonic relationship between the Penninic units and the Austroalpine units, including the Languard and Campo nappes. Profile B–B' (WSW–E) highlights the internal architecture of the basement units. The profile traces are indicated on the tectonic map in Figure 5 (after Schmid et al., 1997).*

3.2 The Study Area

The study area includes the tectonic contact between the Languard, Campo and Ortler nappes. Morphologically, the terrain is characterized by parallel mountain ridges shaped by glacial erosion. Topographic and geological maps of the sampling localities are presented in **Figures 7 to 11**.

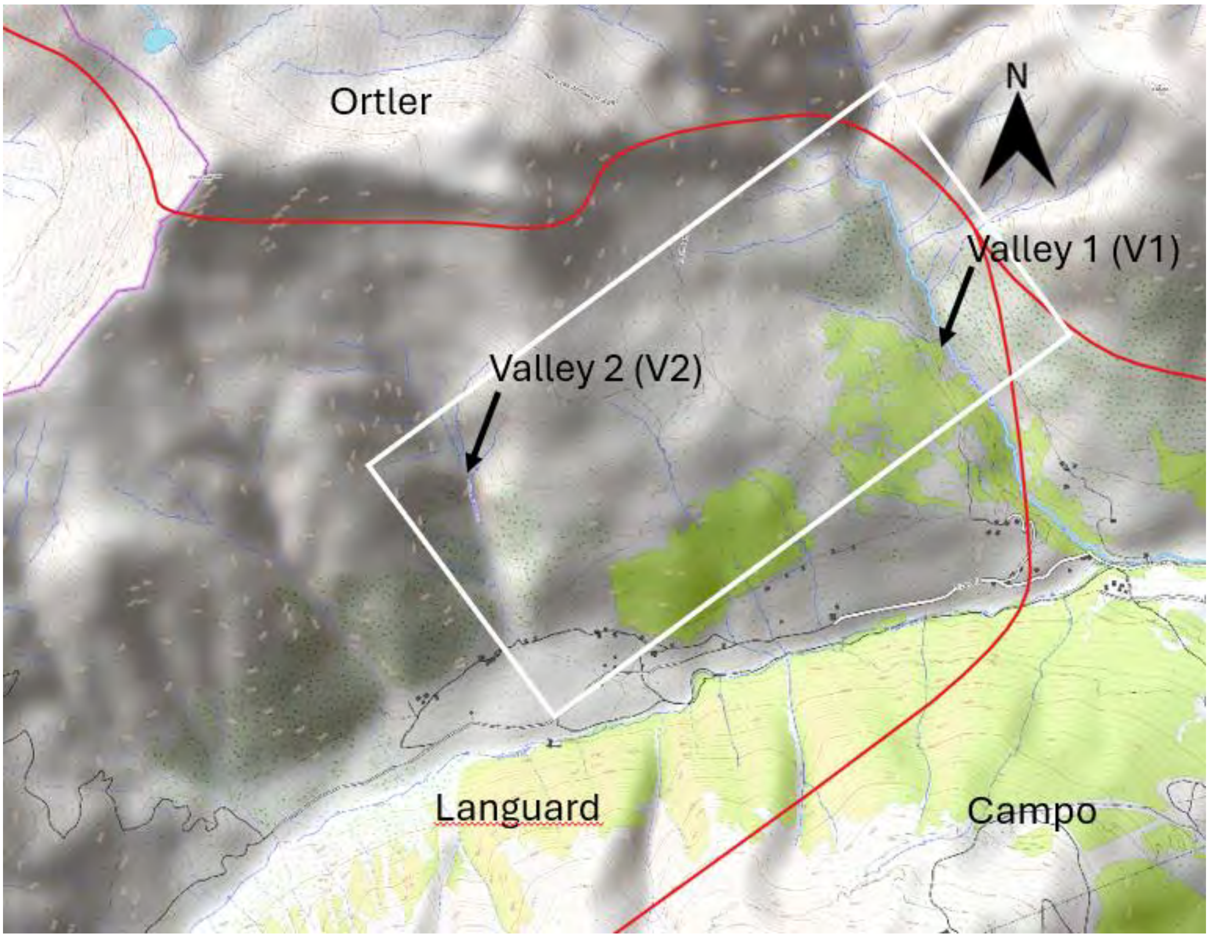

Figure 7: *The study area (white box) is located north west of Livigno, covering two valleys (V1 and V2). V1 follows the tectonic line (red): (Ortler-Languard (N), Campo-Languard (S). (Data source: Swisstopo (2026); Digital Elevation Model (DEM)**:** NASA Shuttle Radar Topography Mission (SRTM, 2013), accessed via OpenTopography (2026); Visualization: QGIS (QGIS Development Team, 2026).*

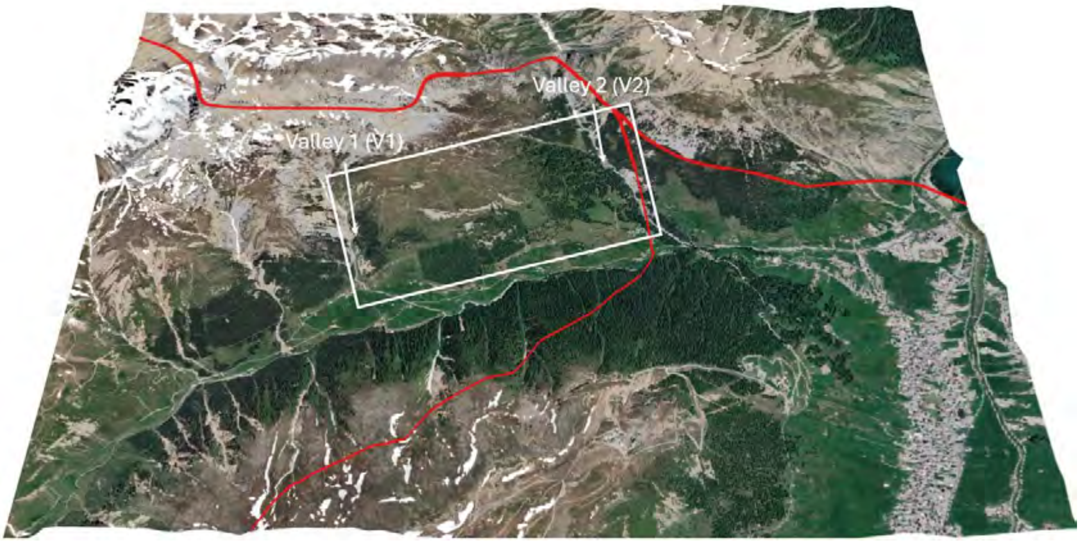

Figure 8: 3D topographic visualization of the study area. *The digital elevation model illustrates the terrain of the study area and the spatial relationship between Valley 1 and Valley 2. Red line: nappe contacts (see Figure 7 for details). Topographic data provided by Swisstopo (2026); Digital Elevation Model (DEM) derived from SRTM 30m (NASA JPL, 2013), accessed via OpenTopography (2026); 3D rendering and visualization performed using QGIS (QGIS Development Team, 20 2026).*

Figure 9: Qverview of the study area. (a) *view of the study area situated below the Ortler nappe.* ***(b)*** *Top of Valley 1 (V1) looking towards the West.* ***(c)*** *view from the ridge between Valley 1 and Valley 2, facing North.* ***(d)*** *Overview of Valley 2 (V2) illustrating the structural contact between the overlying Ortler nappe and the underlying, steeply dipping bedding (Languard nappe).* ***(e)*** *Eastern flank of Valley 2 displaying eastwards dipping beds (Languard).* ***(f)*** *view of the Valley 1 towards NW* ***(g, h)*** *Field observations of the Raibl beds located on the eastern side of Valley 1 (cf. Figure 10).*

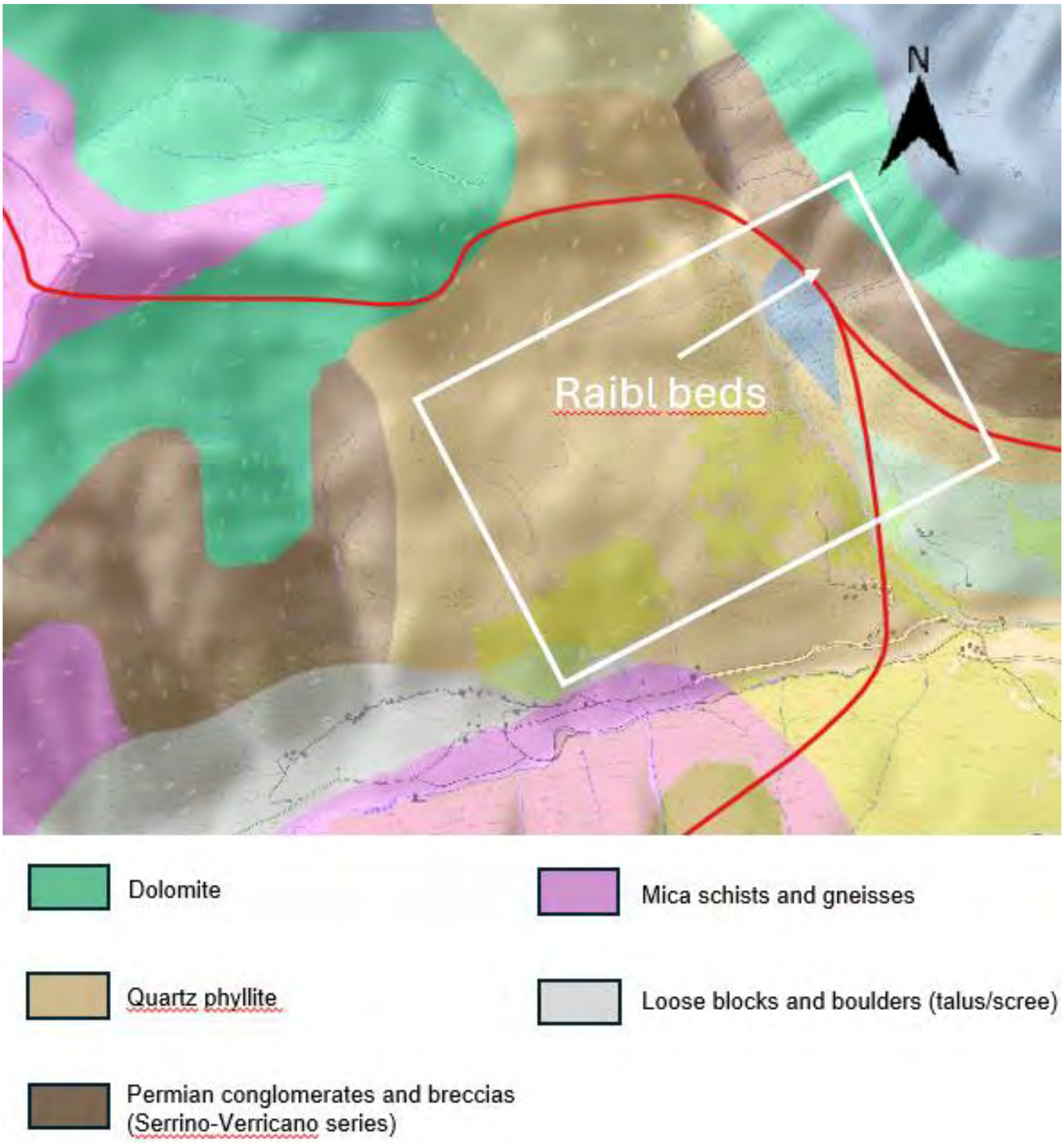

***Figure 10**: **Geological map of the study area showing lithological units and tectonic structures.** Red line: Tectonic line separating the Ortler nappe from underlying Languard (west) and Campo (East) nappe, white box: study area. The map is oriented with North at the top. White arrow indicating Raibl beds found in the field **(cf. Figure 9)** (Data sources: Swisstopo (2026); Digital Elevation Model (DEM): SRTM 30m (NASA JPL, 2013) accessed via OpenTopography (2026); Visualization and GIS-based mapping: QGIS (QGIS Development Team, 2026).*

Hillshade analysis performed in QGIS reveals parallel mountain ridges **(Figure 11)**. The valleys were carved by glacial activity that selectively eroded weaker, highly deformed shear zones. Below the nappe contact in V1 a fine-grained shear zone can be identified.

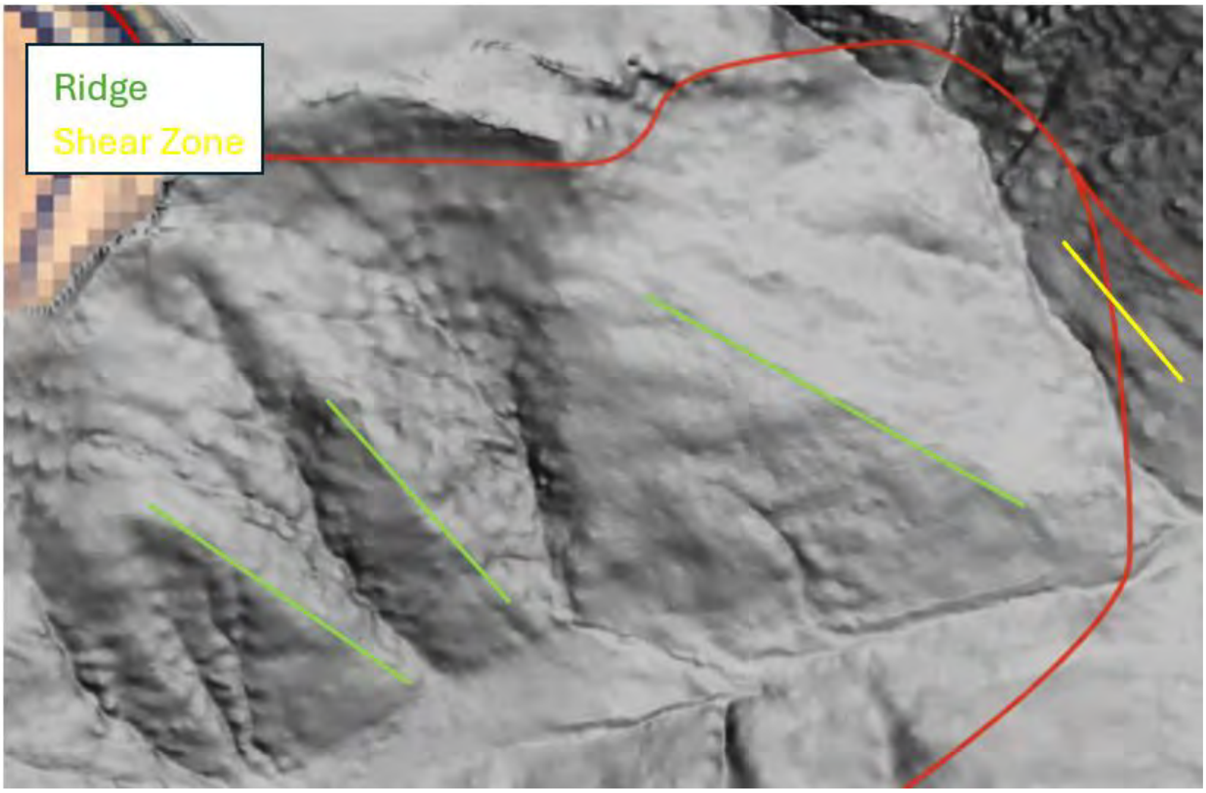

Figure 11: Hillshade analysis of the study area illustrating the structural grain and tectonic architecture. *The shaded relief emphasizes the parallel mountain ridges (green line). Red line: Tectonic line. Immediately beneath this contact on the east side of Valley 1 (V1), a zone of intense strain localization (yellow line) is identified (crossing the Languard/Campo nappe contact, below the Raibl beds* ***(cf. Figure 9,10)****, characterized by fine-grained shear fabrics. Data sources: Swisstopo (2026); Digital Elevation Model (DEM): SRTM 30m (NASA JPL, 2013) accessed via OpenTopography (2026); Visualization and GIS-based mapping: QGIS (QGIS Development Team, 2026).*

4. Deformation Phases and Tectonic Evolution

The Languard, Campo, and Ortler units are part of the upper Austroalpine 'lid,' which reached sub- to low-greenschist facies metamorphism **(Figure 12)**.

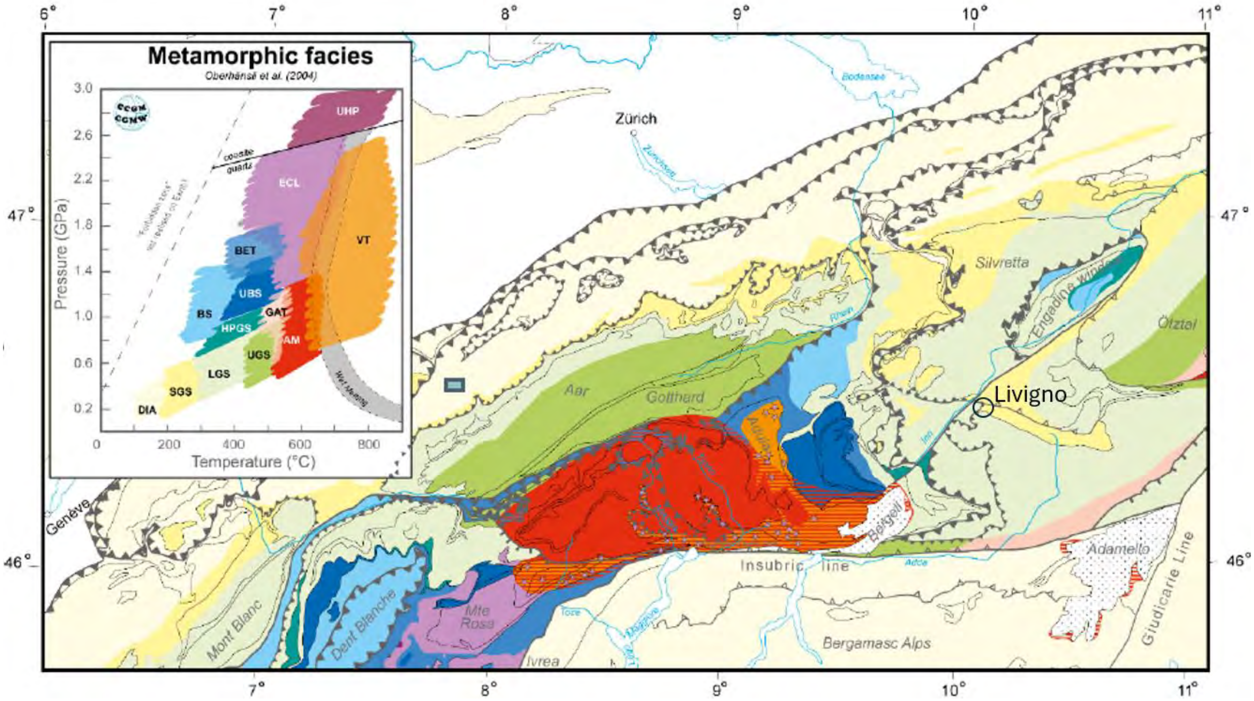

Figure 12: Metamorphic map of the Alps. *Modified after Oberhänsli et al. (2004). The circle indicates the location of the study area within the Austroalpine domain.*

As documented in the Lower Austroalpine of Graubünden and adjacent areas, the region experienced repeated transitions between extensional and compressional regimes throughout the Alpine orogeny (Froitzheim et al., 1994; Schmid et al., 2004; Handy et al., 2010).

The present structural architecture reflects Alpine collision overprinting inherited Jurassic rift structures.

1. **Jurassic rifting and hyperextension of the Adriatic margin** (Mohn et al., 2011), and
2. **Cretaceous to Oligocene Alpine convergence and reactivation** (Froitzheim et al., 1994).

Importantly, the deformation stages D1a–D2 of Mohn et al. (2011) refer to early rift-related processes, whereas the D1–D5 phases of Froitzheim et al. (1994) describe exclusively Alpine deformation. These two-phase systems represent distinct tectonic frameworks and are therefore correlated in **Table 1**.

Time	Tectonic setting	Mohn et al. (2011) – Rift & Alpine framework	Froitzheim et al. (1994) – Alpine phases
Early Triassic–Early Jurassic	Initial continental rifting	**D1a - Stretching phase**: high-angle normal faulting, half-graben formation	–
Middle–Late Jurassic	Advanced rifting and hyperextension	**D1b-D2 - Necking and hyperextension**: detachment faulting, crustal thinning, exhumation of basement	–
Late Cretaceous (Eo-Alpine)	Alpine convergence and nappe stacking	Reactivation of inherited rift structures	**D1 (Trupchun Phase)**
Late Cretaceous	Syn-orogenic extension	Continued reactivation under extensional regime	**D2 (Ducan - Ela Phase)**
Early Tertiary (Eocene)	Renewed crustal shortening	–	**D3 (Blaisun Phase)**

Time	Tectonic setting	Mohn et al. (2011) – Rift & Alpine framework	Froitzheim et al. (1994) – Alpine phases	Expression in the Livigno area
Oligocene	Post-collisional extension and late shortening	–	**D4 (Turba Phase)** – extension; **D5 (Domleschg Phase)** – NW–SE shortening	Late reactivation and regional overprint

Table 1: *Correlation of deformation phases in the Austroalpine units according to (Froitzheim et al., 1994) and the rift inheritance framework of (Mohn et al., 2011).*

The Albula–Zebrù movement zone has originated as a major extensional detachment during the Jurassic rifting of the Adriatic margin (consistent with the D1b-D2 rift phase of Mohn et al., 2011). During the subsequent Alpine Orogeny, this fundamental weakness in the crust was repeatedly reactivated. Many Alpine shear zones represent reactivated rift-domain boundaries. Their geometry, rheology, and orientation strongly influence the localization of shortening, extension, and later transpressional deformation. In this context, the Albula–Zebrù movement zone can be interpreted as a long-lived crustal discontinuity whose kinematic evolution reflects progressive inversion and overprinting of inherited rift architecture **(cf. Figure 2)**.

5. Investigation Strategy and Methodology

To fully characterize the nappe contact, an integrated approach comprising field mapping, structural analysis, micro-/mesostructural (including petrographic analysis) was used.

5.1 Structural Analysis

Structural orientations are reported using the dip direction/dip convention. The dip direction refers to the compass azimuth (000° - 360°) of the maximum inclination of a plane, while the dip represents the vertical angle (0° - 90°) of that plane measured from the horizontal.

Structural measurements (bedding, foliation, and stretching lineations) per section were processed using stereographic projection analysis to calculate fold axes and model the kinematic framework of the investigated nappe contact. All calculations and spatial data representations were performed using the software Stereonet 11 (Allmendinger, 2026, Allmendinger et al., 2012; Cardozo and Allmendinger, 2013).

Eigenvector analysis of the poles to planes (π-method / best fit great circle) was primarily applied to determine the fold axes (Lisle and Leyshon, 2004). For verification planar intersection analysis (beta-method/lines of intersection) was used. The best fit great circle method is more robust against statistical noise caused by subparallel surfaces. Significant discrepancies between the two methods served as indicators for a high variance of measurement.

Digital mapping and spatial analysis were carried out using QGIS (2026), topographic datasets from Swisstopo (2026) and OpenTopography (2026), and the digital elevation model of the NASA Shuttle Radar Topography Mission (SRTM) for terrain characterization.

5.2 Micro- and Mesoscopic Characterization

To validate field observations and determine the regional kinematics, seven oriented samples (TS 1-7) from key outcrops across the shear zone were analyzed in thin section. The sense of shear was evaluated using micro- (TS 1-7) and mesoscopic kinematic indicators (field observations). The criteria analyzed included (cf. Passchier and Trouw, 2005):

- **S-C and S-C' fabrics:** Used to determine the shear sense based on the angular relationship between the primary shear surfaces (C-planes) and the mylonitic foliation (S-planes), and the direction of the shear bands (C'-planes).
- **Asymmetric Porphyroclasts:** clasts were evaluated to deduce the relative shear sense direction.
- **Rotated Porphyroblasts:** Snowball structures and their internal inclusion trails were analyzed to establish the rotational sense during syn-kinematic mineral growth.
- **Fractured Porphyroclasts (Bookshelf Gliding):** Brittle fracturing and displacement of rigid clasts within a ductile matrix (microboudinage) were evaluated. The synthetic or antithetic slip along these micro-faults, resembling a bookshelf mechanism, was used as an indicator to determine the sense of shear.
- **Fold Geometries:** Asymmetric folds were used (with caution) as kinematic indicators.

5.3 Petrographic Analysis and Mineral Assemblages

Petrographic analysis was conducted on the seven oriented samples (TS 1 (Campo), T2 - T7 (Languard)) collected across the study area (analysis at the University Basel, Department of Environmental Sciences (Prof. Dr. Leander Franz). For image size determination and scale calculations the instrumentation table in **Appendix C** was used. Thin sections were examined under a polarizing microscope to determine mineral assemblages, textures, and deformation microstructures. Attention was given to mineral composition, foliation, recrystallization features. Observations were used to characterize protoliths, estimate metamorphic conditions, and support the structural interpretations derived from field data.

6. Results

Geometry, orientation, and style of mesoscopic structures across the study area were documented. This included measuring the dip direction and dip of foliations, folds, shear zones, and stretching lineations and the photographic documentation of the shear sense indicators. Sampling localities and the positions of all field photographs discussed in the text are provided in **Figure 13.**

Figure 13: Overview maps Valley 1 (V1). (a) *Overview study area.* ***(b)*** *Locations of the oriented rock samples* ***(TS 1 to TS 7, cf. Table 2 for data)*** *collected for microstructural thin-section analysis. Arrow indicating down plunge direction of the lineation.* ***(c)*** *Locations of the mesoscopic field photographs documenting kinematic indicators (e.g., shear bands, clasts). Data source: Swisstopo (2026); Topography derived from SRTM 30m (NASA JPL, 2013) accessed via OpenTopography (2026); Visualization and GIS-based mapping: QGIS (QGIS Development Team, 2026).*

Datum	Longitude	Latitude	DipDir	Strike	Dip	Type	height m	Location	Description 1	Description 2	Trend	Plunge
18.08.2025	10,1222062	46,555514	79	349	26	foliation	1881	Valley 1	TS 1	Probe 1 oben		
18.08.2025	10,1222062	46,555514				lineation	1881	Valley 1	TS 1 Lineation	Probe 1 Lineation	74	24
19.08.2025	10,11551	46,5645	0	270	26	bedding	2054	Valley 1	TS 2	Probe 2 oben S plane		
19.08.2025	10,11551	46,5645				lineation	2054	Valley 1	TS 2 Lineation	Probe 2 Lineation	263	11
19.08.2025	10,11596	46,56353	350	260	11	bedding	2020	Valley 1	TS 3	Probe 3 oben		
19.08.2025	10,11596	46,56353				bedding	2020	Valley 1	TS 3 Lineation	Probe 3 lineation	260	3
19.08.2025	10,11614	46,56332	55	325	40	bedding	2017	Valley 1	TS 4	Probe 4 oben		
19.08.2025	10,11614	46,56332				lineation	2017	Valley 1	TS 4 Lineation	Probe 4 oben lineation	114	20
19.08.2025	10,11695	46,56244	83	353	15	bedding	2003	Valley 1	TS 5	Probe 5 oben		
19.08.2025	10,11695	46,56244				lineation	2003	Valley 1	TS 5 Lineation	Probe 5 oben lineation	93	15
19.08.2025	10,11695	46,56172	120	30	24	bedding	1984	Valley 1	TS 6	Probe 6 oben		
19.08.2025	10,11695	46,56172				lineation	1984	Valley 1	TS 6 Lineation	Probe 6 oben lineation	318	2
19.08.2025	10,11935	46,55943	49	319	39	foliation	1946	Valley 1	TS 7	Probe 7 oben		
19.08.2025	10,11935	46,55943				lineation	1946	Valley 1	TS 7 Lineation	Probe 7 oben lineation	120	10

Table 2: *Structural field measurements of the samples Thin Section 1-7 taken in Valley 1 (V1). Strike values follow the Right-Hand Rule convention (Strike = Dip Direction - 90°).*

6.1 Structural analysis

6.1.1 Valley 1 (V1)

According to the tectonic map (Swisstopo, 2026), the Languard/Campo nappe contact is in valley 1 (V1) at ca. 1924 m altitude and the Ortler nappe at ca. 2130 m **(Figure 13)**. This information was used together with lithologic characteristics **(Figure 10)** to distinguish between the different nappes. To bundle measurements along the valley also the altitude was used, as the steady incline provides uniform intervals for creating comparable sections.

The structural investigation starting at the Campo nappe, crossing the Languard nappe to the Ortler nappe within Valley 1 (V1) **(Table 3, Figure 14)** is characterized by gently plunging fold axes (all < 20°) rotating counterclockwise relative to the down plunge direction **(Table 3)**. Lineations within the Campo nappe show an average trend of 136°/20° (SE) **(Table 4, Figure 15)**. The calculated fold axis using data for foliation **(Table 3, Figure 14)** in this sub-area should be interpreted with caution; the high concentration of poles (based on measurements of the fold axis) (Axis 1 eigenvalue ca. 0.94) forms a dense cluster rather than a distinct girdle, making the best-fit great circle statistically weakly defined. The π-method (111°/10°) and the beta-method (117°/20°) however yield nearly identical orientations and can therefore be considered as robust.

Within the Campo nappe, the calculated fold axis derived from bedding data (160°/13°) is different compared to the fold axis derived from foliation data (111°/20°).

Within the Languard nappe, a structural discontinuity is identified between 2000 m and 2050 m, marked by a strong rotation of the fold axes towards NE. This structural discontinuity is just below the nappe contact between Ortler and Languard. Getting closer to the Languard/Ortler nappe contact (ca. 2050–2150 m), the fold axis shift to a NE trend (63° - 43°). Using data from the Ortler nappe in valley 1 reveals a fold axis with a trend of 69° and a plunge of 15°, close to the data received just below at the Languard/Ortler nappe contact. A fold axis with a trend of 77° and a plunge of 16° can be calculated using data from the Ortler nappe throughout the study area.

The lineation, based on down plunge direction, is rotating counterclockwise (136° - 108°) with a low to almost horizontal plunge (20° - 6°) **(Table 4, Figure 15)**.

Stereonet	Section (m)	Trend	Plunge	Nappe	Interpretation
	Calculated fold axes (bedding measurements)				
(a)	**1800–1924**	160° (SE)	13°	Campo	Plunging to the SE
(b)	**1924–2000**	111° (SE)	20°	Languard	Very gently plunging to the SE
(c)	**2000–2050**	58° (NE)	11°	Languard	Sub-horizontal, plunging to the NE
(d)	**2050–2100**	63° (NE)	13°	Languard	Gently plunging to the NE
(e)	**2100–2150**	43° (NE)	17°	Languard	Gently plunging to the NE
(f)	**> 2130**	69° (NE)	15°	Ortler	Only Valley 1
	> 2130	77° (NE)	16°	Ortler	Overall study area
Stereonet	**Section (m)**	**Trend**	**Plunge**		**Interpretation**
	Calculated fold axes (foliation measurements)				
(g)	**< 1924**	111°	20°	Campo	Plunging SE
(h)	**> 1924**	286°	4°	Languard	Plunging WNW, low plunge compared to Campo. Flattened footwall at Ortler/Languard nappe contact.

Table 3: Calculated fold axes per structural section in Valley 1 (V1). *Best-fit fold axes (**π**-axes) were determined for each defined elevation segment along the profile. Calculations were performed using the eigenvector-based π-pole method (Bingham statistics) in the software Stereonet (Allmendinger et al., 2012; Cardozo and Allmendinger, 2013).*

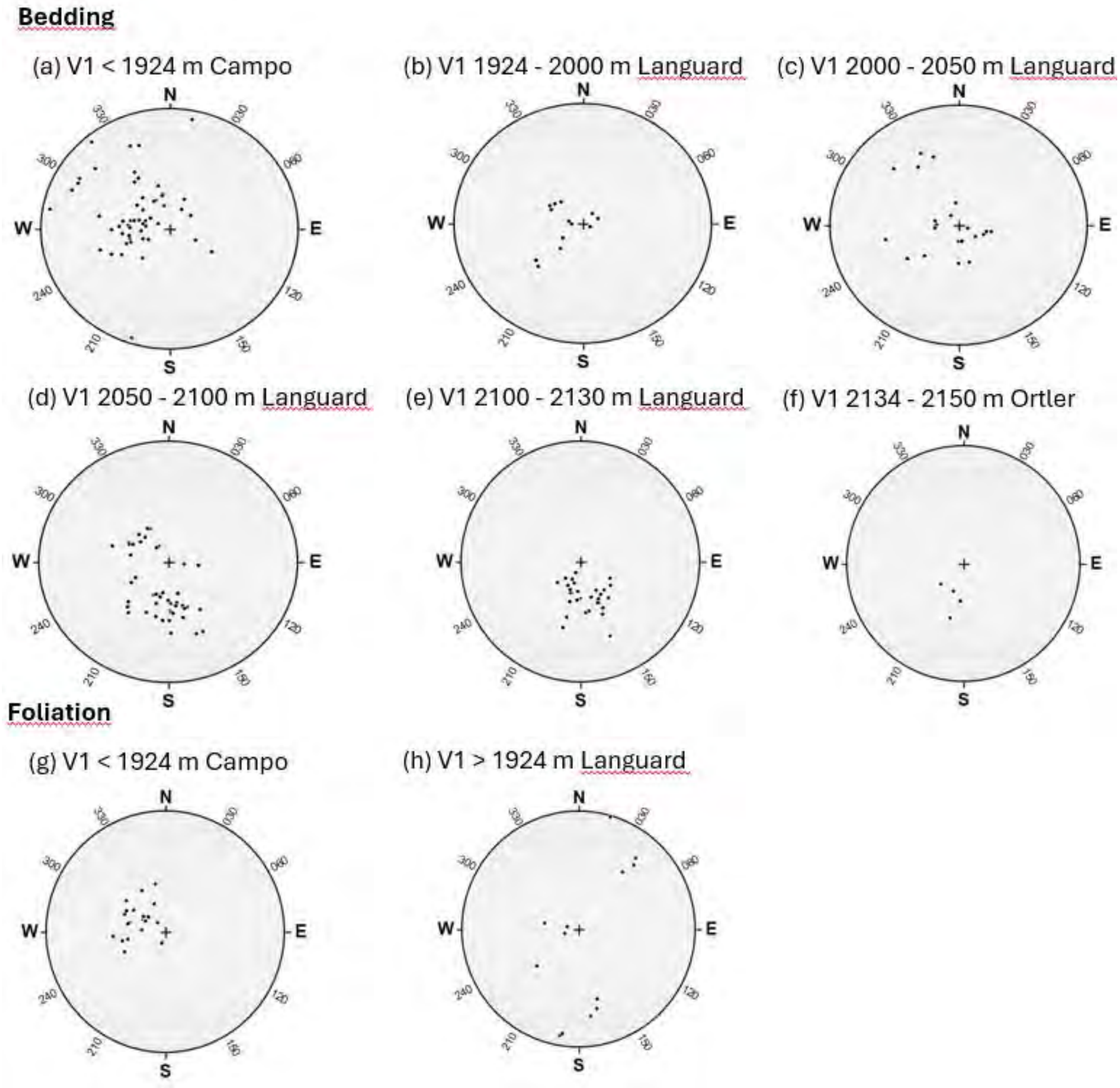

Figure 14: Structural data of Valley 1 within different nappes plotted in stereographic projection. *Projections and statistical best-fit calculations were generated using Stereonet (Allmendinger et al., 2012; Cardozo and Allmendinger, 2013). The data is subdivided into distinct structural domains (a: < 1900 m, b: 1900–2000 m, c: > 2000 m) to illustrate the kinematic rotation towards the nappe contact.*

Stereonet	Section (m)	Trend	Plunge	Direction	Nappe
Lineation					
(i)	**< 1924**	**136°**	**20°**	**S**	**Campo**
(j)	**1924 - 2000**	**128°**	**8°**	**SE**	**Languard**
(k)	**2000 - 2050**	**109°**	**6°**	**ESE**	**Languard**
(l)	**2050 - 2101**	**108°**	**6°**	**ESE**	**Languard**

***Table 4: Measured stretching lineations along Valley 1 (V1)**: The table summarizes the mean trend and plunge of the stretching lineations for each defined structural level. The data documents the progressive rotation of the kinematic transport direction towards the Ortler/Languard nappe contact.*

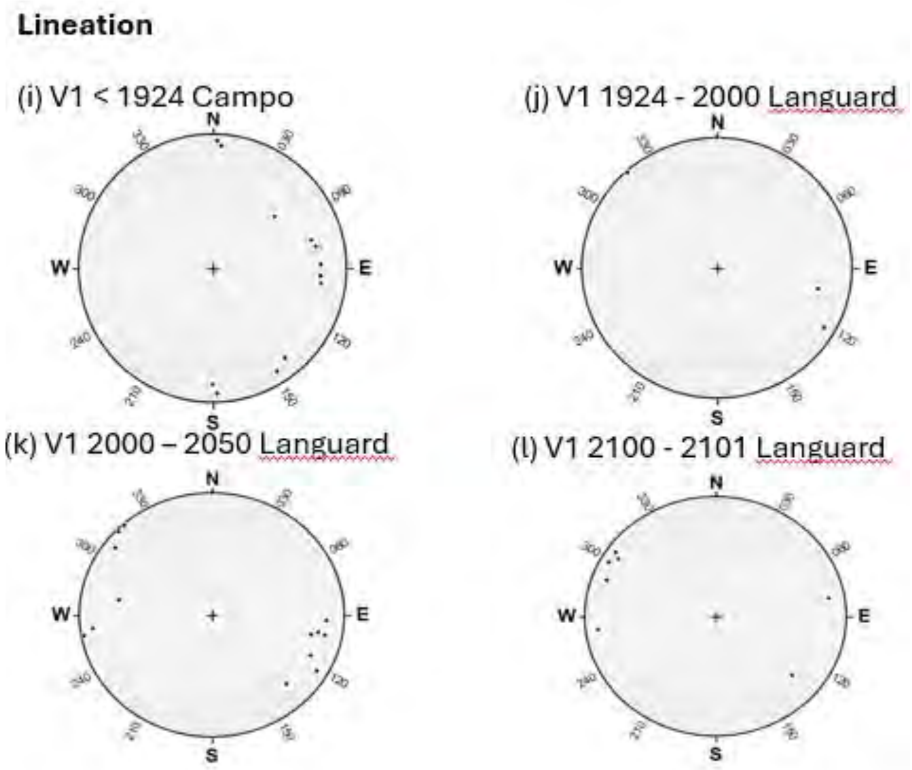

***Figure 15:** Kinematic rotation of stretching lineations along the V1 profile and within different nappes. Projections were generated using Stereonet (Allmendinger et al., 2012; Cardozo and Allmendinger, 2013).*

6.1.2 Between Valley 1 (V1) – Valley 2 (V2)

According to the tectonic map (Swisstopo, 2026), the Ortler nappe starts within this area at an altitude of ca. 2500 m. However, Dolomite (the lithologic characteristic of the Ortler nappe) starts lower at an altitude of ca. 2400 m. The section above 2400 m could therefore be considered as belonging to the Ortler nappe. The fold axes between the sections oscillate strongly between an SE and NNE-trend **(Table 5, Figure 16)**. Lower sections (<2100 – 2300) show a counterclockwise rotation of the fold axis relative to the down plunge direction (from 75° (ENE) to 22° (NNE)), with a decreasing plunge from 22° to 3°. In the section between 2300 m and 2400 m a strong rotation is shown (to 110° (SE), plunge 12°), returning to E (78°) with a plunge of 19° in the section above 2400 m.

Despite these sharp lateral shifts in direction, the plunge remains consistently gentle, maintaining a sub-horizontal inclination between 3° and 22°.

Stereonet	Section (m)	Trend	Plunge	Interpretation	Nappe
Calculated fold axes (bedding measurements)					
(m)	**Lower 2100**	75°	22°	Axis is oriented ENE	Languard
(n)	**2100 – 2300**	22°	3°	Sub-horizontal axis; aligns well with the "ideal" NNE strike for W-transport.	Languard
(o)	**2300 – 2400**	110°	12°	Strong rotation into the SE-WNW transport direction.	Languard
(p)	**2400 – 2500**	78°	19°	Axis returns to an ENE trend, showing continued rotational instability.	Ortler

Table 5: Calculated fold axes and kinematic interpretations for the structural profile between Valley 1 (V1) and Valley 2 (V2). *Best-fit fold axes were determined for different elevation sections to evaluate the spatial variation of the structural framework. Statistical calculations were performed using the software Stereonet (Allmendinger et al., 2012; Cardozo and Allmendinger, 2013).*

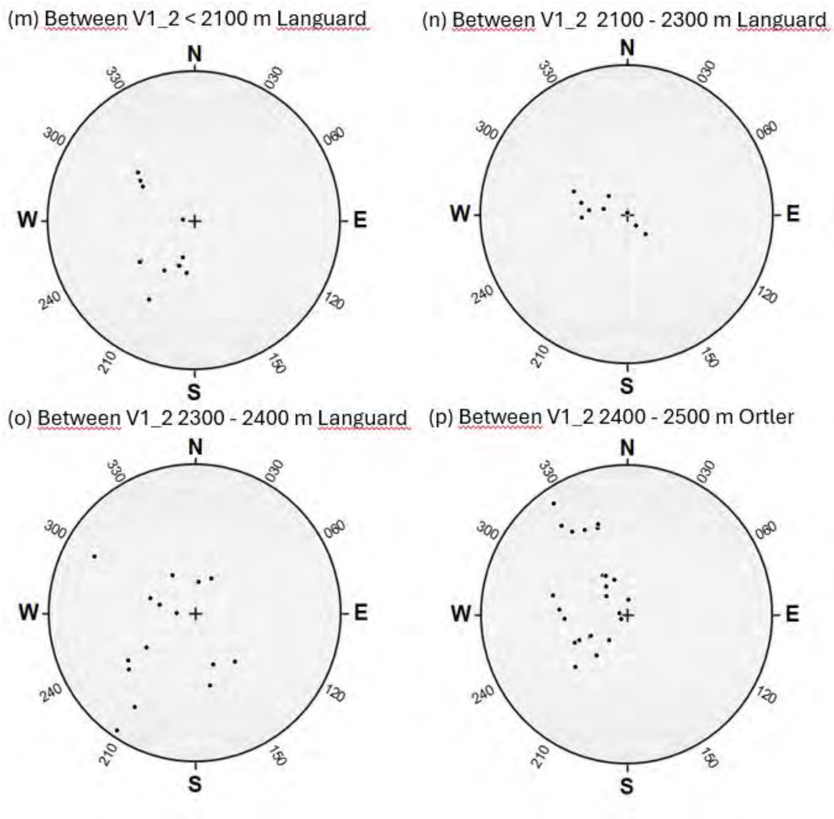

Figure 16: *Stereographic projection of fold data for the structural domain between Valley 1 (V1) and Valley 2 (V2) in different altitudes. Data and statistical best-fit calculations were generated utilizing Stereonet (Allmendinger et al., 2012; Cardozo and Allmendinger, 2013).*

6.1.3 Valley 2 (V2)

Valley 2 (V2) is entirely within the Languard nappe. Valley 2 (V2) is dipping NW on the west side and dipping east on the east side (lower section of V2 to NE, higher section of V2 to ENE) **(Table 6, Figure 17).** The stereonet representation shows strong clustering and strong deviations **(Figure 17).** The fold axes in the lower section calculated by the π-method or the beta-method **(Table 6)** show, however, similar values. When viewed down-plunge of the fold axes, the rotation of the structures is clockwise.

In the west of V2 a significant variation is observed: a primary axis trending 282° (WNW) and a plunge of 67° towards the Ortler/Languard nappe contact.

Stereonet	Section (m)	Trend	Plunge	Interpretation	Nappe
Calculated fold axes (bedding measurements)					
(q)	**ca. 2200 m (west)**	282°	67°	Fold axis plunging steeply toward the WNW, likely representing a lateral ramp or oblique shear.	Languard
(r)	**< 2150 m (east)**	124° 119°	17° (beta-method) 18° (π-method)	(beta method) (π-method)	Languard
(s)	**2150 m - 2200 m (east)**	142° 145°	13° (beta-method) 12° (π-method)	The plunging direction remains consistently toward the SE, though the spread suggests some folding or variation in the angle.	Languard

__Table 6:__ Fold axis analysis of the Valley 2 (V2). Calculations were performed using Stereonet (Allmendinger et al., 2012; Cardozo and Allmendinger, 2013).

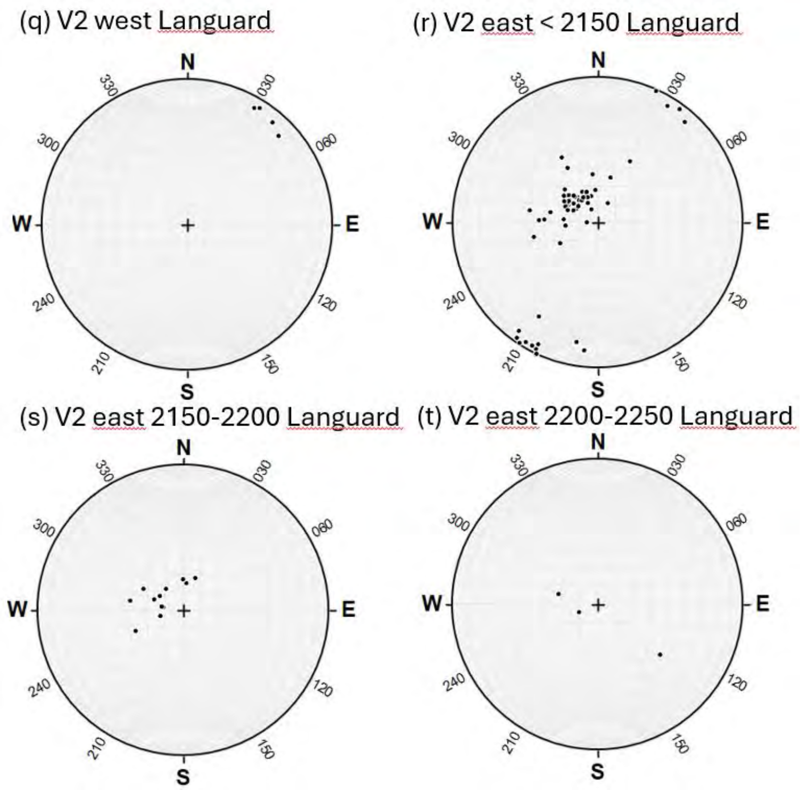

__Figure 17:__ Stereographic representation of structural data from Valley 2 (V2). Statistical processing and plotting were performed using Stereonet (Allmendinger et al., 2012; Cardozo and Allmendinger, 2013).

6.2 Micro- and Mesoscopic Characterization

The direction of movement in deformed metamorphic rocks can be determined by analyzing internal structures (cf. Passchier and Trouw, 2005). In the following chapter the main results are shown ordered by the type of identification. As identifications are similar in the microscopic and the mesoscopic scale, examples are shown from both. The complete thin section protocol is given in Appendix A, data for structural analysis in Appendix B.

S-C and S-C' Fabrics were used to determine the sense of shear based on the angular relationship between the primary shear surfaces (C-planes), the mylonitic foliation (S-planes) and the shear bands (C'-planes). In a ductile shear zone, the S-planes (foliation) represent the direction of maximum flattening, while the C-planes (shear bands) represent the actual planes of sliding. The acute angle between the S-plane and the C-plane points in the direction of the "top" block's movement. Mesoscopic examples from locality TS 1 (Campo) and TS 2 (Languard) indicated a top-to-the-WNW sense of shear **(Figure 18, Figure 19 b,c)**. In the location of TS 1, the presence of a steeper foliation (S 118/30) relative to the shear plane (C 119/17) and a shear band (C' 299/13) indicates a near-perfect dip-slip geometry, confirming that ductile deformation associated with the westward nappe transport extends significantly into the footwall units. In the location of TS 2 in 2031 m altitude (Valley 1), the geometric relationship between the shear plane (C 345/26) and the foliation (S 0/26) reveals a 15° angular divergence, providing mesoscopic evidence for a Top-NW sense of shear during the thrusting of the Ortler nappe. The C'-plane (263/11) is dipping to the west.

Figure 18: *Sample area TS1 (location marked in Figure 13). Strongly deformed fine-grained, foliated metamorphic rock of phylllitic composition (major minerals identified in the thin section: Quartz, Feldspar, Carbonates). White lines: NW-dipping shear bands (299/13).*

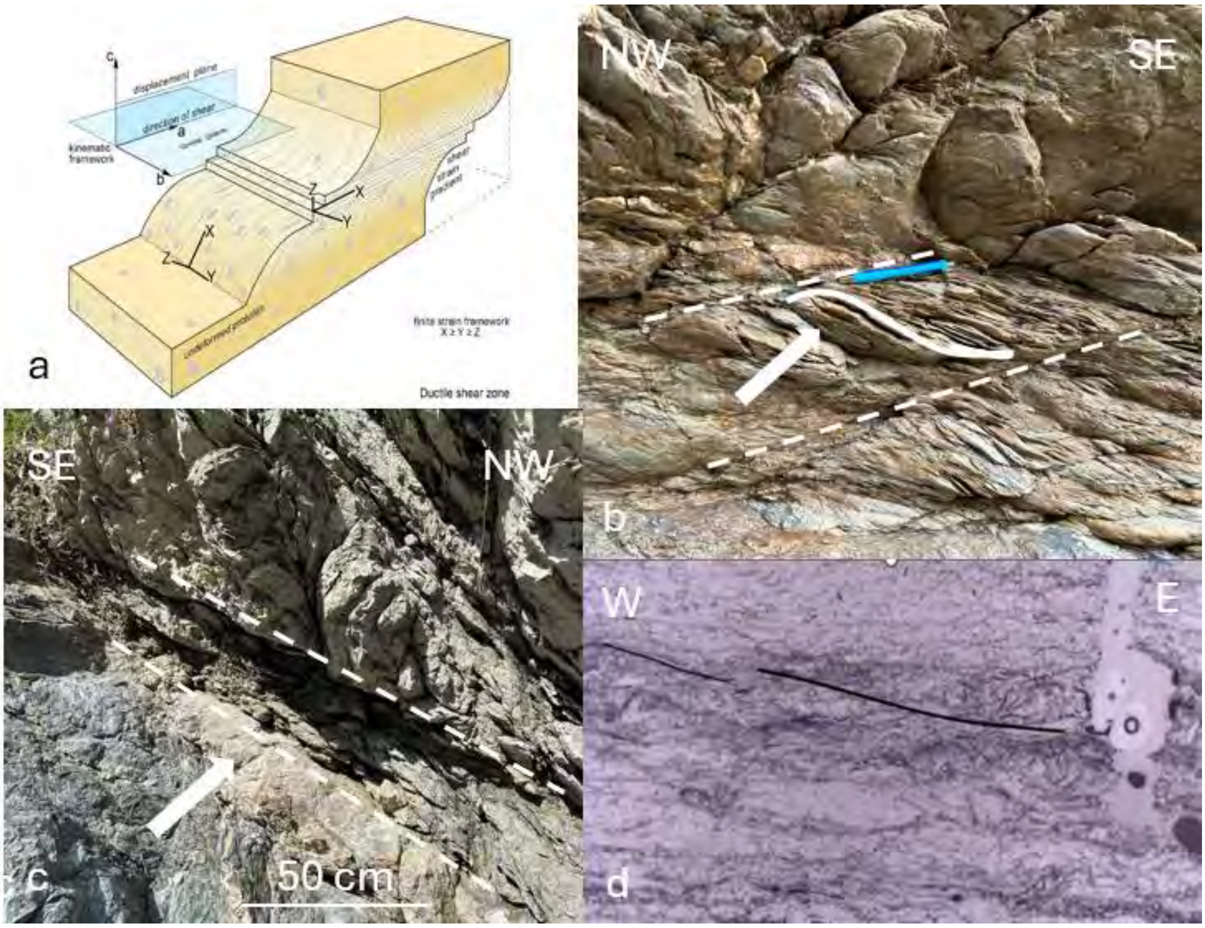

Figure 19: Multi-scale kinematic indicators within the investigated shear zone. (a) *Conceptual model of S-C fabric development in a ductile shear zone (modified after Burg, 2017).* ***(b)*** *Mesoscopic shear band at the TS 1 locality (Campo) indicating a top-to-the-WNW sense of shear (C 119/17 S 118/30 C' 299/13)* ***(c)*** *Outcrop overview displaying mesoscopic shear bands (W-dipping) at the TS 2 locality (C 345/26 S 0/26 C' 263/11) (Languard).* ***(d)*** *Photomicrograph of thin section TS 7 (Languard) (Plane-polarized light (PPL), 1.25× objective, Horizontal field width (HFW) is 9.86 mm) demonstrating a sinistral microscopic shear sense (Top-to-the-West). All corresponding sample and outcrop locations are mapped in Figure 13.*

Asymmetric Porphyroclasts: Rigid clasts (such as sigma-type) within a ductile matrix provided evidence of the rotational sense during deformation. Field observations of mesoscopic clasts consistently indicated Top-to-the-NW movement **(Figure 20,21)**.

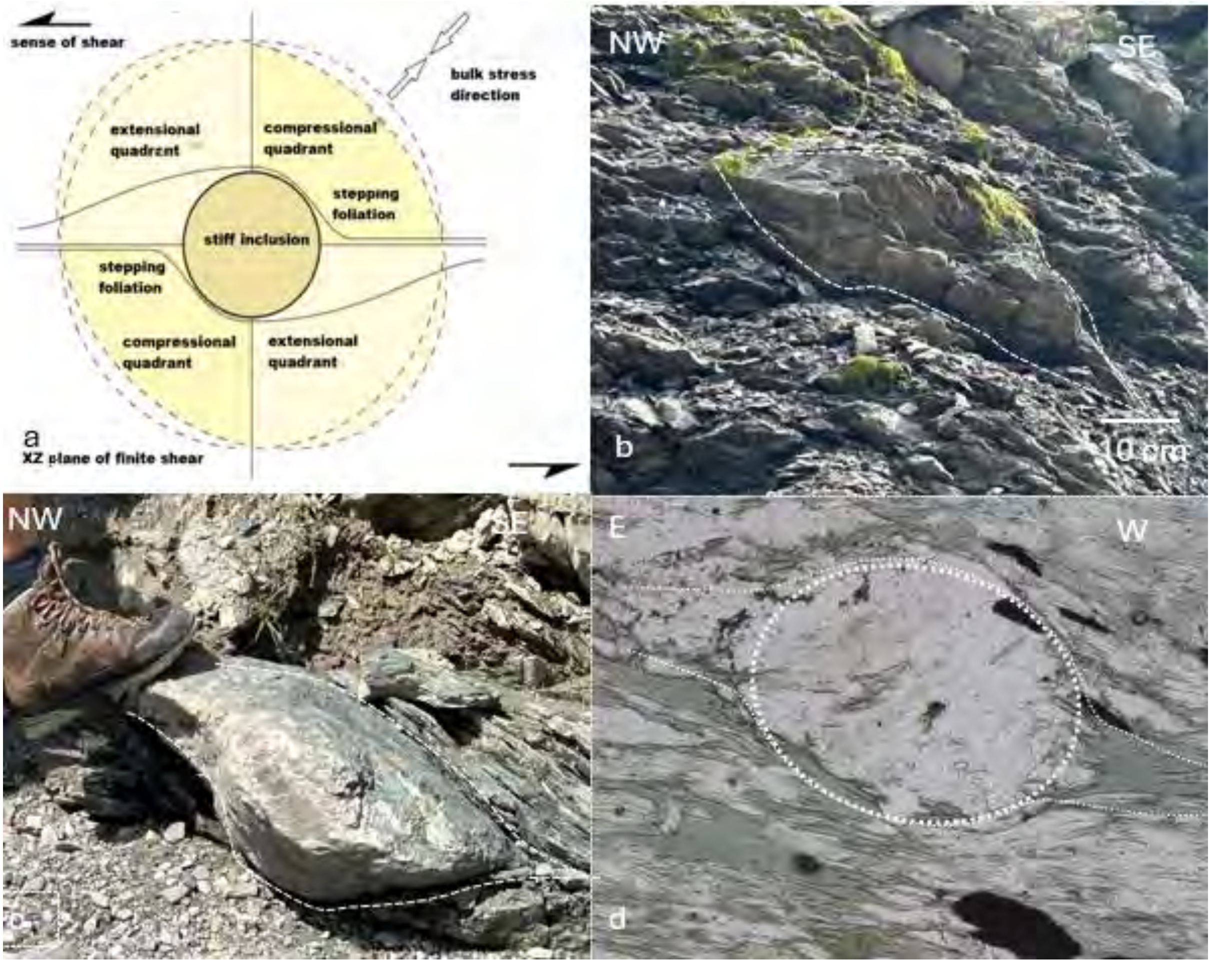

Figure 20: Rigid porphyroclasts as meso- and microscopic shear sense indicators. (a) *Incremental deformation quadrants in the perturbed flow of a soft matrix around a hard object (modified after Burg, 2017).* ***(b)*** *Field photograph of a macroscopic clast at locality clast 1 (Figure 13) (Languard), indicating Top to the NW (C 101/24 Clast Bruch 128/22).* ***(c)*** *Field photograph of a macroscopic clast at locality clast 2 (Figure 13) (Languard), indicating Top-to-the-W shear sense.* ***(d)*** *Microscopic view of thin section TS 3 (Languard) displaying a sinistral kinematic shear sense (here Top-to the E), however this sample show clasts (Albit) indicating both directions. (Plane-polarized light (PPL), 10× objective, Horizontal field width (HFW) is 1.24 mm). Spatial locations for all features are indicated in the overview map (Figure 13). White dotted lines trace the clast and the strain window.*

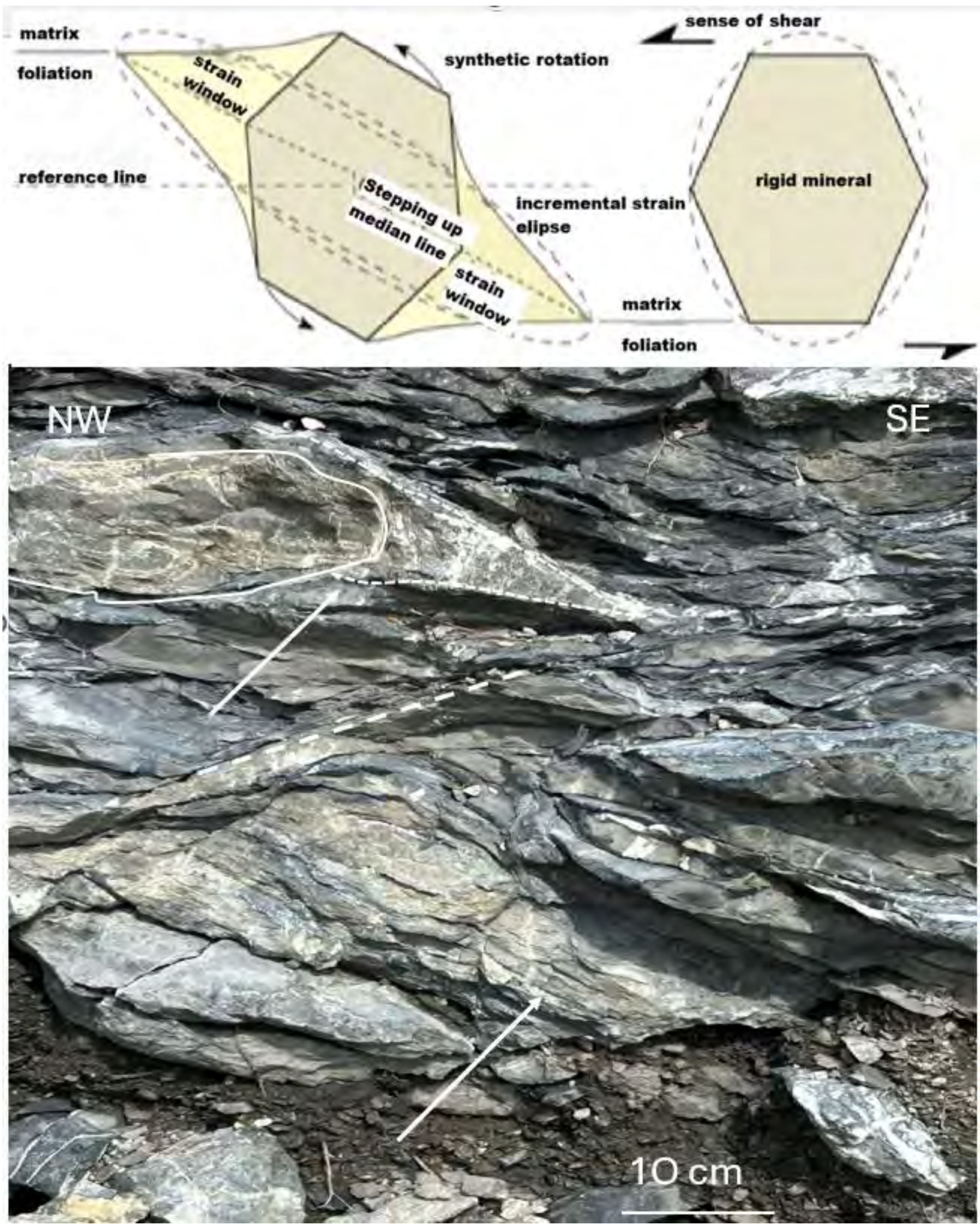

Figure 21: Rotation of rigid clasts during ductile deformation. ***(Top)*** *Theoretical model depicting the kinematic rotation of rigid minerals within a soft matrix (modified after Burg, 2017).* ***(Bottom)*** *Mesoscopic view of a rotated clast at locality clast 1 (Figure 13) (Languard). Arrows indicating clasts and strain window. Straight dotted line, shear band dipping towards NW (280/30). Shear sense Top-to-NW. Spatial coordinates for both sampled locations are marked in Figure 13.*

Rotated Porphyroblasts: Helical inclusion trails (snowball structures) within minerals were analyzed using the string-cylinder model to establish the rotation sense during syn-kinematic growth **(Figure 22)**.

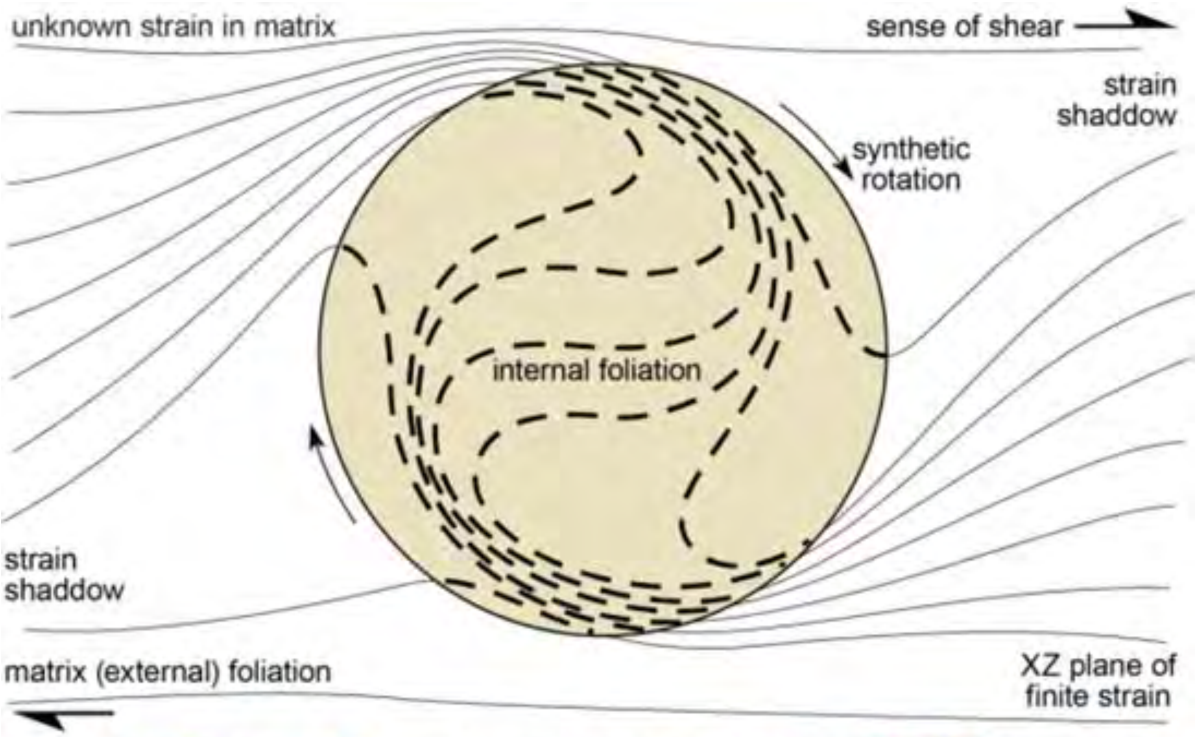

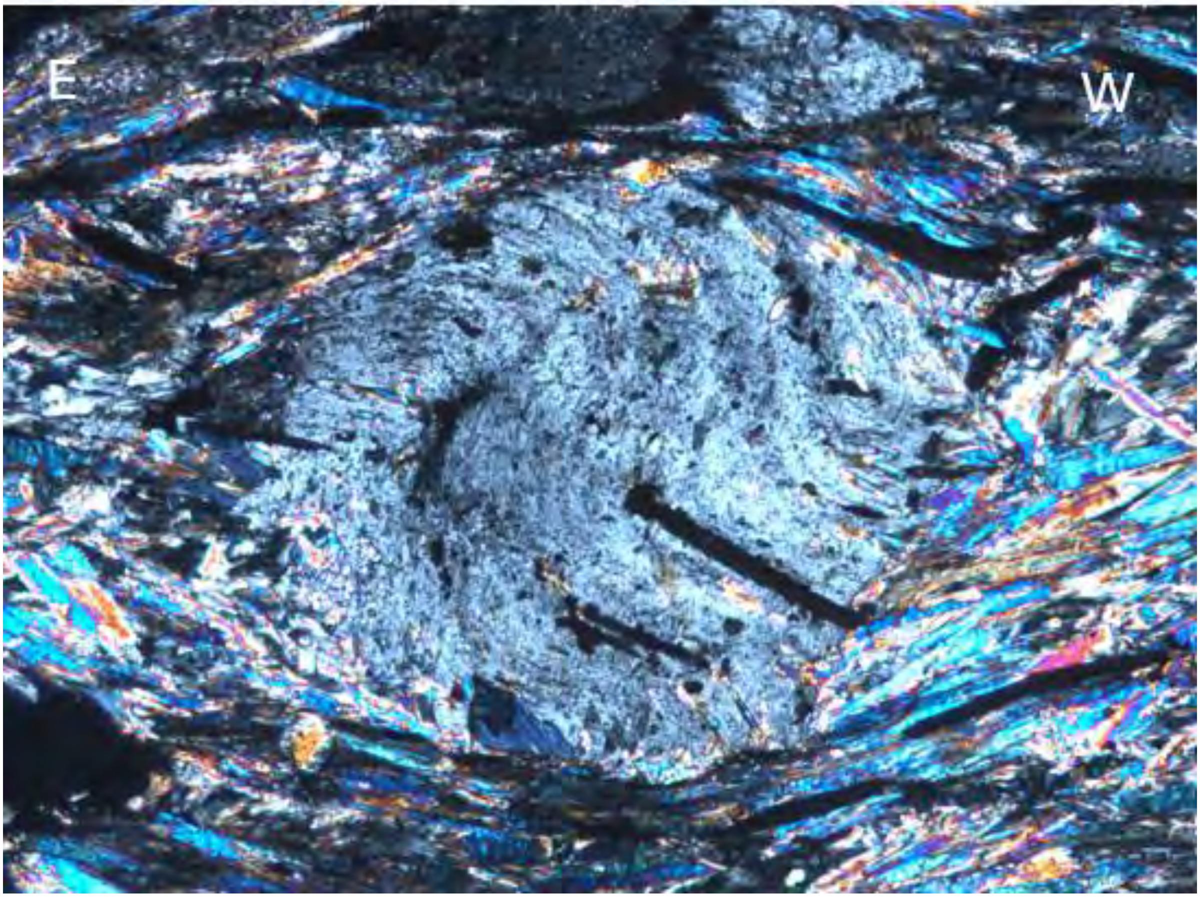

Figure 22: *Helical inclusion trails preserved within a porphyroblast interpreted using the string-cylinder model of Schoneveld (1977). The model illustrates rotation of a rigid porphyroblast within a ductile shear zone, producing curved internal. Bottom: Thin section 7 (Languard) showing clast (Albit) indicating Top-to-the West movement. The helical inclusion trails within the porphyroblast indicate a rotational strain path that differs from the final orientation of the surrounding matrix foliation (Crossed-polarized light (XPL), 10× objective, Horizontal field width (HFW) is 1.24 mm). Spatial coordinates for both sampled locations are marked in Figure 13.*

Brittle-Ductile Mechanisms: The "Bookshelf Gliding" mechanism, where rigid clasts undergo microboudinage and brittle fracturing before rotating into easy-slip orientation was used to identify strain localization and the sense of displacement **(Figure 23)**.

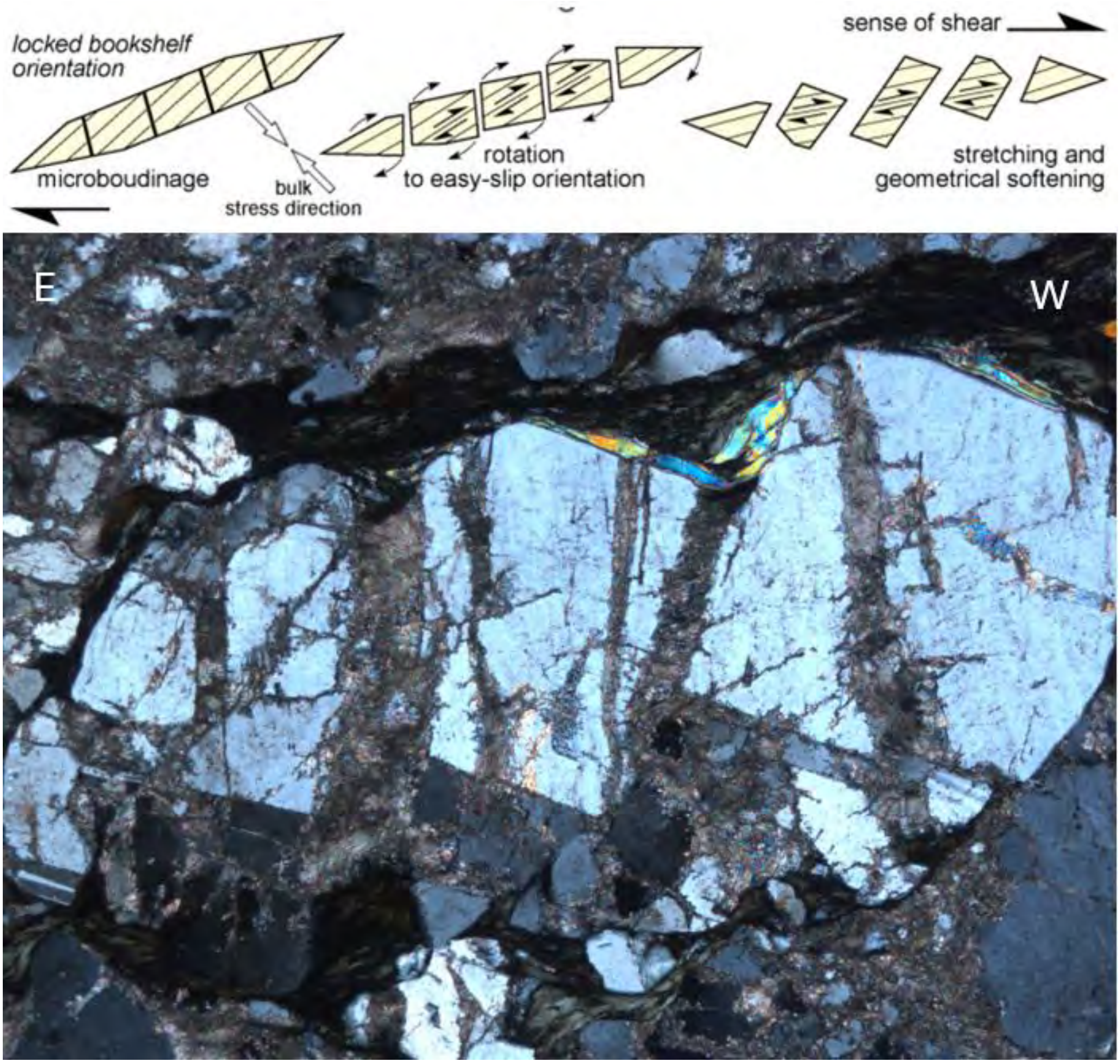

Figure 23: (Top) Conceptual model illustrating deformation-induced softening in a ductile shear zone through grain fragmentation and rotation (modified after Etchecopar, 1977). Initially "locked" grains in an unfavourable orientation undergo microboudinage and progressive fragmentation under bulk stress. Subsequent rotation toward an easy-slip orientation reduces internal resistance, promoting strain localization. Continued stretching and geometrical softening enhance deformation in the direction of shear. The model highlights the role of boundary processes in facilitating mechanical weakening during non-coaxial deformation, (bottom) Thin section 6 (Languard): Top-to-the W (Quarz grain). (Crossed-polarized light (XPL), 5× objective, Horizontal field width (HFW) is 2.49 mm). Spatial locations for all features are indicated in the overview map (Figure 13).

Fold Geometries: *Asymmetric micro- and mesoscopic folds were documented, though interpreted with caution, to support kinematic determinations (Figure 24).*

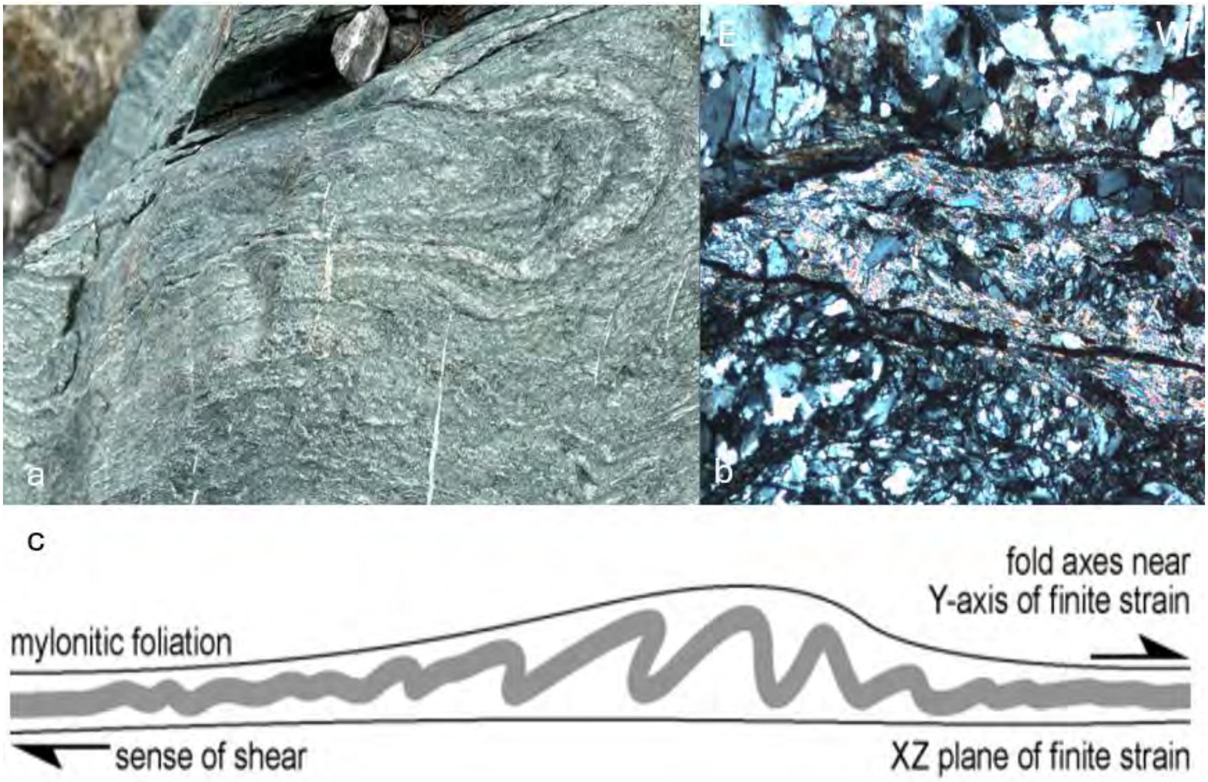

***Figure 24**: **Micro- and mesoscopic Folds from two different locations (a)** Mesoscopic fold observed in the field, fold top to the West: but not clear to identify shear sense **(b)** Microscopic view of thin section TS 2 displaying a top-to-the-E fold asymmetry. Both directions were found in TS 2 (location indicated in Figure 13) (Crossed-polarized light (XPL), 5× objective, Horizontal field width (HFW) is 2.49 mm). **(c)** Theoretical model of fold kinematics (after Burg, 2017). Fold geometry needs to be treated with caution: Overall thin section 2 is identified as top-to the West based mostly on shear bands.*

6.3 Petrographic Analysis and Mineral Assemblages

6.3.1 Lithology and Mineral Assemblages

Thin section analysis of the mineral assemblage in the samples shows a range from phyllites to chlorite-muscovite schists and locally calc-silicate rocks. Grain size and the degree of recrystallization vary between samples, with finer-grained phyllitic textures in some sections and coarser, more strongly recrystallized schistose fabrics in others (for detail see Appendix A).

The samples consist predominantly of quartz, albite, white mica, and chlorite, with variable carbonate content and accessory phases including tourmaline, zircon, apatite, epidote, titanite, rutile, pyrite, and ilmenite. Secondary minerals such as limonite and leucoxene occur locally as products of late-stage alteration.

6.3.2 Texture and Deformation Structures

All samples show a foliation defined by the preferred orientation of white mica and chlorite, accompanied by elongation and recrystallization of quartz and, locally, feldspar. In many sections, compositional banding - consisting of alternating quartz-feldspar-carbonate domains and mica-rich layers - has developed. These fabrics represent primary sedimentary layering that was rearranged into mineral bands by intense deformation and metamorphic separation.

Microstructures indicate deformation under ductile conditions. Quartz commonly shows undulose extinction, subgrain formation, and dynamic recrystallization, locally forming elongate ribbons or mosaic textures. Porphyroclastic feldspar and albite grains frequently display internal deformation and alignment parallel to the foliation. In several samples, microfolds, shear bands, and displaced clasts provide kinematic indicators, documenting both sinistral and dextral shear. The presence of multiple foliations in some thin sections further suggests a polyphase deformation history (e.g. TS 1).

6.3.3 Metamorphic Conditions

Mineral assemblages indicate greenschist-facies metamorphism. The widespread coexistence of quartz, muscovite, chlorite, and albite, combined with the general absence of higher-grade index minerals such as garnet or amphibole, indicates metamorphic temperatures in lower to intermediate greenschist-facies range **(Table 7, cf. Figure 13).** Quartz recrystallization and ribbon development indicate temperatures above approximately 280 °C, while the absence of extensive feldspar recrystallization and the persistence of chlorite suggest temperatures generally below approximately 400 °C (cf. Marshak, 2019). In one sample (TS 4, Languard, ca. 2040 m altitude), minor biotite indicates locally slightly higher temperatures approaching the upper part of the lower greenschist field. TS 4 is located within the Languard close to the Ortler nappe contact.

6.3.4 Protoliths

The protoliths are predominantly siliciclastic sediments, including pelitic to semi-pelitic mudstones and siltstones, as well as feldspar-rich sediments such as arkosic siltstones or graywackes. Variations in feldspar abundance and the presence of accessory minerals such as tourmaline and zircon suggest heterogeneous sediment sources and, in some cases, volcaniclastic contributions. Carbonate-bearing samples originated from calcareous sediments or mixed carbonate-siliciclastic deposits, whereas calc-silicate assemblages indicate impure limestone or marl protoliths.

6.3.5 Metamorphic and Tectonic Evolution

The samples record a sequence of processes beginning with sediment deposition, followed by burial and regional metamorphism under greenschist-facies conditions. Ductile deformation produced foliation, compositional banding, and quartz recrystallization. Overprinting foliations and opposing shear indicators suggest polyphase deformation. Finally, late-stage fluid interaction and weathering processes produced oxidation features such as limonite and alteration of ilmenite to leucoxene. The summary of the results are given in **Table 7** and the trends in **Table 8**.

.

Sample	Nappe	Rock type / Classification	Main minerals	Metamorphic facies	Protolith interpretation	Deformation / Structural features	Notable features
1	Campo	Phyllite (feldspar-bearing, possible volcaniclastic component)	Quartz, muscovite, feldspar, carbonate; rutile, pyrite, ilmenite	Lower greenschist facies.	Volcaniclastic or tuffaceous sediment	Two foliations (S1, S2) indicating polyphase deformation; ductile deformation	Unusually thin section; limonite alteration; feldspar abundance atypical for phyllite. **Overall shear sense:** Top-to-the-W
2	Languard	Chlorite–muscovite schist	Quartz, muscovite, Fe-chlorite, minor carbonate	Lower greenschist facies (~280–350 °C).	Pelitic to semi-pelitic sediment	Sinistral microfolds; strong foliation	Recrystallized quartz ribbons; consistent shear sense indicators **Overall shear sense:** Top-to-the-W
3	Languard	Carbonate–quartz–chlorite schist with albite	Quartz, carbonate, chlorite, muscovite, albite; tourmaline, zircon, apatite	Greenschist facies	Mixed carbonate–siliciclastic sediment; possible volcaniclastic input	Ductile deformation; aligned albite clasts	Pronounced compositional banding; zircon disrupting chlorite layers **Overall shear sense:** Top-to-the-E
4	Languard	Biotite-bearing chlorite phyllite	Chlorite, muscovite, quartz, albite; minor biotite	Lower greenschist facies (locally higher temperatures – 400 °C).	Pelitic to semi-pelitic sediment	Strong schistosity; preferred mineral alignment	Biotite indicates slightly higher temperatures; carbonate absent **Overall shear sense:** unclear
5	Languard	Quartz–feldspar–chlorite schist (carbonate-bearing)	Quartz, albite, microcline, chlorite, muscovite, carbonate; epidote	Low–mid greenschist facies.	Feldspar-rich siliciclastic sediment (arkosic)	Continuous foliation; ductile deformation	Epidote present; ilmenite altered to leucoxene **Overall shear sense:** Top-to-the-E

Sample		Rock type / Classification	Main minerals	Metamorphic facies	Protolith interpretation	Deformation / Structural features	Notable features
6	Languard	Calc-silicate chlorite schist / calc-silicate rock	Carbonate, quartz, feldspar, chlorite, epidote	Lower greenschist (~300–350 °C)	Calcareous sediment or impure limestone	Cataclastic and ductile deformation; mylonitic quartz	Coexisting Mg- and Fe-chlorite; shear sense unclear **Overall shear sense:** unclear
7	Languard	Quartz–feldspar–chlorite schist (coarse muscovite)	Quartz, albite, chlorite, muscovite; minor carbonate, epidote	Greenschist facies (~300 - 400 °C)	Feldspathic sediment (arkosic siltstone or graywacke)	Strong schistosity; sinistral shear indicators	Coarser grain size than phyllites; pronounced compositional layering **Overall shear sense:** Top-to-the-W

*Table 7: **Summary of petrographic and microstructural results.** The table synthesizes the primary mineral assemblages, dominant ductile deformation mechanisms, and deduced kinematic shear sense for each analyzed thin section (TS 1 to TS 7). Spatial locations of the samples within the shear zone profile are provided in Figure 13.*

.

Parameter	Observed trend	Interpretation
Metamorphic grade	All samples fall within greenschist facies; most in the lower greenschist field, with slight local increase where biotite appears	Regional low-grade metamorphism under broadly similar P-T conditions
Grain size and recrystallization	Phyllitic textures (TS1, TS4) → more recrystallized schists (TS5, TS7)	Variation reflects differences in strain intensity and recrystallization rather than major grade differences
Foliation and fabric development	Strong foliation present in all samples; schistosity increases with grain size and mica content	Progressive deformation and mica recrystallization during ductile strain
Compositional banding	Common in most samples; especially pronounced in TS3, TS5, TS7	Likely reflects transposed bedding and metamorphic differentiation during deformation
Quartz microstructures	Undulose extinction, subgrain formation, and locally ribbon quartz	Deformation at greenschist-facies temperatures with dynamic recrystallization
Carbonate content	Variable: absent or minor in some phyllites; abundant in calc-silicate sample (TS6)	Differences controlled primarily by protolith composition
Feldspar abundance	Present in all samples, locally abundant (albite-dominated)	Indicates feldspar-rich siliciclastic or volcaniclastic sediment sources
Accessory minerals	Tourmaline, zircon, epidote, apatite, titanite present in several samples	Suggest heterogeneous sediment sources and fluid interaction during metamorphism

Parameter	Observed trend	Interpretation
Deformation style	Predominantly ductile; local cataclastic features in TS6	Deformation occurred at relatively low temperatures, locally overprinted by brittle processes
Shear sense indicators	Both sinistral and dextral indicators observed in different samples	Evidence for polyphase deformation or changing kinematic regimes
Alteration and retrogression	Limonite, leucoxene, and fracture-controlled alteration common	Late-stage fluid circulation and oxidation after peak metamorphism
Protolith variability	Pelitic, semi-pelitic, arkosic, carbonate-bearing, and volcaniclastic inputs	Sedimentary sequence with compositional heterogeneity prior to metamorphism

Table 8: ***Synthesis of Petrographic Trends Across the Thin Sections*** *A systematic comparison of the microstructural features of the thin sections (TS 1 – TS7).*

7. Discussion

This study investigates the structural geometry and kinematics of nappe contacts within the Ortler-Campo nappe complex near Livigno in the Central Alps. The research question was to determine the transport direction and deformation history associated with the reactivation of the Albula–Zebrù movement zone through structural mapping, stereographic analysis, and micro-/mesostructural investigation.

Field measurements combined with structural analysis within the Campo, Languard and Ortler nappes show a systematic variation in the fold-axis orientation and in the stretching lineations. In valley 1 (V1) **(Table 3,4; Figure 14,15)**, fold axes show, based on the direction of the down plunge, a progressive counterclockwise rotation toward the Languard/Ortler nappe contact (160°/13° to 69°/15°). Using data from the Ortler nappe throughout the study area reveals an average fold axis of 77°/16°, comparable to the data obtained in valley 1 (V1) for the Ortler nappe. Near the Languard/Ortler nappe contact fold axes shift toward the NE aligning with the stretching lineations (transport direction).

Calculation of the fold axes based on foliation in the Campo nappe (111°/2°) and the Languard nappe (286°/4°) shows divergence, which could be a direct result of the tectonic transport. As the Ortler nappe moved towards the Northwest, the underlying rock fabric was progressively 'dragged' and reoriented in the transport direction. Stretching lineations (Campo 136°/20° and Languard (from 128°/8° to 108°/6°) display a similar rotation and progressively align with an ESE-WNW direction toward the contact. This pattern indicates increasing strain intensity toward the Languard/Ortler nappe contact and reflects progressive reorientation of structures into the transport direction. The lineation **(Table 4, Figure 15)** is rotating with a low plunge, characteristic of a near-horizontal nappe-dominated structural regime. Average lineation (109°/6°) at the Ortler/Languard nappe contact is a solid indicator of the transport directions. Kinematic modeling reveals an ENE-trending fold axis (77°/16°), oriented at an angle of 32° to the lineation. In low-strain environments, these features are typically 90° apart. The reduction to 32° indicates significant rotation of the fold axis toward the transport direction, indicating a regime of high stress and high strain. The structural data illustrates a clear strain gradient towards the nappe contact. While lineations in the deeper, lower-strain footwall record a partial reorientation, the lineations towards the thrust contact

are fully rotated into the WNW transport direction of the overriding nappe.
Between V1-V2 of the study area **(Table 5, Figure 16)**, which is mainly within the Languard nappe, oscillatory behavior suggests a high-strain environment between two stress regimes. The sharp rotation observed in the section of 2300 m could mark a lithological or mechanical boundary where the earlier deformation history is locally preserved. Despite these sharp lateral shifts in direction, the plunge remains consistently gentle, maintaining a sub-horizontal inclination between 3° and 22°.
The steep bedding on the west side of Valley 2 (V2) **(Table 6, Figure 17)** could indicate a lateral ramp or an oblique shear zone where material is forced to "climb" or escape laterally. Overall, the geometries in valley 2 (V2) could indicate different deformation regimes related to the Albula–Zebrù movement zone. The east side shows calculated values of the fold axis of 119°/18° - 145°/12° which are comparable with the values obtained in valley 1 (V1).

Mesoscopic and microscopic kinematic indicators provide evidence for W to WNW directed transport. S-C fabrics **(Figure 18, 19)**, asymmetric porphyroclasts **(Figure 20)**, and rotated clasts **(Figure 21, 22)** predominantly indicate a top-to-the-WNW sense of shear in the Campo and the Languard nappe. Thin sections show different shear indicators on a local scale, not contradicting the top-to-the-WNW transport direction. At the millimetric scale, deformation could be non-homogenous.

The protoliths of the studied rocks were predominantly siliciclastic sediments including pelitic to semi-pelitic mudstones and feldspar-rich sediments, with local carbonate-bearing and calc-silicate lithologies. Subsequent burial, metamorphism, and ductile deformation produced the observed foliations, compositional banding, and shear fabrics.

Petrographic analysis **(Table 7)** indicates that tectonic transport occurred under lower greenschist-facies conditions (280 °C – 400 °C). The dynamic quartz recrystallization (starting at ca. 280 °C), the stability of chlorite (Mg and Fe rich), feldspar and the occurrence of prograde biotite in only one thin section (TS 4) suggests that temperatures generally remained close to the biotite-in isograd. The temperature range is therefore approximately 280 - 400 °C (cf. Marshak, 2019). Overprinting foliations and opposing shear indicators in the thin sections suggest polyphase deformation.

8. Conclusion

Structural and kinematic analysis across the nappe contact near Livigno confirms a dominant Top-to-the-WNW tectonic transport direction (reverse kinematic). Mesoscopic and microscopic kinematic indicators, including S-C fabrics and asymmetric porphyroclasts, provide consistent evidence for this WNW thrusting of the Ortler nappe over the Campo and Languard units. Systematic measurements reveal a strong structural convergence toward the contact, where fold axes rotate toward the transport direction, indicating a high-strain regime.

Petrographic evidence indicates that this deformation occurred under lower greenschist-facies conditions, with temperatures estimated between 280 – 400 ° C. The occurrence of prograde biotite in only one thin section suggests that temperatures generally remained close to the biotite-in isograd.

9. References

Allmendinger, R. W., Cardozo, N., & Fisher, D. M. (2012). Structural geology algorithms: Vectors and tensors. Cambridge University Press.

Allmendinger, R. W. (2026). Stereonet 11. [Software]. Available at: rickallmendinger.net. Accessed: [1.10.2025].

Cardozo, N., and Allmendinger, R. W., (2013). Spherical projections with OSXStereonet. Computers & Geosciences, v. 51, 193–205. https://doi.org/10.1016/j.cageo.2012.07.021

Bearth, P., Heierli, H., and Roesli, F., (1987). Blatt Nr. 1237 Albulapass. Geologischer Atlas der Schweiz 1:25'000, Karte 81. Bundesamt für Wasser und Geologie, Bern.

Bernoulli, D., Dall'Agnolo, S., Fantoni, R., Gouffon, Y. (Hrsg.), Jordan, P., Madritsch, H., Mosar, J., Picotti, V., Pfiffner, O. A., Schenker, F. L., Schlunegger, F., & Schmid, S. M. (2024). Tectonic map of Switzerland: explanatory notes. Swiss Geological Survey, Federal Office of Topography Swisstopo.

Bigi, G., Cosentino, D., Parotto, M., Sartori, R., & Scandone, P. (1990). Structural model of Italy. 1:500,000 . Explanatory notes. Consiglio Nazionale delle Ricerche, Progetto Finalizzato Geodinamica, Roma.

Bonsignore, G., Borgo, A., Gelati, R., Montrasio, A., Potenza, R., Ragni, U., and Schiavinato, G., (1969a). Carta Geologica d'Italia, Foglio 8, Bormio 1:100'000. Servizio Geologico d'Italia.

Bonsignore, G., Borgo, A., Gelati, R., Montrasio, A., Potenza, R., Ragni, U., and Schiavinato, G., 1969b. Note illustrative della Carta Geologica d'Italia, Foglio 8, Bormio.

Boyer, S. E., & Elliott, D. (1982). Thrust systems. AAPG Bulletin, 66(9), 1196–1230.

Burg, J.-P., Galli, A., & Schenker, F. L. (2016). Migmatization and deformation in the Southern Steep Belt of the Central Alps. Field Guide, 20th July 2016

Burg, J.-P. (2017). Structural Geology. Vorlesungsskript, ETH Zürich, Institut für Geophysik.

Cornelius, H. P., (1932). Geologische Karte der Err-Julier-Gruppe 1:25'000. Schweiz. geol. Komm. Spezialkarte 115a.

Cornelius, H. P., (1935). Geologie der Err-Julier-Gruppe: Das Baumaterial. Beiträge zur Geologischen Karte der Schweiz, NF 70/1, 1–321.

Cornelius, H. P., (1950). Geologie der Err-Julier-Gruppe: Der Gebirgsbau. Beiträge zur Geologischen Karte der Schweiz, NF 70/2, 264

Conti, P. (1992). Tettonica delle falde austroalpine nelle Dolomiti dell'Engadina: un'ipotesi di lavoro. Atti Ticinesi di Scienze della Terra, 35, 61–66.

Conti, P., Manatschal, G., & Pfister, M. (1994). Synrift sedimentation, Jurassic and Alpine tectonics in the central Ortler nappe (Eastern Alps, Italy). *Eclogae Geologicae Helvetiae*, 87(1), 63–90.

Conti, P. (1997). The austroalpine Ortler nappe and the tectonic evolution of the Engadine Dolomites (Switzerland-Italy). Memorie Descrittive della Carta Geologica d'Italia, 53, 102 pp.

Dewey, J. F., & Bird, J. M. (1970). Mountain belts and the new global tectonics. Journal of Geophysical Research, 75(14), 2625–2647.

Dewey, J. F., Helman, M. L., Turco, E., Hutton, D. H. W., & Knott, S. D. (1989). Kinematics of the western Mediterranean. Geological Society, London, Special Publications, 45(1), 265–283.

Etchecopar, A. (1977). A study of boundary processes involving grain fragmentation and rotation. Tectonophysics, 39(1–3), 121–139.

Fossen, H. (2016). Structural geology (2. Aufl.). Cambridge University Press.

Froitzheim, N., Schmid, S. M., & Conti, P. (1994). Repeated change from crustal shortening to orogen-parallel extension in the Austroalpine units of Graubünden. Eclogae Geologicae Helvetiae, 87, 559–612.

Handy, M. R., Schmid, S. M., Bousquet, R., Kissling, E., & Bernoulli, D. (2010). Reconciling plate-tectonic reconstructions of Alpine Tethys with the geological–geophysical record of spreading and subduction in the Alps. Earth-Science Reviews, 102(3), 121–158.

Hansmann, W. (1996). Age determinations on the Tertiary Bregaglia (Bergell) intrusive rocks (Central Alps): a review. Schweizerische Mineralogische und Petrographische Mitteilungen, 76(3), 421-451.

Kempf, O., Pross, J. (2005). The Lower Marine to Lower Freshwater Molasse transition in the northern Alpine foreland basin (Oligocene; central Switzerland-south Germany): age and geodynamic implications. International Journal of Earth Sciences, 94, 160–171.

Liniger, M. H., (1992). Der Ostalpin-Penninische Grenzbereich im Gebiet der Nördlichen Margna-Decke (Graubünden, Schweiz). Unpublished PhD thesis, ETH Zürich, p. 1–186.

Lisle, R. J., & Leyshon, P. R. (2004). Stereographic Projection Techniques for Geologists and Civil Engineers. Cambridge University Press.

Marshak, S. (2019). Earth: Portrait of a planet (6th international student ed.). W. W. Norton & Company.

Meier, A., (2003). The Periadriatic fault system in Valtellina (N-Italy) and the evolution of the southwestern segment of the Eastern Alps. Unpublished PhD thesis, ETH Zürich

Mohn, G., Manatschal, G., Masini, E., and Müntener, O., (2011). Rift-related inheritance in orogens: a case study from the Austroalpine nappes in Central Alps (SE-Switzerland and N-Italy). *International Journal of Earth Sciences*, v. 100, 937–961.

Montrasio, A., Crespi, R., Boriani, A., Bonsignore, G., Ragni, U., et al., (1969). *Carta Geologica d'Italia, Foglio 19, Tirano 1:100'000*. Servizio Geologico d'Italia.

NASA Shuttle Radar Topography Mission (SRTM) (2013). Shuttle Radar Topography Mission (SRTM) Global. Distributed by OpenTopography. https://doi.org/10.5069/G9445JDF. Accessed: 13.1.2026.

Oberhänsli, R., Bousquet, R., Engi, M. et al. (2004). Metamorphic structure of the Alps. In: Explanatory notes to the map „Metamorphic Structure of the Alps“. Commission for the Geological Map of the World.

OpenTopography (2026). High-Resolution Topography Data and Tools. San Diego Supercomputer Center (SDSC). https://opentopography.org. (Accessed: 10.1.2026).

Passchier, C. W., & Trouw, R. A. J. (2005). Microtectonics (2. Aufl.). Springer.

Peters, T., (2005). Blatt Nr. 1257 St. Moritz. Geologischer Atlas der Schweiz 1:25'000, Karte 118. Bundesamt für Wasser und Geologie, Bern.

Peters, T., (2007). Blatt Nr. 1256 Bivio. Geologischer Atlas der Schweiz 1:25'000, Karte 124. Bundesamt für Wasser und Geologie, Bern.

Pfiffner, O. A. (2024). Geologie der Alpen (2. Aufl.). Wiley-VCH.

QGIS Development Team (2026). *QGIS Geographic Information System*. QGIS Association. http://www.qgis.org. Accessed: [1.10.2025].

Savostin, L.A., Sibuet, J.C., Zonenshain, L.P., Le Pichon, X., Roulet, M.J. (1986). Kinematic evolution of Tethys belt from the Adriatic Ocean to the Pamirs since the Triassic. Tctonophysics, 123, 1–35.

Schmid, S. M., & Haas, R. (1989). Transition from near-surface thrusting to intrabasement decollement, Schlinig thrust, Eastern Alps. *Tectonics*, 8(4), 697-718. https://doi.org/10.1029/TC008i004p00697

Schmid, S. M., & Froitzheim, N. (1993). Oblique slip and block rotation along the Engadine Line. Eclogae Geologicae Helvetiae, 86, 569–593.

Schmid, S. M., Pfiffner, O. A., Schönborn, G., Froitzheim, N., and Kissling, E. (1997). Integrated cross section and tectonic evolution of the Alps along the Eastern Traverse. In: Deep Structure of the Swiss Alps: Results of NRP 20. Birkhäuser Basel, pp. 289–304.

Schmid, S. M., Fügenschuh, B., Kissling, E. & Schuster, R. (2004). Tectonic map and overall architecture of the Alpine orogen. Eclogae Geologicae Helvetiae, 97(1), 93–117.

Schoneveld, C. (1977). A study of the mechanical behaviour of garnet porphyroblasts in a ductile shear zone (string-cylinder model). Tectonophysics, 39(1–3), 453–471.

Schuster, R., Kurz, W., Krenn, K., & Fritz, H. (2013). Introduction to the Geology of the Eastern Alps. Berichte der Geologischen Bundesanstalt, 99, 5–19.

Spillmann, P., (1993). Die Geologie des penninisch-ostalpinen Grenzbereichs im südlichen Berninagebirge. Unpublished PhD thesis, ETH Zürich, No. 10175.

Spillmann, P., and Trommsdorff, V., (2005**).** Blatt Nr. 1277 Piz Bernina. Geologischer Atlas der Schweiz 1:25'000, Karte 119. Bundesamt für Wasser und Geologie, Bern.

Spitz, A. & Dyhrenfurth, G. (1914). Monographie der Engadiner Dolomiten. Beiträge zur Geologischen Karte der Schweiz, 44.

Staub, R. (1946). Geologische Karte der Bernina-Gruppe 1:50,000. Speyer & Kaerner.

Swisstopo (Bundesamt für Landestopografie) (2026): Geologische Vektordaten und Kartenportale. [Online-Daten abgerufen am 14.01.2026]. URL: https://map.geo.admin.ch

Thöni, M. (2006). Dating eclogite-facies metamorphism in the Eastern Alps – approaches, results, interpretations: a review. Mineralogy and Petrology, 88, 123–148.

Trommsdorff, V., Montrasio, A., Hermann, J., Müntener, O., Spillmann, P., and Gieré, R., (2005). The geological map of Valmalenco. *Schweizerische Mineralogische und Petrographische Mitteilungen*, v. 85, 1–13.

Von Blanckenburg, F. & Davies, J. H. (1995). Slab breakoff: A model for syncollisional magmatism and tectonics in the Alps. Tectonics, 14, 120–131.

Appendix A: Thin Section

For image size determination and scale calculations, refer to the instrumentation table in **Appendix C**.

1. Thin section 1 (sinistral, Top-W):

Figure 1: Thin section 1: scan. Top left W, top right E.

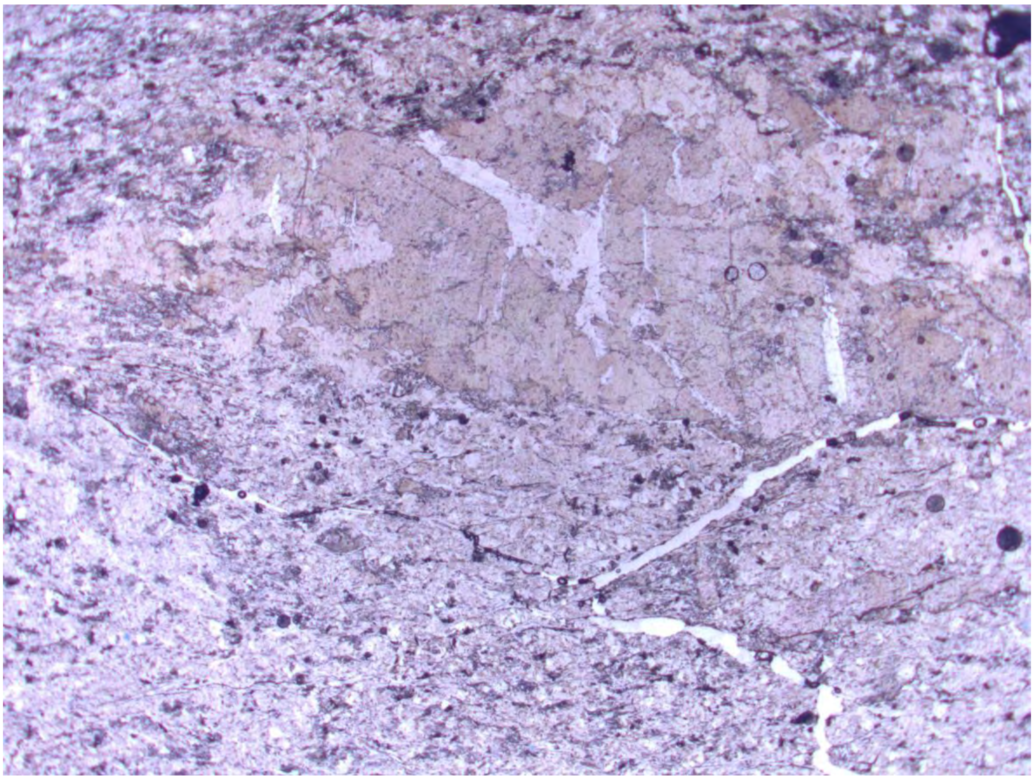

Figure 2: Thin section 1: Plane-polarized light (PPL), 1.25× objective.

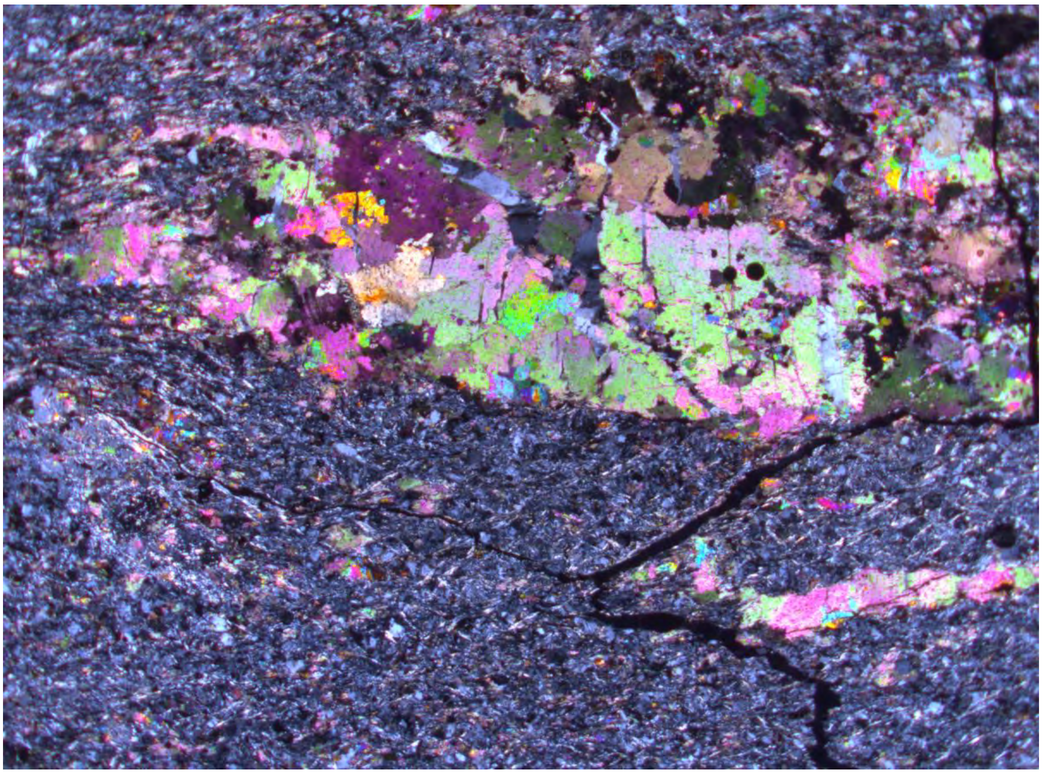
Figure 3: Thin section 1: Crossed-polarized light (XPL), 1.25× objective.

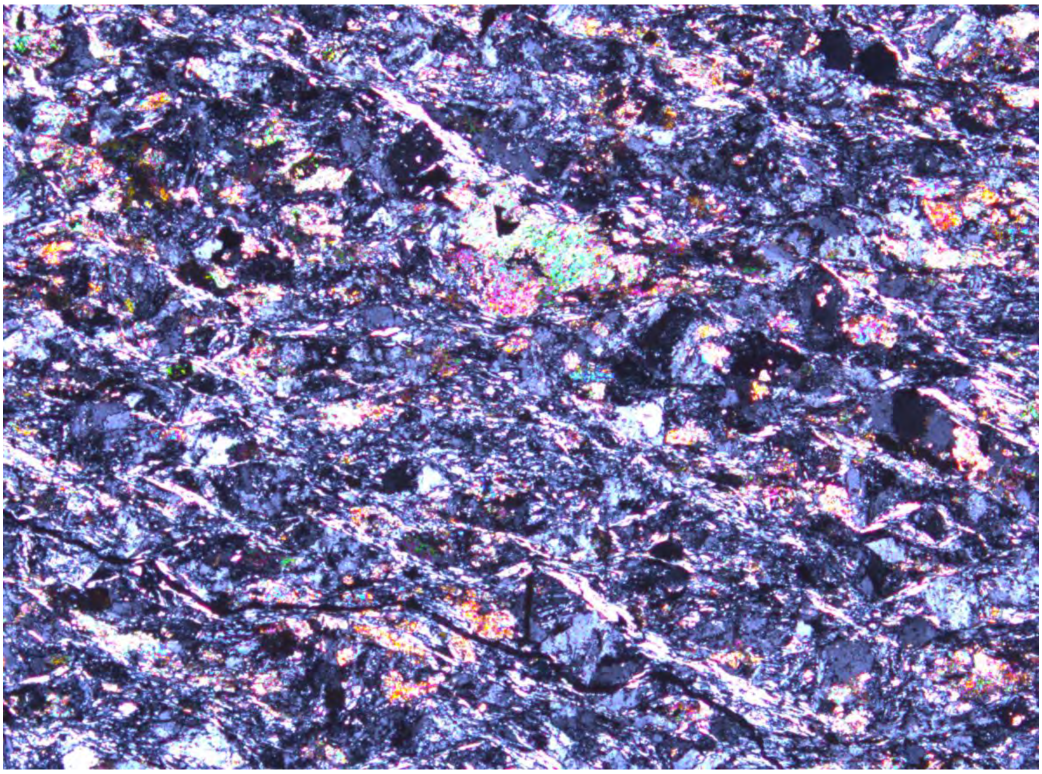
Figure 4: Thin section 1: Crossed-polarized light (XPL), 5× objective.

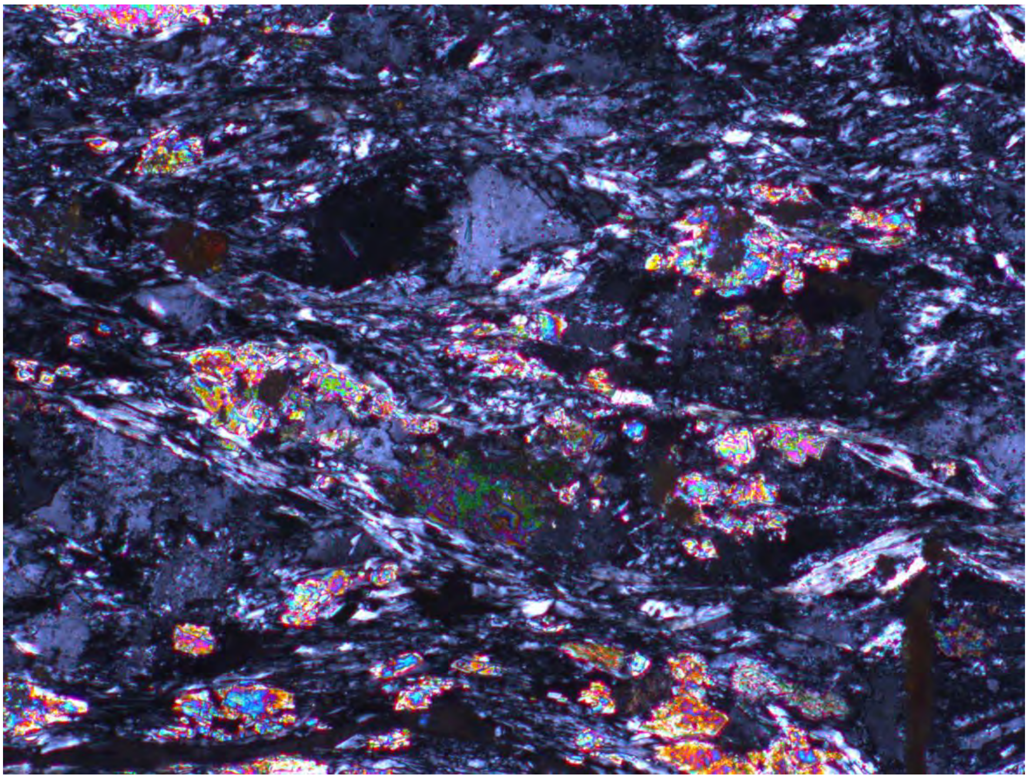
Figure 5: Thin section 1: Crossed-polarized light (XPL), 20× objective.

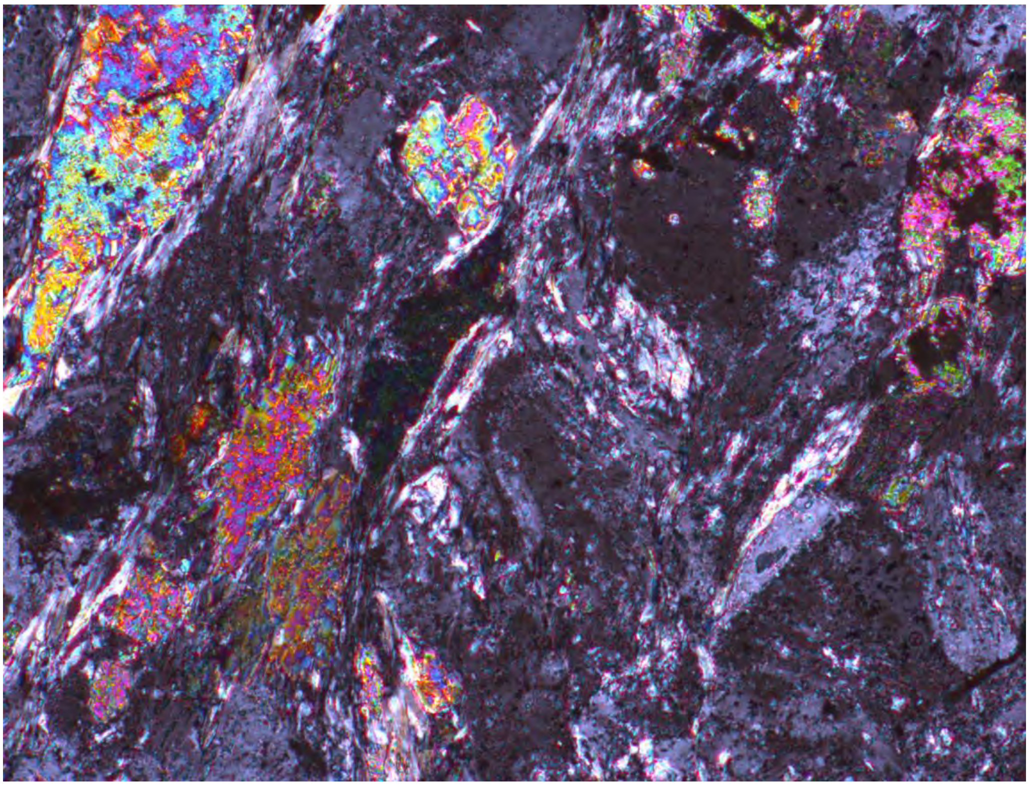
Figure 6: Thin section 1: Crossed-polarized light (XPL), 20× objective, turned.

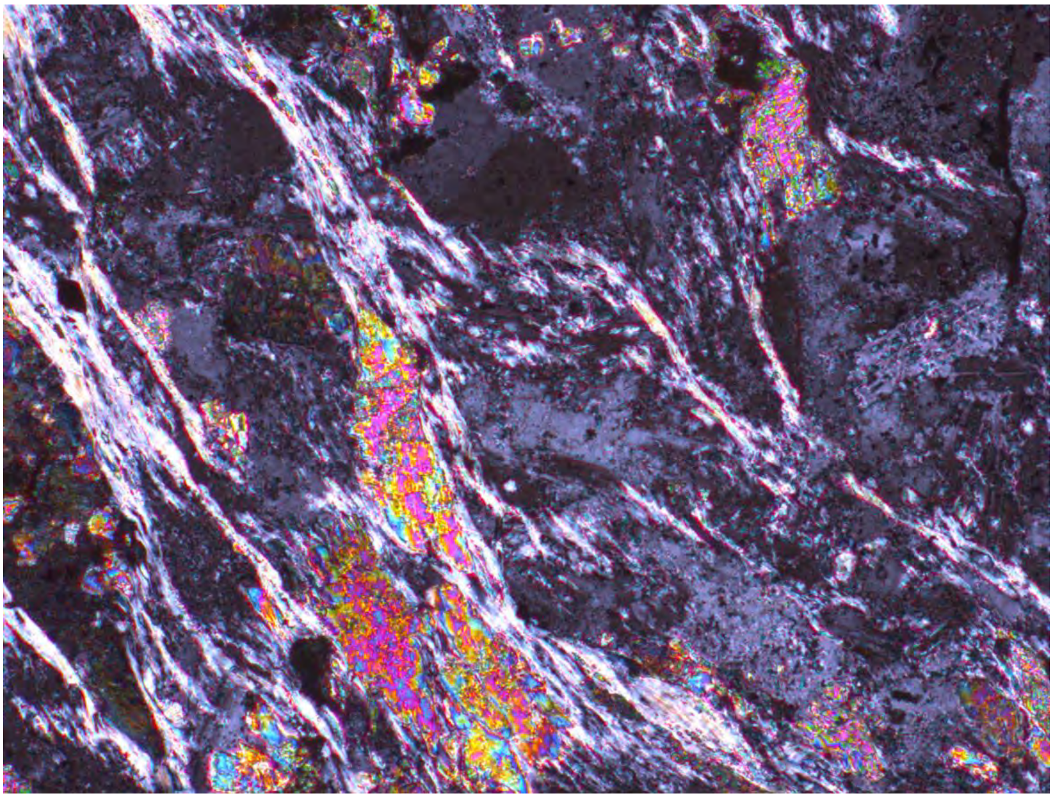

Figure7: Thin section 1: Crossed-polarized light (XPL), 20× objective.

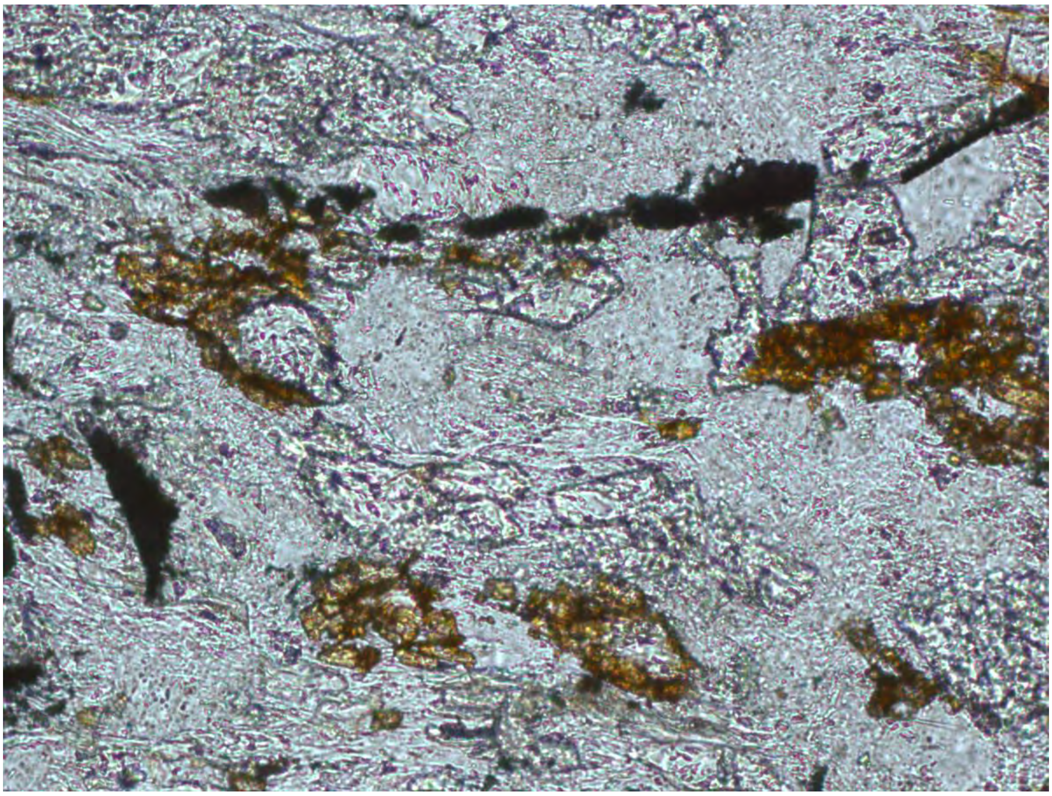

Figure 8: Thin section 1: Crossed-polarized light (XPL), 5× objective, Limonit.

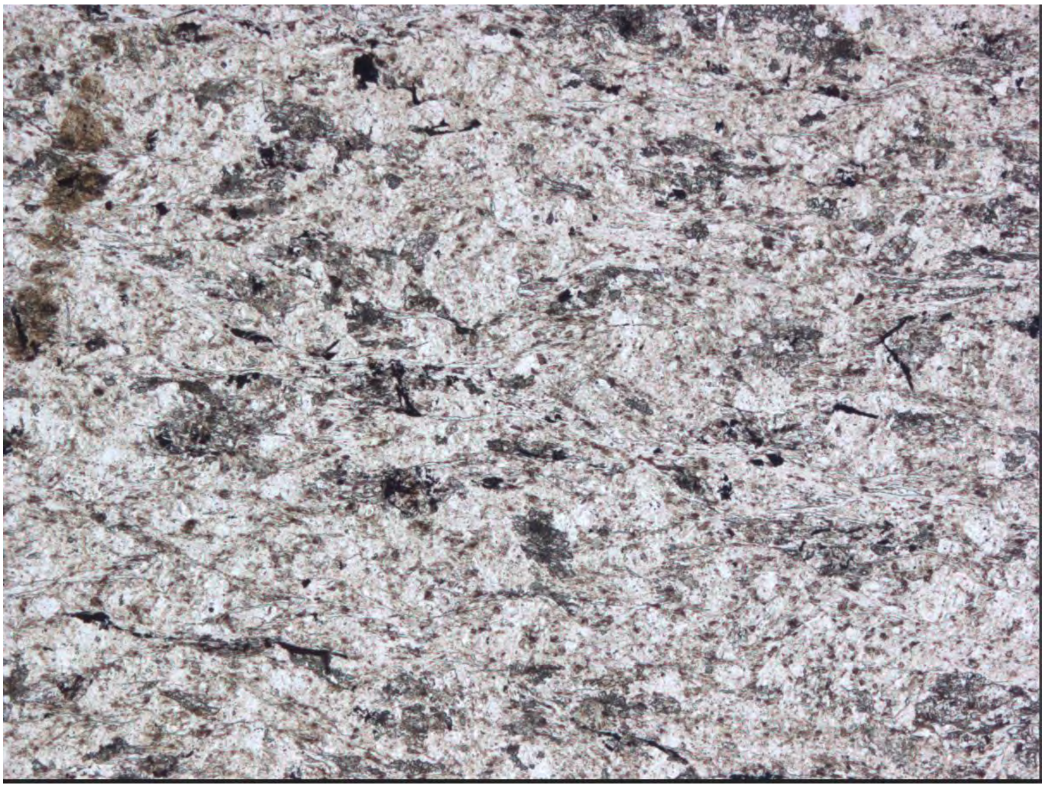

Figure 9: Thin section 1: Plane-polarized light (PPl), 5 x objective, younger S1 dextral through older S2.

Figure 10: Thin section 1: Plane-polarized light (XPl), 5 x objective, younger S1 dextral through older S2.

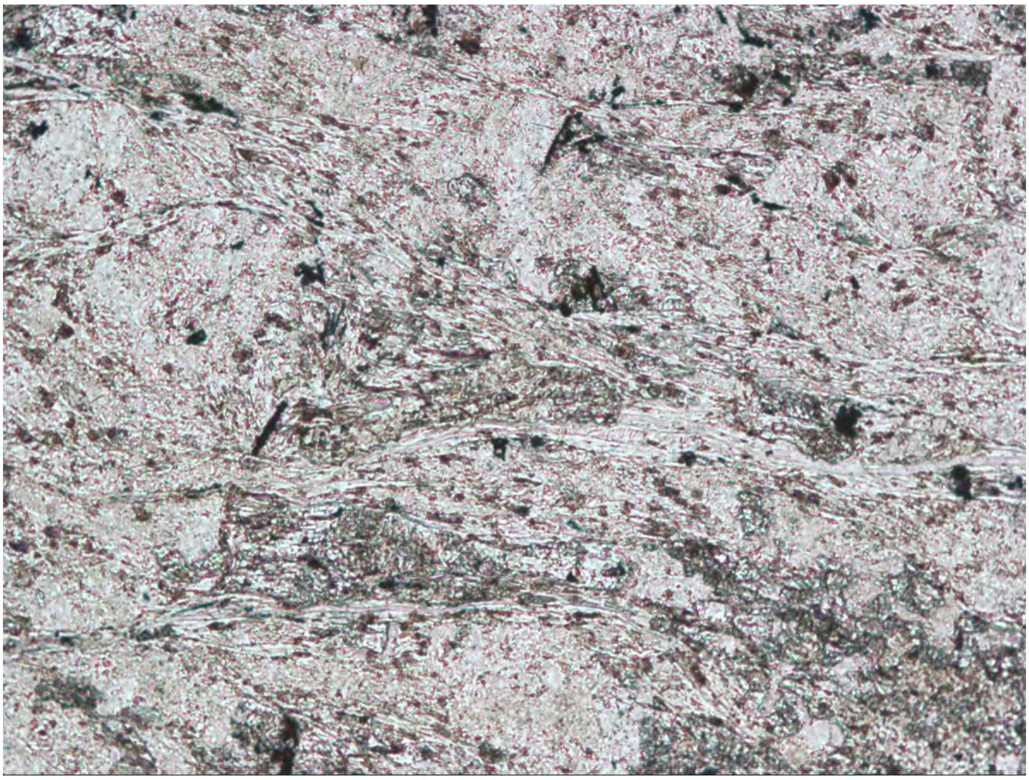

Figure 11: Thin section 1: Plane-polarized light (PPl), 10x objective, younger S1 dextral through older S2.

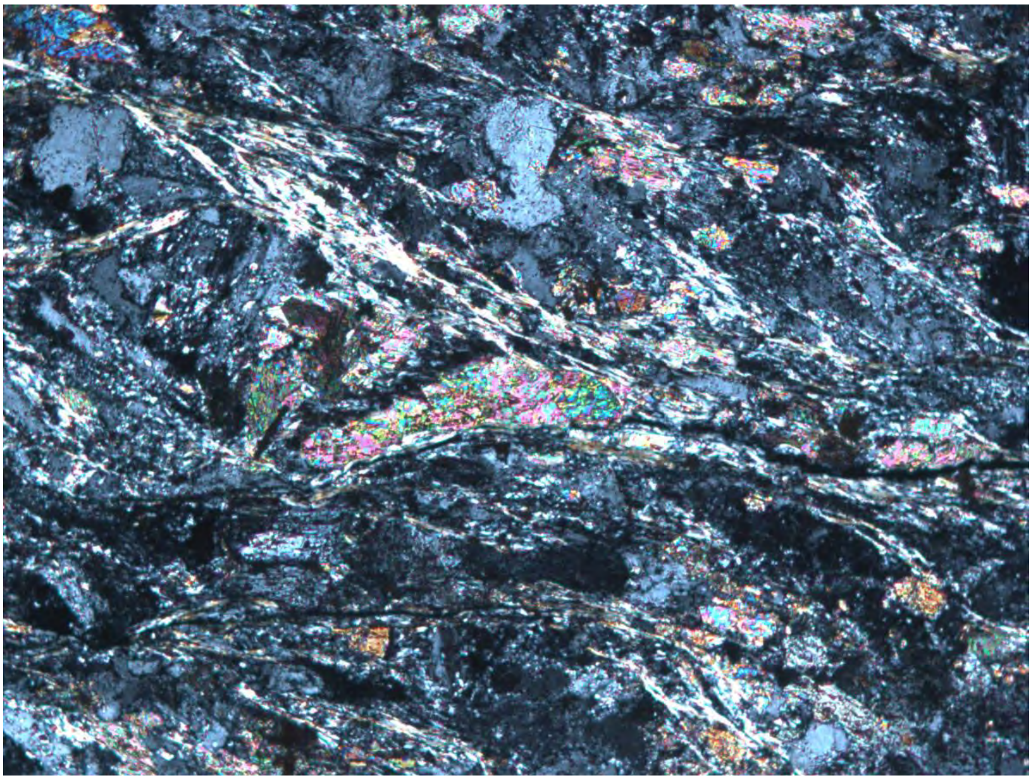

Figure 12: Thin section 1: Crossed-polarized light (XPl), 10x objective, younger S2 dextral through older S1.

1. Sample Overview

The thin section represents a fine-grained, foliated metamorphic rock of phyllitic composition. The section is unusually thin, resulting in enhanced interference colors and partial loss of optical characteristics (especially of chlorite). The rock contains a notable proportion of feldspar, suggesting a possible volcaniclastic contribution to the protolith.

2. Texture and Fabric

2.1 General texture

- Very fine-grained, lepidoblastic (mica-rich).
- Alignment of muscovite defines a well-developed foliation.

2.2 Foliation

- Two distinct foliations are visible.
- The dominant foliation (S2) is defined by muscovite flakes with grain sizes of 0.2–0.4 mm.
- The dominant foliation (S2) overprints the older S1 dextral.

2.3 Grain shape and morphology

- Quartz and feldspar are mostly anhedral; some feldspar grains show idiomorphic outlines, consistent with a volcanogenic source.
- Carbonates occur in irregular patches, partially recrystallized.

3. Mineral Constituents

3.1 Major minerals

- Quartz
  - Anhedral to subhedral grains, generally fine-grained.
  - Low-order interference colors.
  - Locally strained and undulose, consistent with deformation under greenschist-facies conditions.
- Feldspar (plagioclase ± K-feldspar)
  - Similar interference colors to quartz; identification based on polysynthetic twinning.
  - Occurs more frequently than typical for phyllites; may reflect volcanogenic or volcaniclastic material in the protolith.
  - Rarely exhibits sericitic alteration.
- Carbonates
  - Granular to patchy aggregates.
  - Interference colors unusually high due to the extreme thinness of the section.

3.2 Accessory minerals

- Rutile
  - Brownish pleochroic long-prismatic crystals.
  - Common accessory in metamorphosed Fe-Ti-bearing lithologies.
- Opaque minerals
  - Pyrite: metallic golden reflectance (visible in reflected light).
  - Ilmenite: completely opaque; altered portions appear brown (leucoxene rims).

    - Leucoxene / Titanite: alteration products of ilmenite; high relief and moderate interference colors.
- Mica (muscovite / sericite)
    - Bright, low-order interference colors.
    - Forms aligned flakes responsible for the foliation.

3.3 Secondary / weathering products

- Limonite
    - Brown, amorphous to cryptocrystalline infill in fractures.
    - Represents late-stage oxidation/alteration processes.

4. Metamorphic Conditions

Indicators such as:

- presence of fine-grained muscovite.
- absence (or non-detection due to thinness) of chlorite
- lepidoblastic fabric

suggest lower greenschist facies metamorphism.
Chlorite would be expected but is not identifiable, likely due to the exceedingly thin section which suppresses its characteristic interference colors.

5. Interpretation

5.1 Protolith

The elevated feldspar content and presence of idiomorphic grains indicate:
→ Possible volcaniclastic protolith, such as a tuffaceous sediment or fine-grained volcanogenic detritus.

5.2 Deformation

- Two foliations indicate at least two deformation events.
- Mica alignment suggests ductile deformation under low-grade metamorphic conditions.
- Shear sense ?

5.3 Alteration

- Oxidation along fractures (limonite) indicates post-deformational, near-surface weathering.

6. Petrographic Classification

Phyllite with volcaniclastic components (relatively large amount of feldspar (vulcanoclastic material), euhedral (vulcanogen components)). Thin section too thin to show chlorite.

2. Thin section 2 (dextral, Top W)

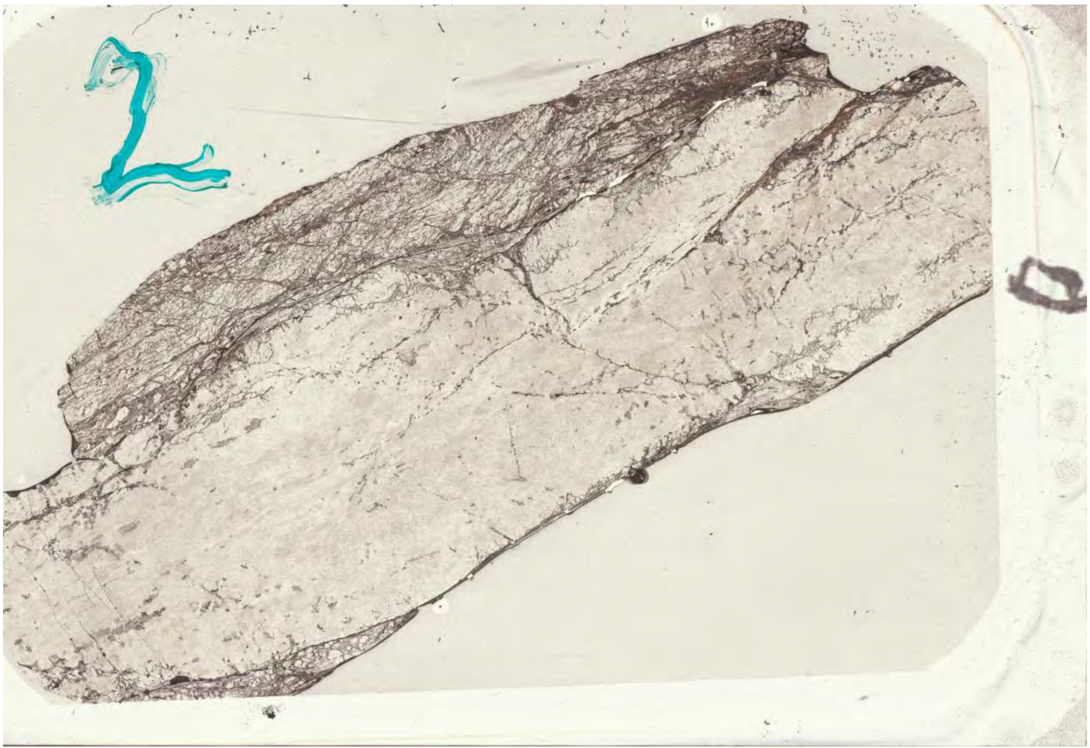

Figure 13: Thin section 2: scan. Top left E, top right W.

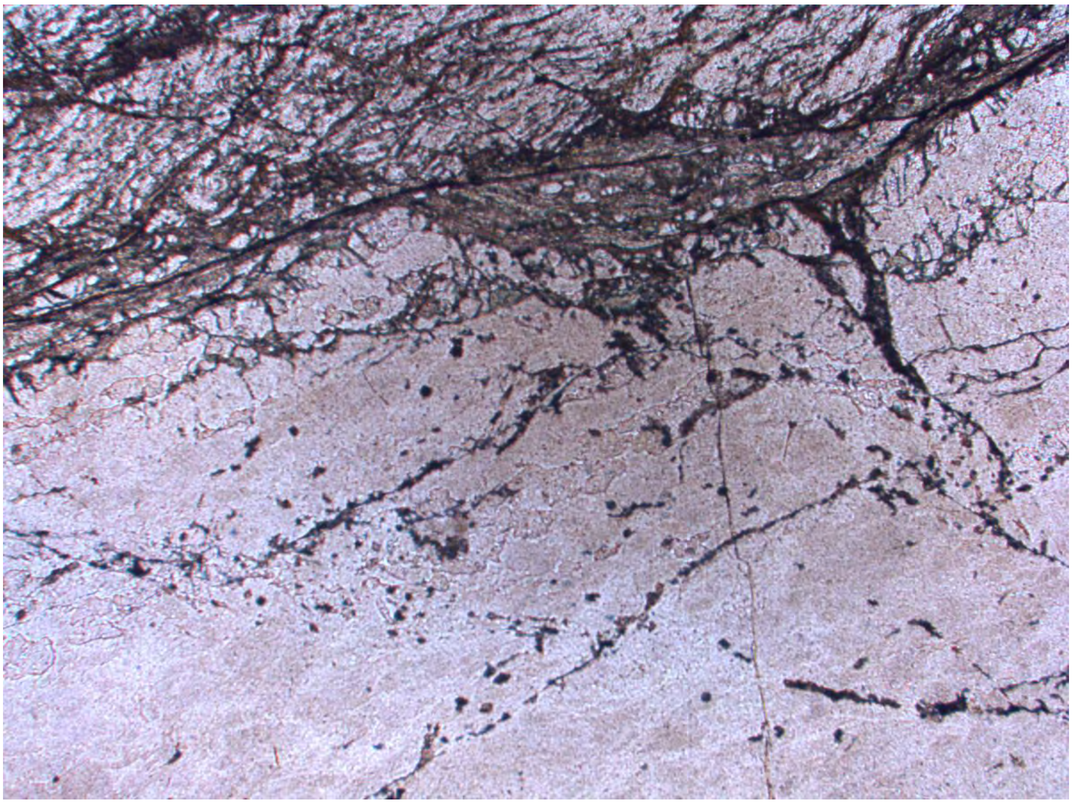

Figure 14: Thin section 2: Plane-polarized light (PPL), 1.25× objective.

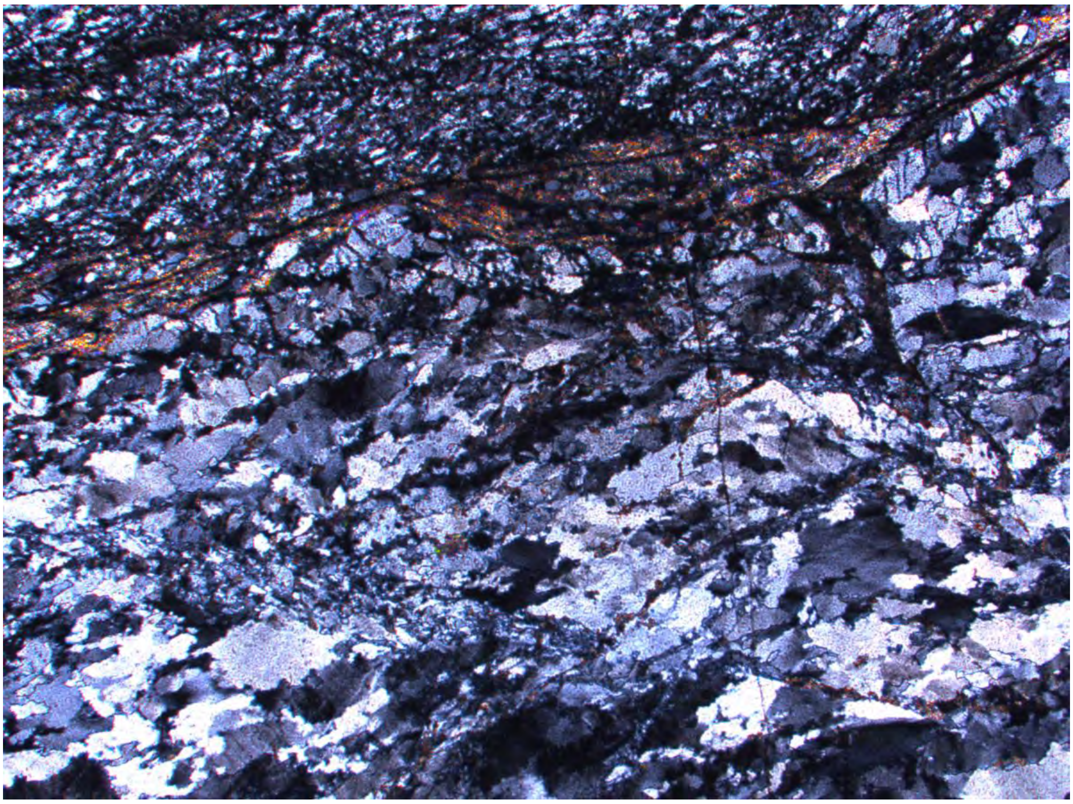
Figure 15: Thin section 2: Crossed-polarized light (XPL), 1.25× objective.

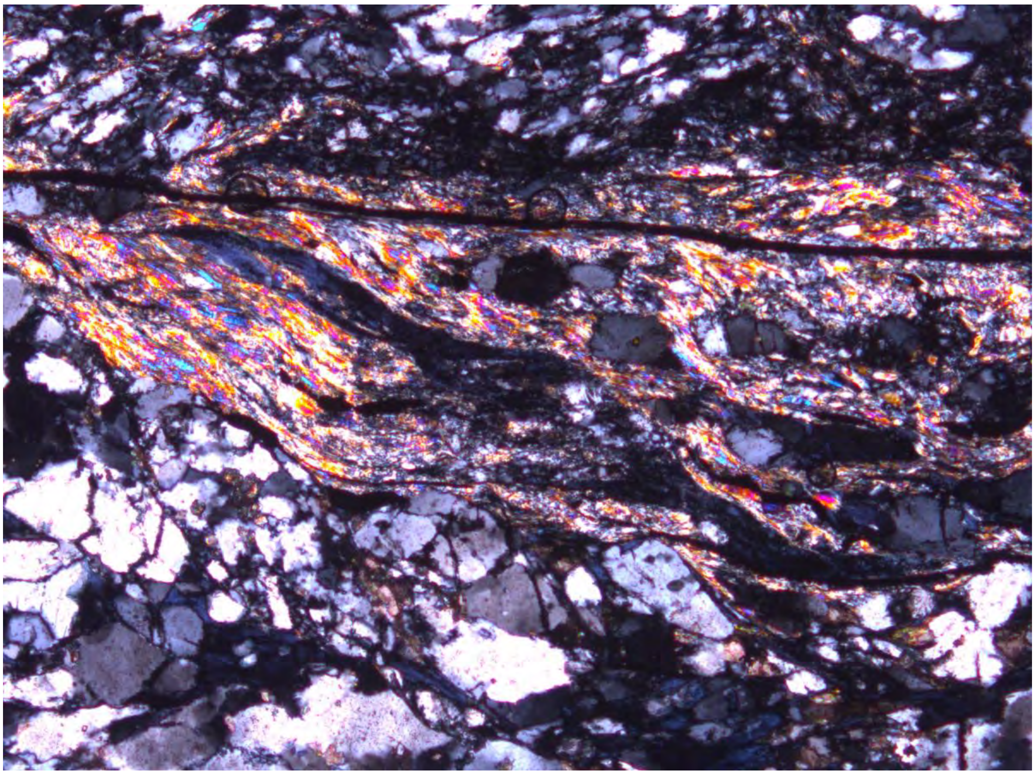
Figure 16: Thin section 2: Crossed-polarized light (XPL), 5× objective, white mica (colored), chlorite(blue).

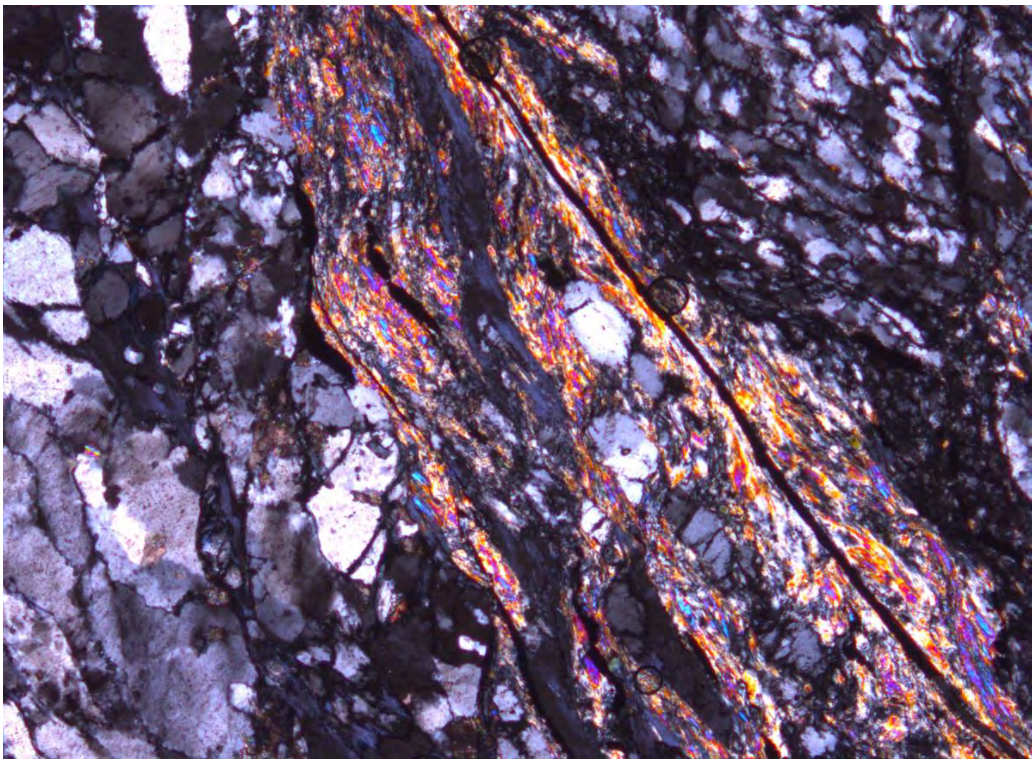

Figure 17: Thin section 2: Crossed-polarized light (XPL), 5× objective.

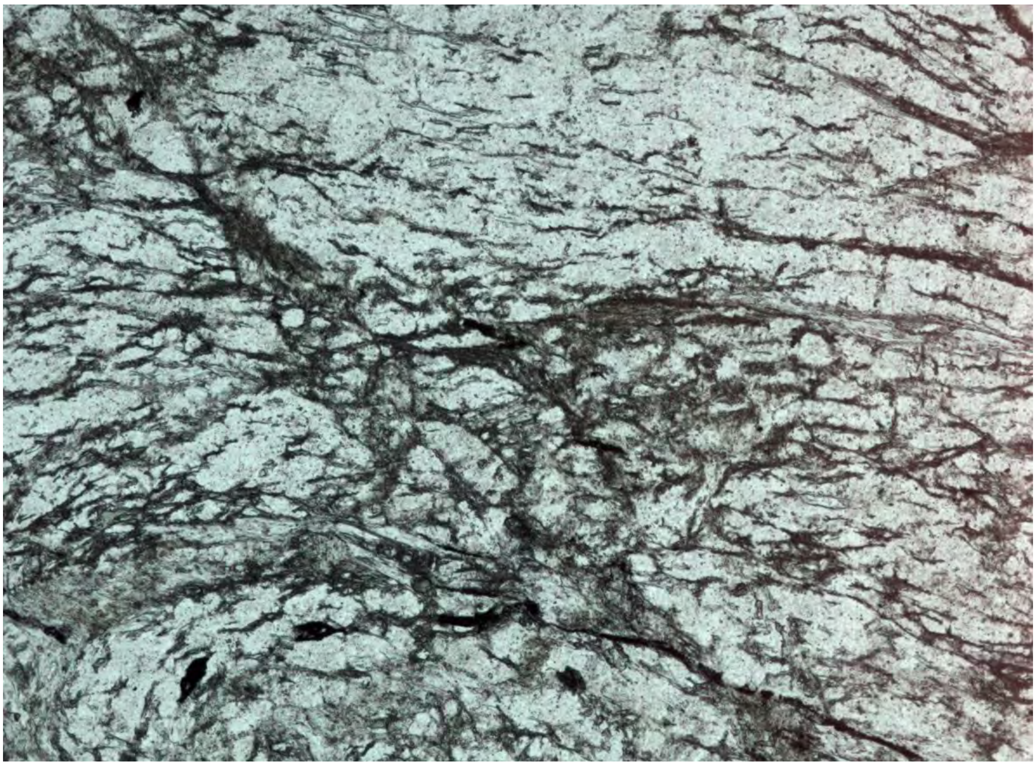

Figure 18: Thin section 2: Plane-polarized light (PPl), 5x objective, microfold(sinistral).

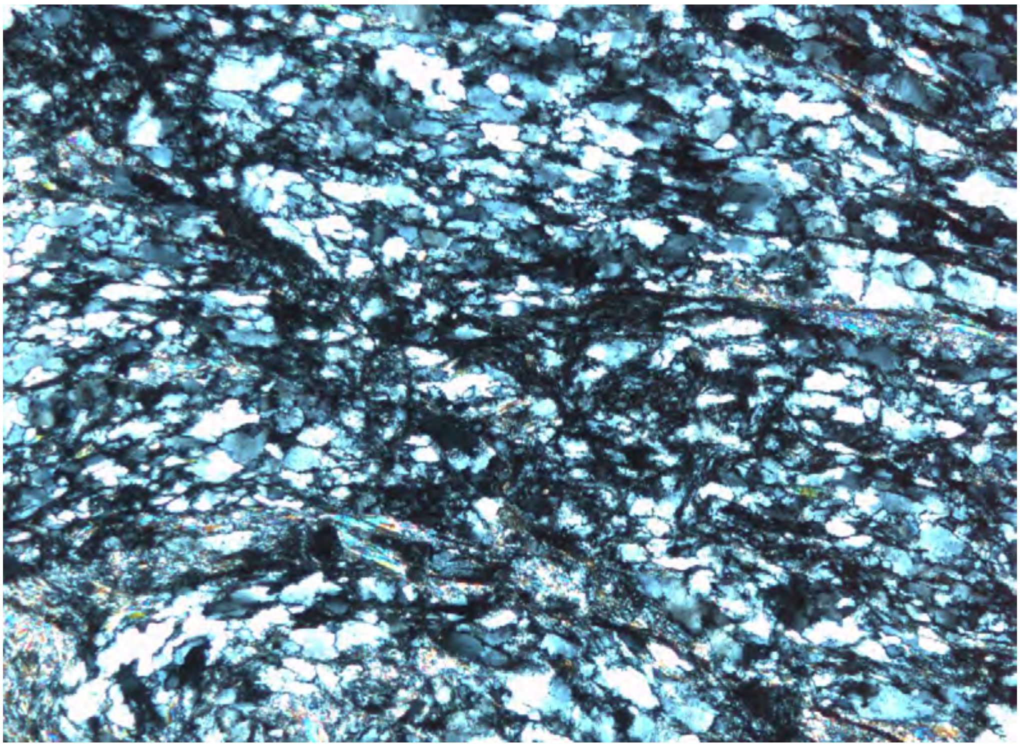

Figure 19: Thin section 2: Crossed-polarized light (PPl), 5x objective, microfold(sinistral).

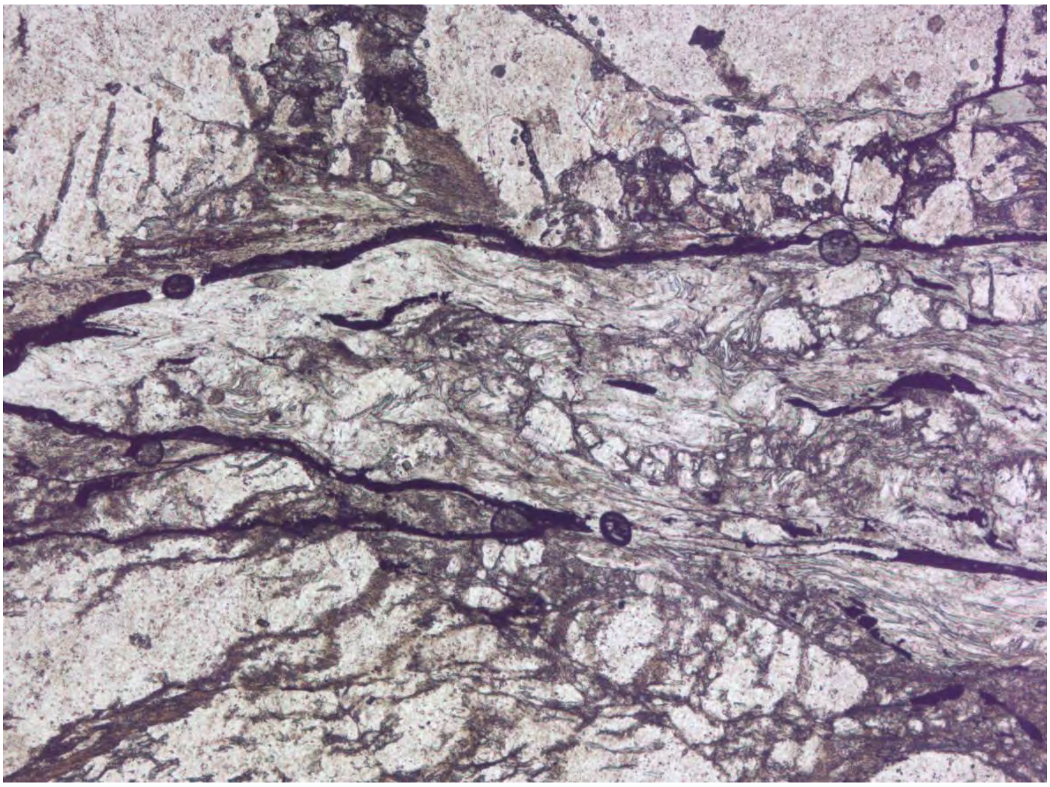

Figure 20: Thin section 2: Plane-polarized light (PPl), 5x objective, microfold(sinistral).

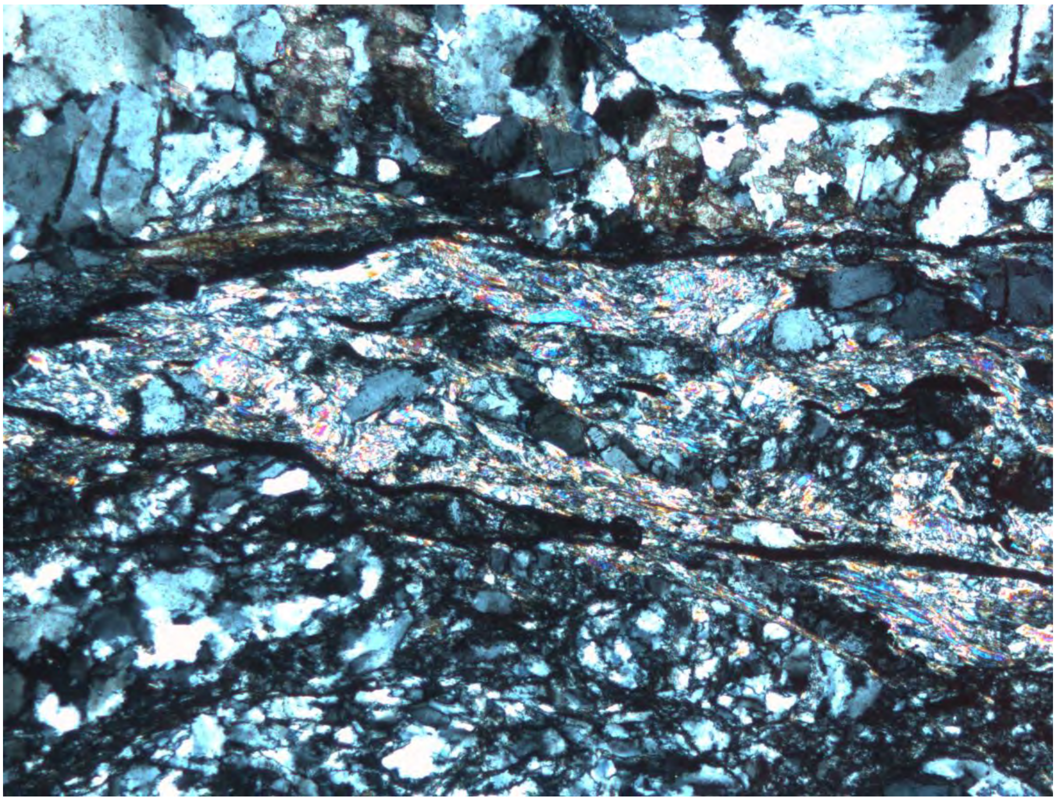

Figure 21: Thin section 2: Crossed-polarized light (XPl), 5x objective, microfold(sinistral).

1. Sample Overview

Thin section 2 represents a fine- to medium-grained metamorphic rock dominated by recrystallized quartz, white mica, and Fe-rich chlorite. Subordinate carbonate is present in discrete domains. The rock displays a well-developed foliation and contains microfolds that clearly indicate a sinistral (left-lateral) shear sense. The assemblage and microstructures are consistent with lower greenschist facies metamorphism.

2. Texture and Fabric

The dominant foliation is defined by aligned white mica, chlorite, and elongate recrystallized quartz.
The asymmetry of microfolds consistently indicates a sinistral shear sense.

3. Mineral Constituents

Major minerals

- **Quartz**
  - Abundant and strongly recrystallized.
  - Shows undulose extinction, subgrain development, and fine-grained neoblasts.
  - Occurs in elongate ribbons parallel to the main foliation.
- **White mica (muscovite)**
  - Colorless in PPL, moderate interference colors.
- **Chlorite (Fe-rich)**
  - Green in PPL, blue to turquoise interference colors in XPL.

- **Carbonate (minor)**
  - Present as small patches and lenses.

4. Metamorphic Conditions

The mineral assemblage quartz + muscovite + chlorite + carbonate (minor), no biotite indicates:

- Lower greenschist facies metamorphism.
- Likely temperature range 280–350 °C (supported by quartz recrystallization but absence of biotite) (eg. Marshak, 2019)

5. Interpretation

5.1 Protolith

The protolith was likely a **pelitic to semi-pelitic sediment** with minor carbonate content (e.g., calcareous shale or siltstone).

5.2 Metamorphic & structural evolution

- Chlorite stability and absence of biotite indicate the rock did not exceed lower greenschist conditions.
- Microfold asymmetry provides an indicator for left-lateral shear.

6. Petrographic Classification

Chlorite–muscovite schist with recrystallized quartz ribbons and sinistral microfolds.

3. Thin section 3 (sinistral, Top E)

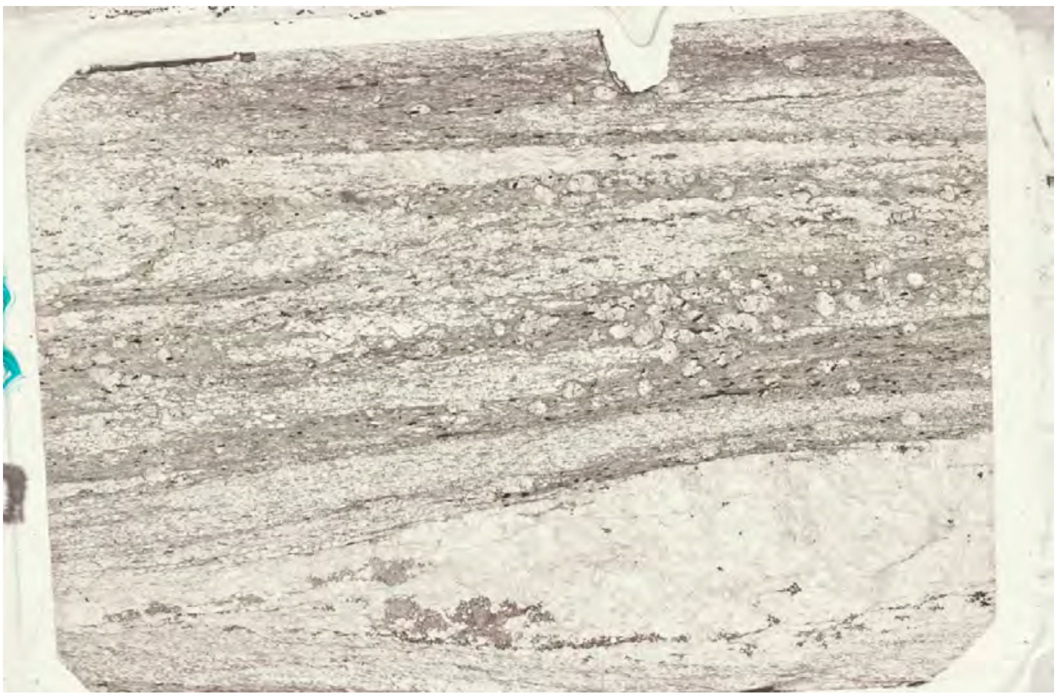

Figure 22: Thin section 3: scan. Top left E, top right W.

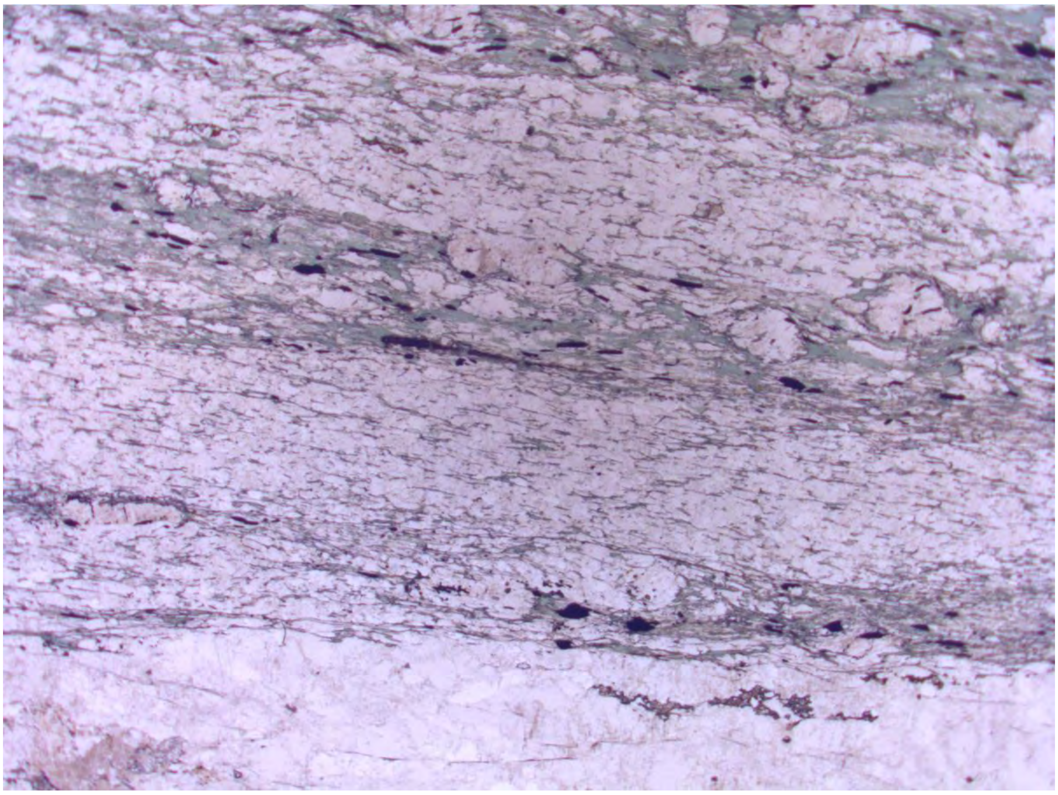

Figure 23: Thin section 3: Plane-polarized light (PPL), 1.25× objective.

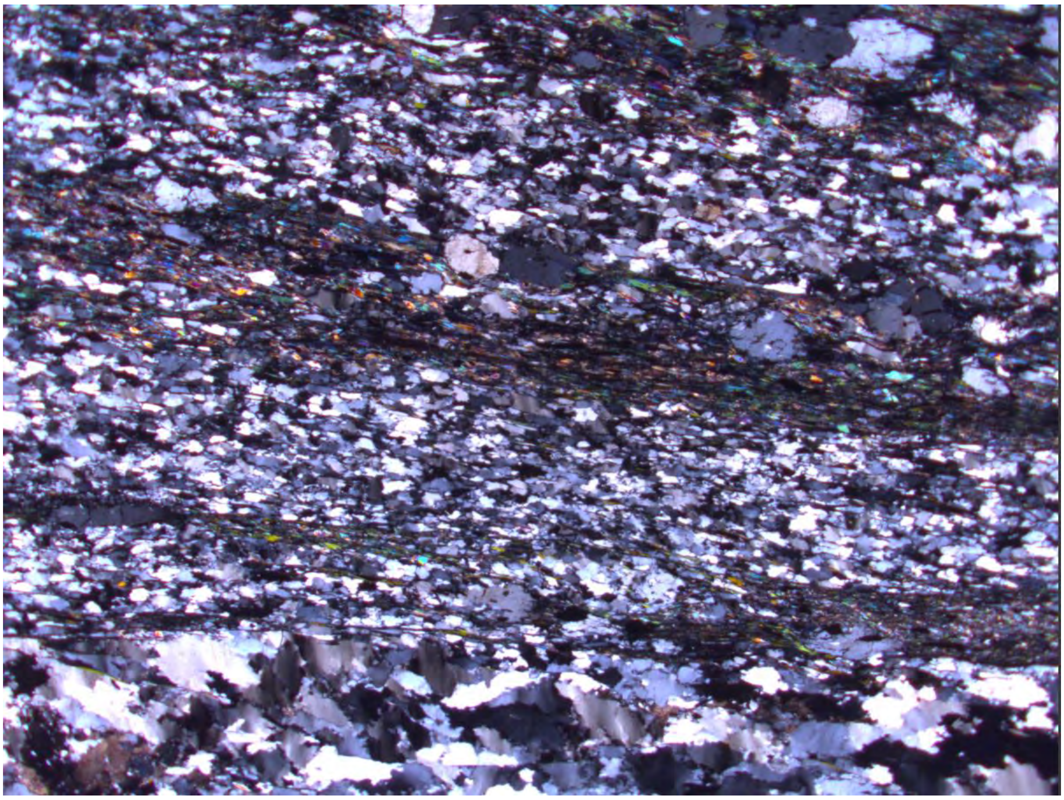

Figure 24: Thin section 3: Crossed-polarized light (XPL), 1.25× objective.

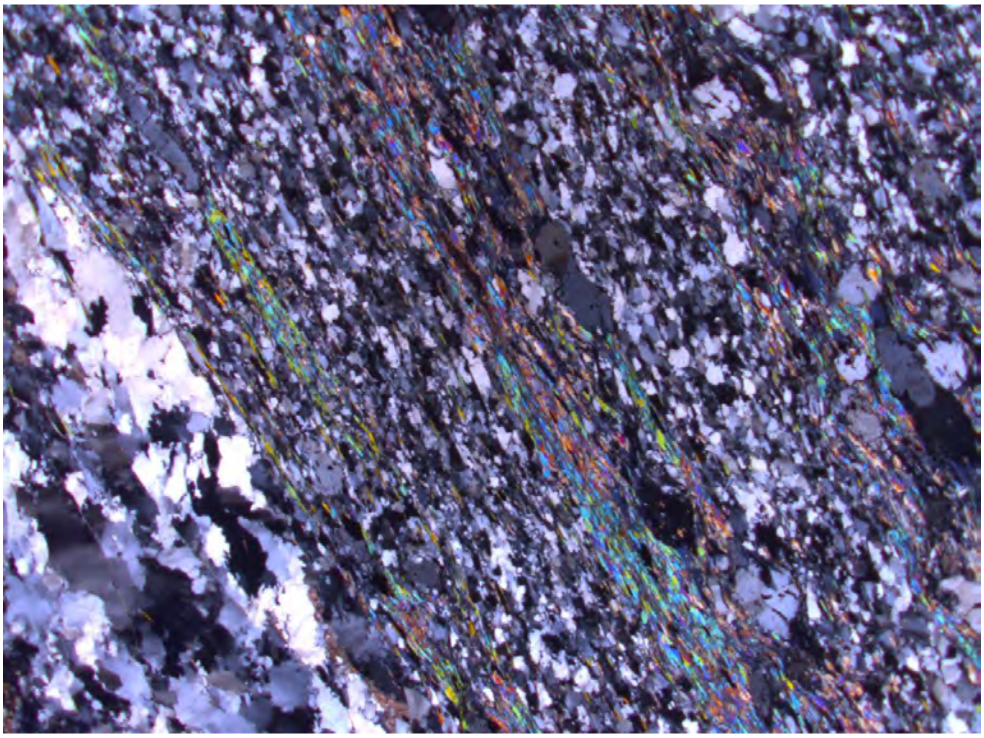

Figure 25: Thin section 3: Crossed-polarized light (XPL), 1.25× objective, turned.

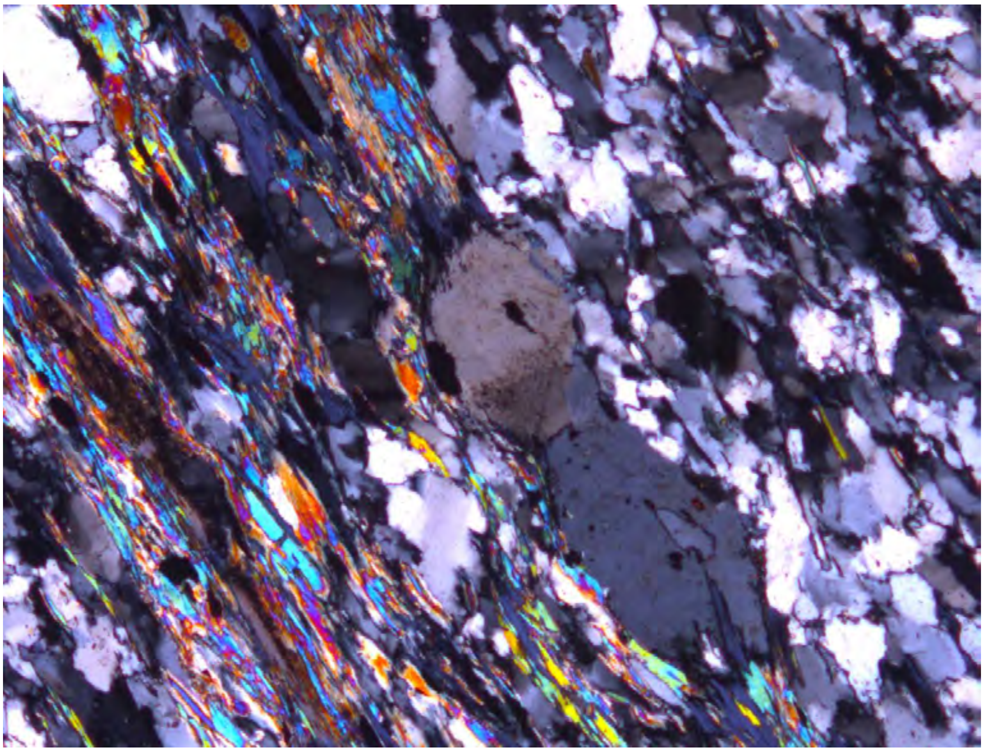

Figure 26: Thin section 3: Crossed-polarized light (XPL), 5× objective, turned.

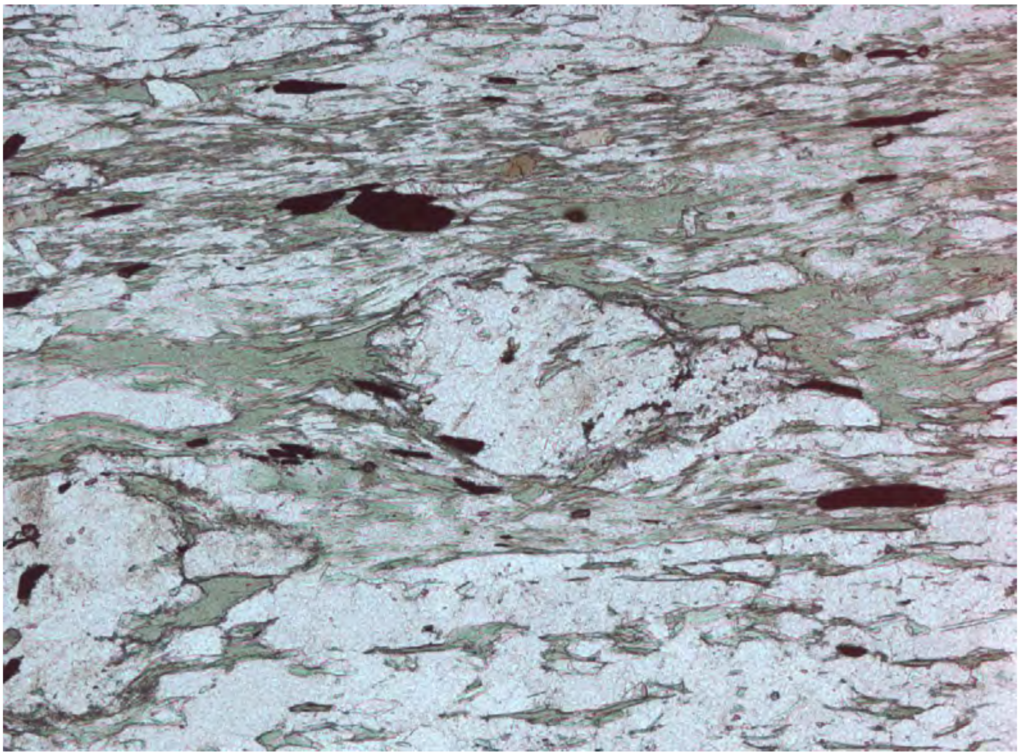

Figure 27: Thin section 3: Plane-polarized light (PPL), 5× objective, Albit.

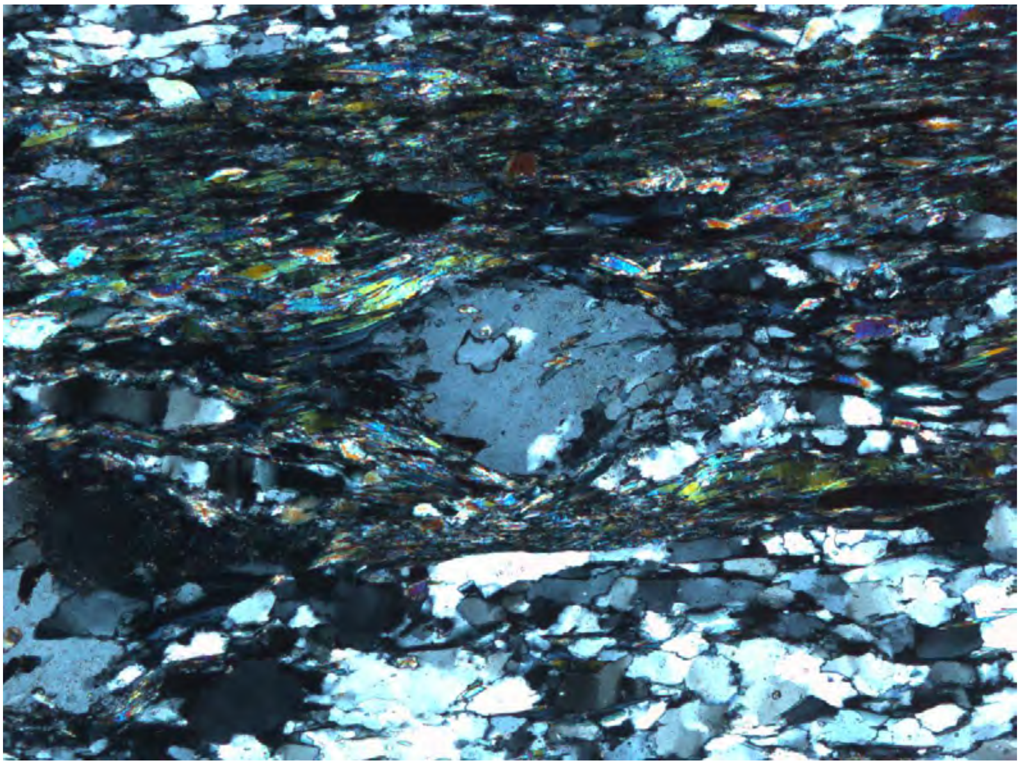

Figure 28: Thin section 3: Crossed-polarized light (XPL), 5× objective.

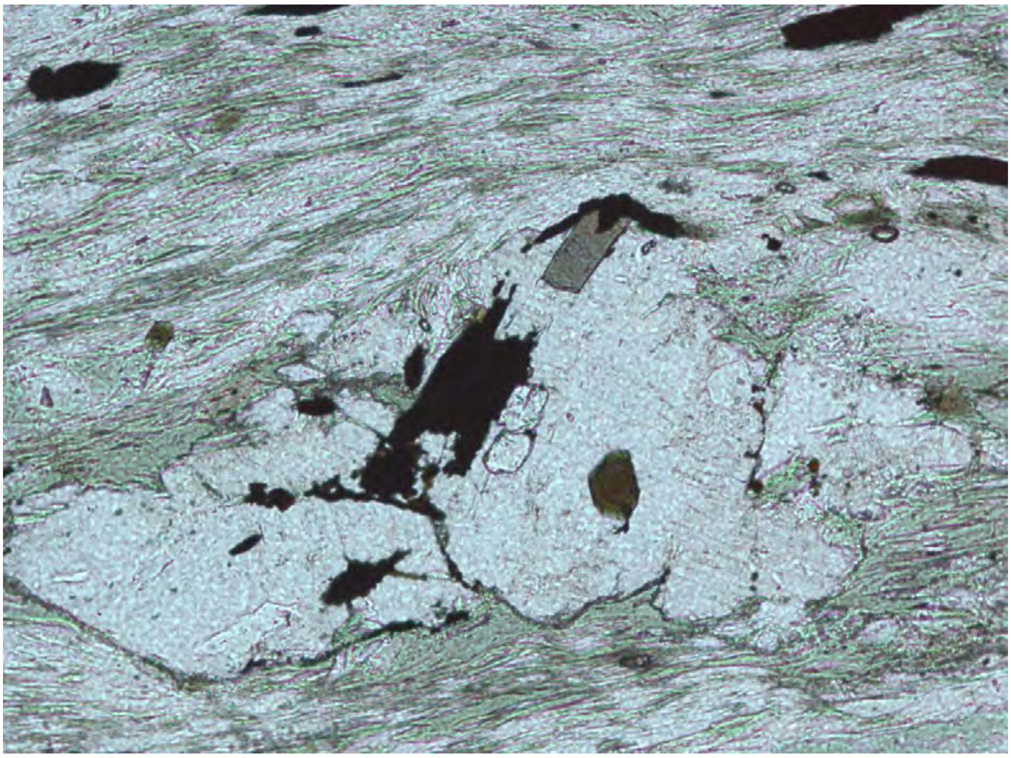

Figure 29: Thin section 3: Plane-polarized light (PPL), 10× objective, Apatit, Turmalin, Ilmenit (opaque)..

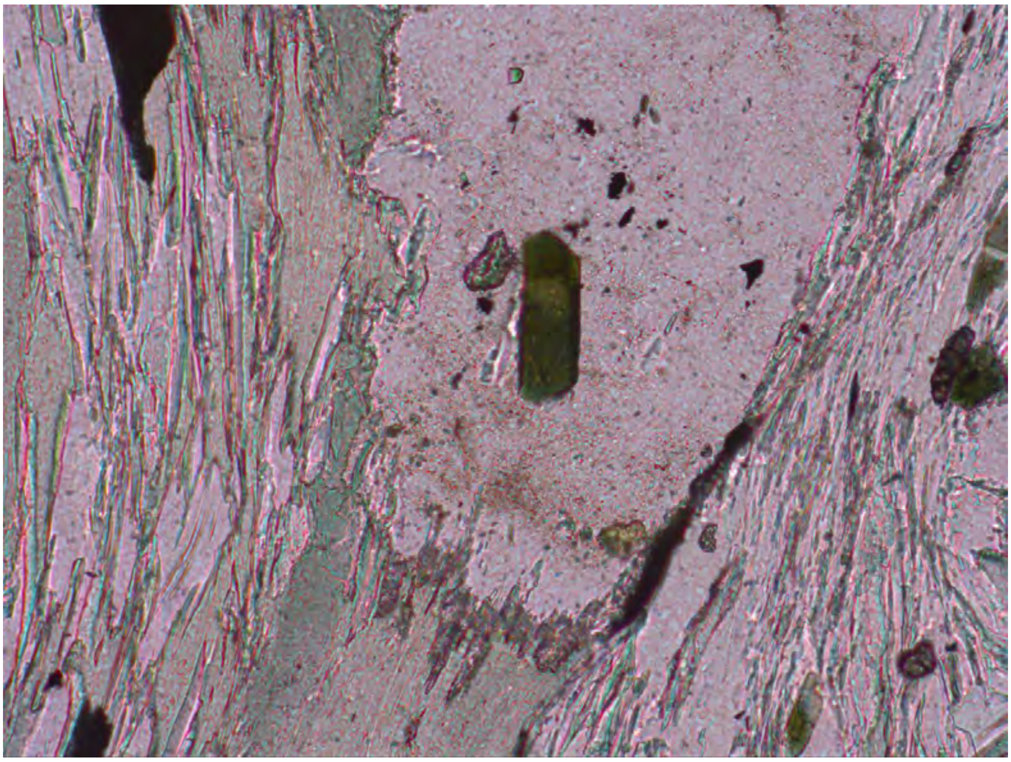

Figure 30: Thin section 3: Plane-polarized light (PPL), 20× objective, Turmalin (NS direction).

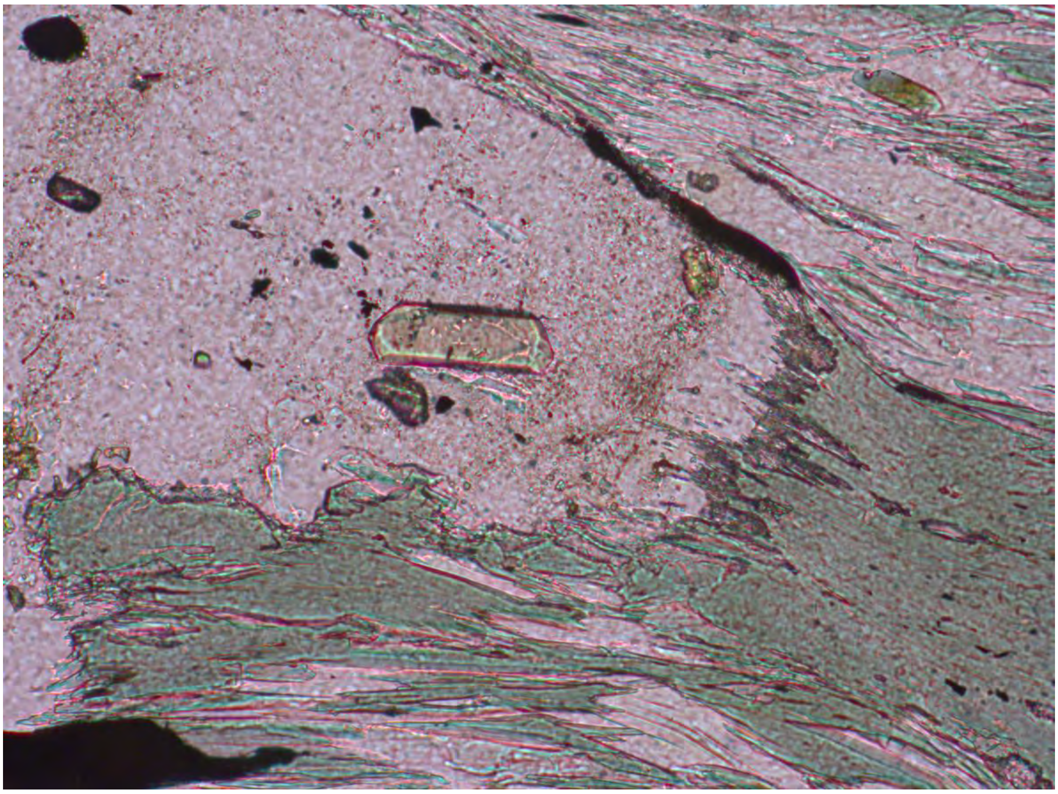

Figure 31: Thin section 3: Plane-polarized light (PPL), 20× objective, Turmalin (WO direction).

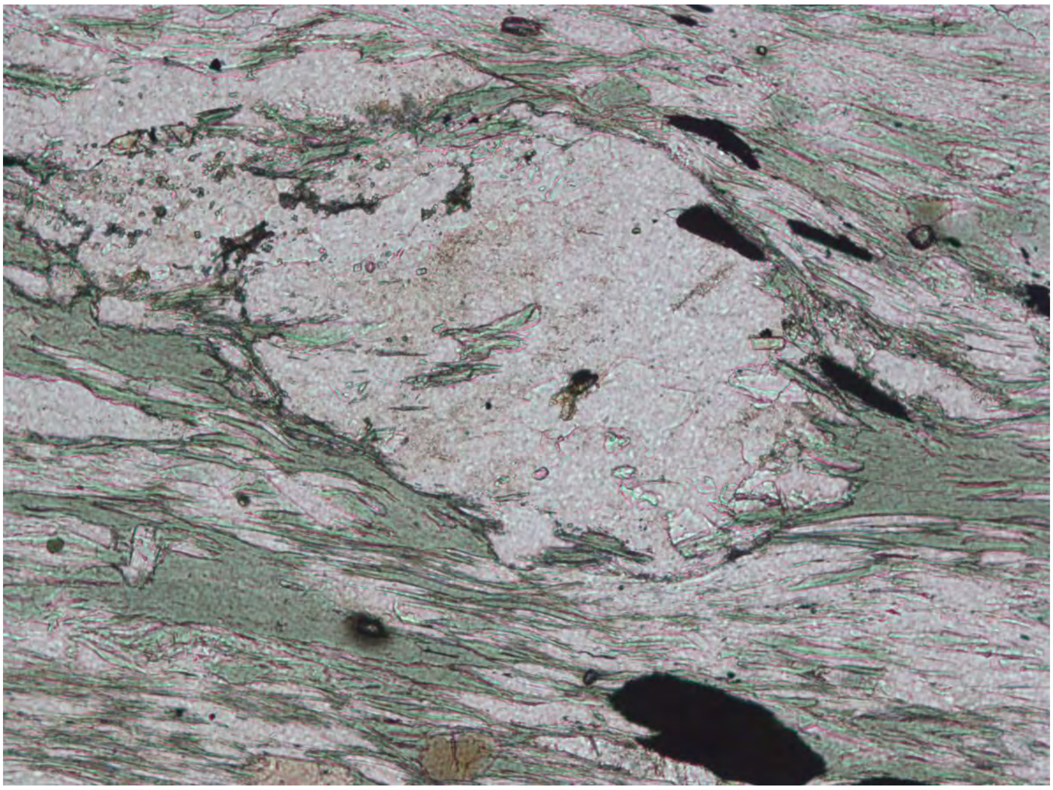

Figure 32: Thin section 3: Plane-polarized light (PPL), 10× objective, clast (sinistral).

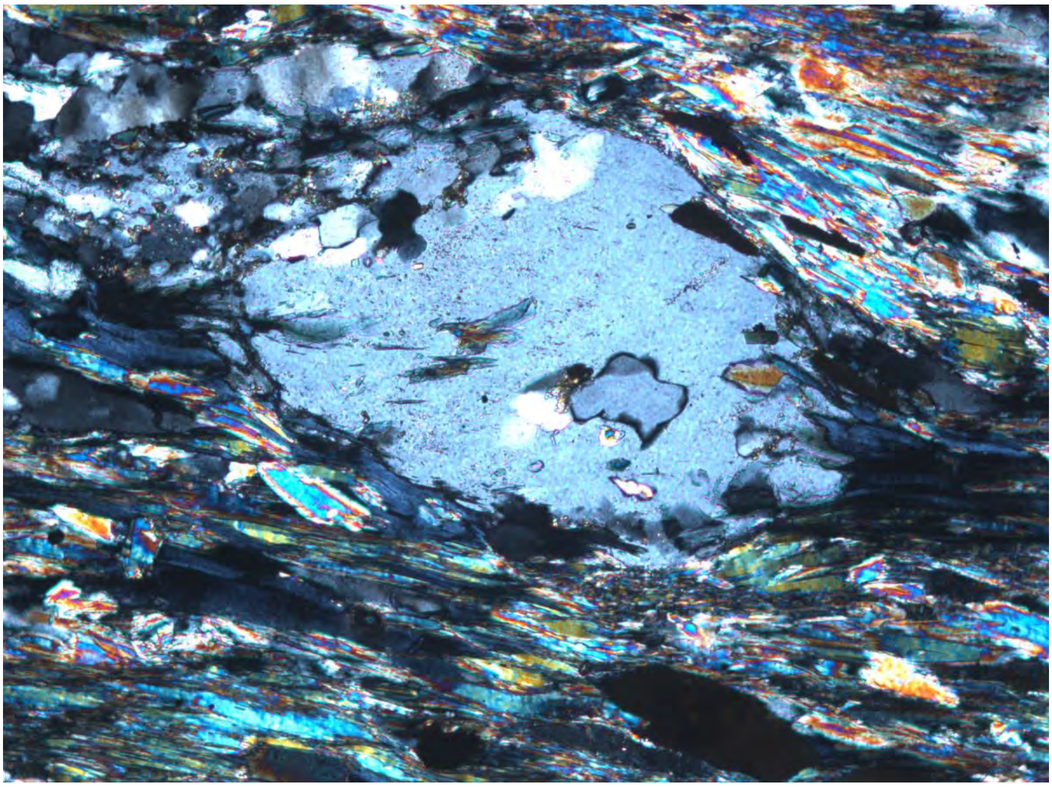

Figure 33: Thin section 3: Crossed-polarized light (XPL), 10× objective, clast (sinistral).

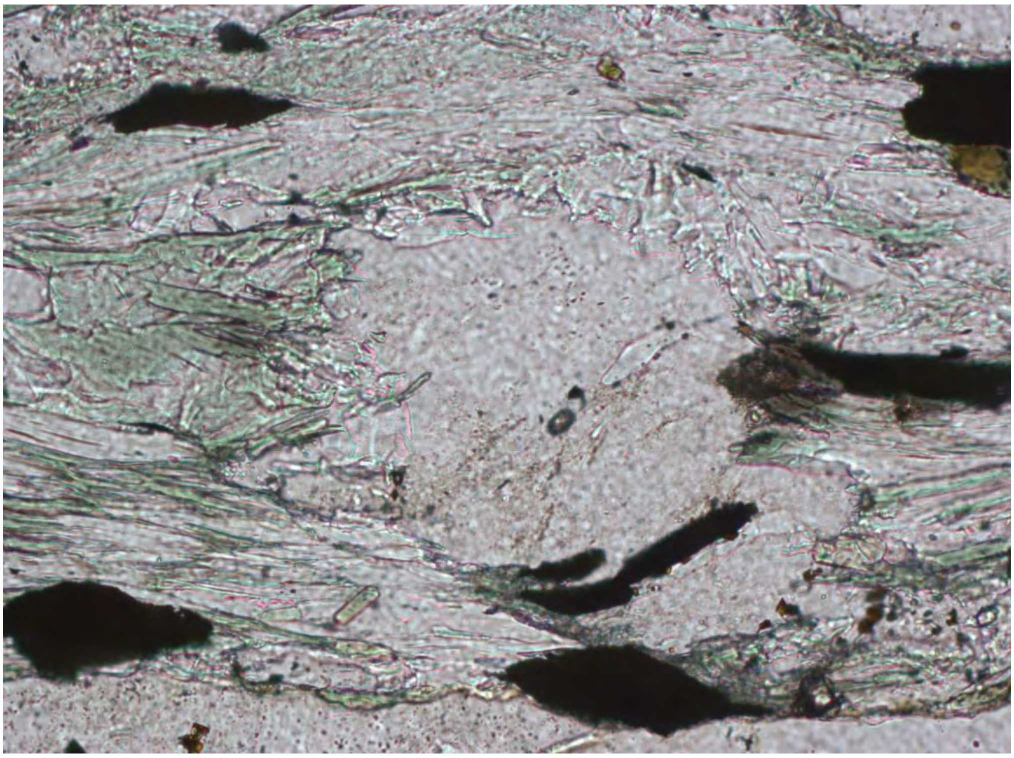

Figure 34: Thin section 3: Plane-polarized light (PPL), 20× objective, clast (sinistral).

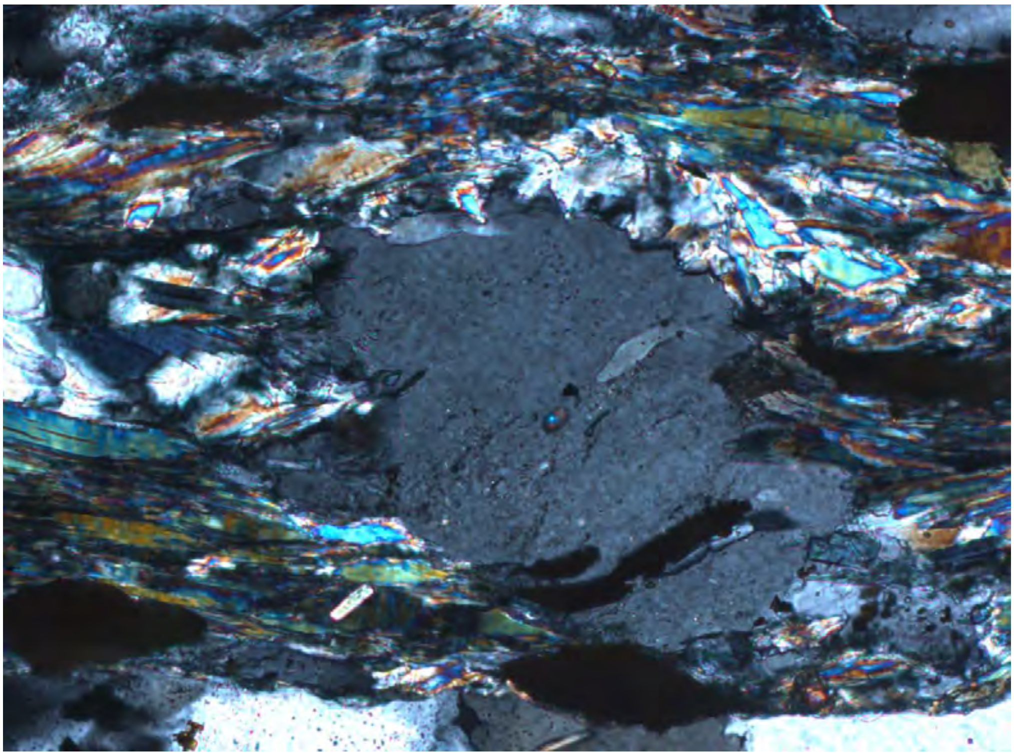

Figure 35: Thin section 3: Crossed-polarized light (XPL), 20× objective, clast (sinistral).

1. Sample Overview

The thin section represents a fine- to medium-grained metamorphic rock characterized by compositional banding and foliation. The mineralogy is dominated by quartz, carbonate, and sheet silicates (chlorite and white mica), with significant feldspar (albite). Accessory minerals include tourmaline, ilmenite, zircon, pyrite, and apatite. The rock shows pronounced mineral alignment parallel to the compositional layering, indicating deformation under greenschist-facies conditions.

2. Texture and Fabric

2.1 Compositional layering

The rock exhibits a distinct compositional banding consisting of:

1. **Quartz-rich, feldspar-bearing domains**, locally enriched in carbonates
2. **Sheet-silicate layers** (chlorite + white mica), representing former S-surfaces
3. **Heterogeneous stripes** containing large, aligned albite clasts

2.2 Foliation and lineation

- Foliation is defined by the alignment of chlorite, white mica, and elongate quartz.
- All mineral phases, including albite, show preferred orientation parallel to the linear fabric.
- Quartz is recrystallized into elongate ribbons consistent with deformation.

2.2 Grain shape relationships

- Albite porphyroclasts exhibit internal alignment and external stretching.
- Quartz shows dynamic recrystallization (mosaic textures / subgrain development).
- Zircon inclusions disrupt chlorite layers.

3. Mineral Constituents

3.1 Major minerals

- **Quartz**
  - Forms the bulk of the rock.
  - Strongly recrystallized; anhedral mosaic textures dominate.
  - Elongated quartz grains aligned parallel to the foliation and lineation.
- **Carbonates**
  - Occur in discrete carbonate-enriched bands.
  - Fine- to medium-grained, commonly intergrown with quartz.
- **Chlorite (Fe-rich)**
  - Blue interference colors (Fe-rich composition).
  - Represents the main component of the sheet-silicate layers (S-layers).
  - Often disrupted by zircon inclusions (fractured chlorite envelopes).
- **White mica (muscovite/sericite)**
  - Light interference colors.
  - Well aligned and concentrated in phyllosilicate-rich bands.
- **Albite (plagioclase)**
  - Present both as fine grains and as larger porphyroclasts.
  - Often aligned within foliation; exhibits polysynthetic twinning.
  - Occurs in feldspar-enriched domains.

3.2 Accessory minerals

- **Tourmaline** – prismatic, pleochroic; scattered throughout matrix.
- **Ilmenite** – opaque; locally altered to leucoxene.
- **Zircon** – small, high-relief grains; commonly disrupt chlorite layers (“fracturing/chasing” effect).
- **Pyrite** – rare, present as subhedral opaque grains.
- **Apatite** – small, rounded grains (“spherical nodules”).

3.3 Secondary phases

- **Limonite** – brown alteration/oxidation product; infills microfractures.

4. Metamorphic Conditions

Indicators such as:

- chlorite + white mica assemblage
- recrystallized quartz ribbons

- absence of higher-grade index minerals (e.g., garnet, biotite)

are consistent with greenschist-facies metamorphism, likely at relatively low to intermediate temperatures.

5. Interpretation

5.1 Protolith

The rock may derive from a **mixed carbonate–siliciclastic sediment**, with contributions from **volcaniclastic material** (supported by the abundance of albite and presence of tourmaline, zircon).

5.2 Deformation

- Multiple domains of recrystallized quartz, aligned micas, and aligned albite clasts suggest ductile deformation.

5.2 Alteration

- Limonite represents late-stage oxidative alteration.
- Zircon-induced “dissolution” of chlorite.

6. Petrographic Classification

Carbonate–quartz–chlorite schist with albite and muscovite, exhibiting compositional banding and lineation.

4. Thin section 4 (unclear)

Figure 36: Thin section 4: scan. Top left E, top right W.

Figure 37: Thin section 4: Plane-polarized light (PPL), 1.25× objective.

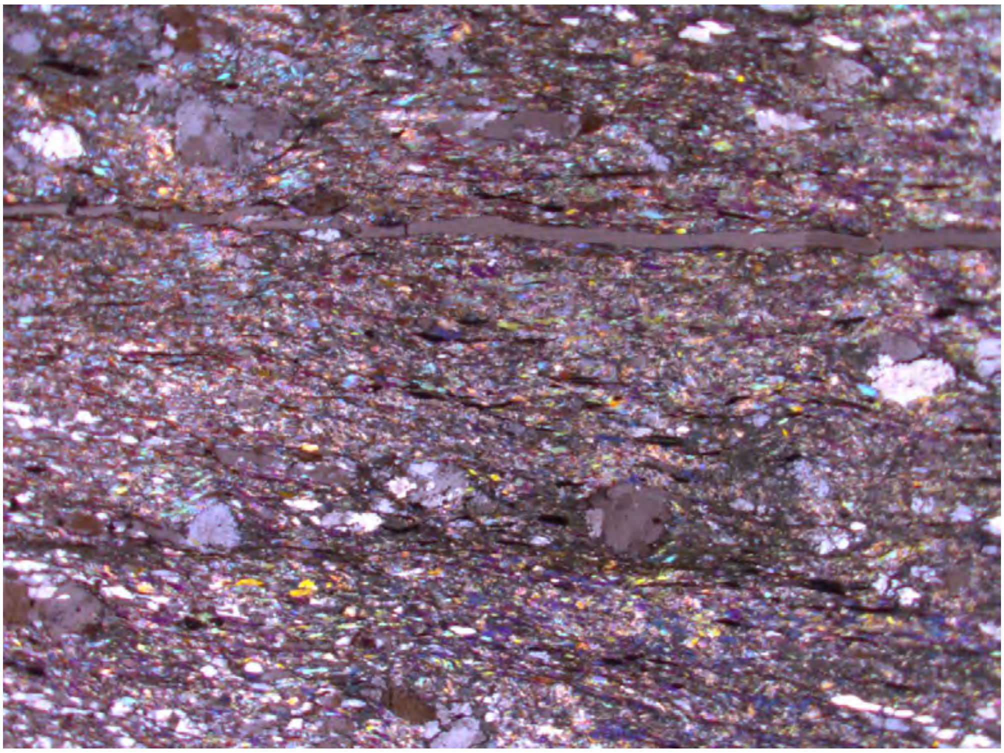

Figure 38: Thin section 4: Crossed-polarized light (XPL), 1.25× objective.

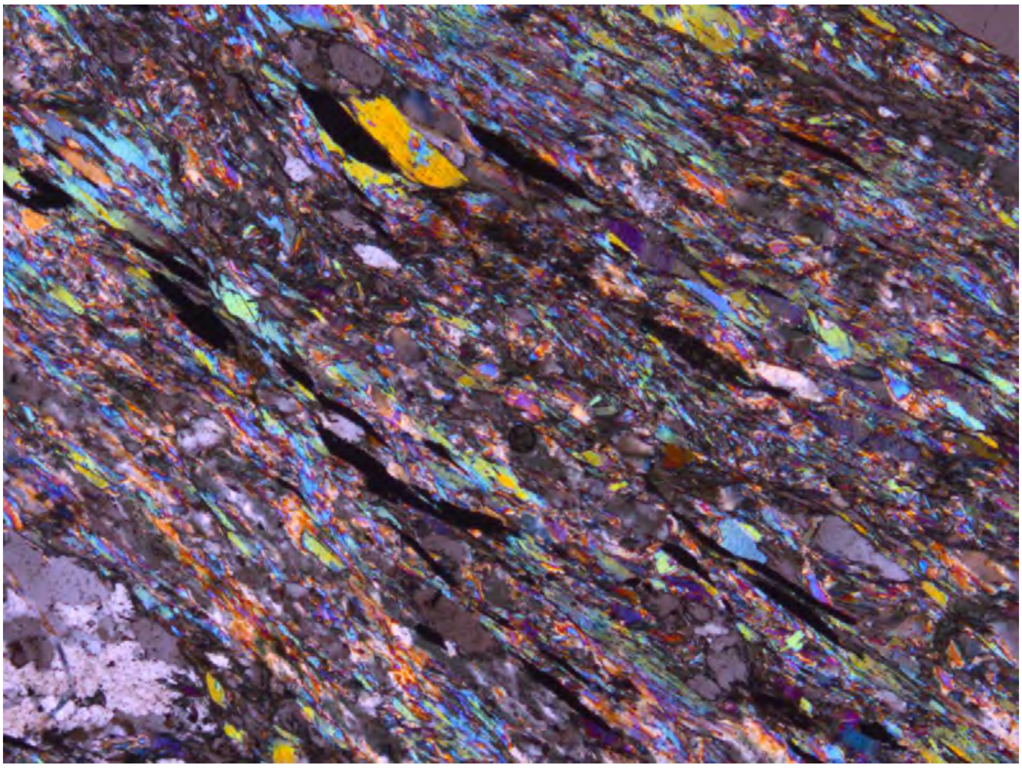

Figure 39: Thin section 4: Crossed-polarized light (XPL), 5× objective.

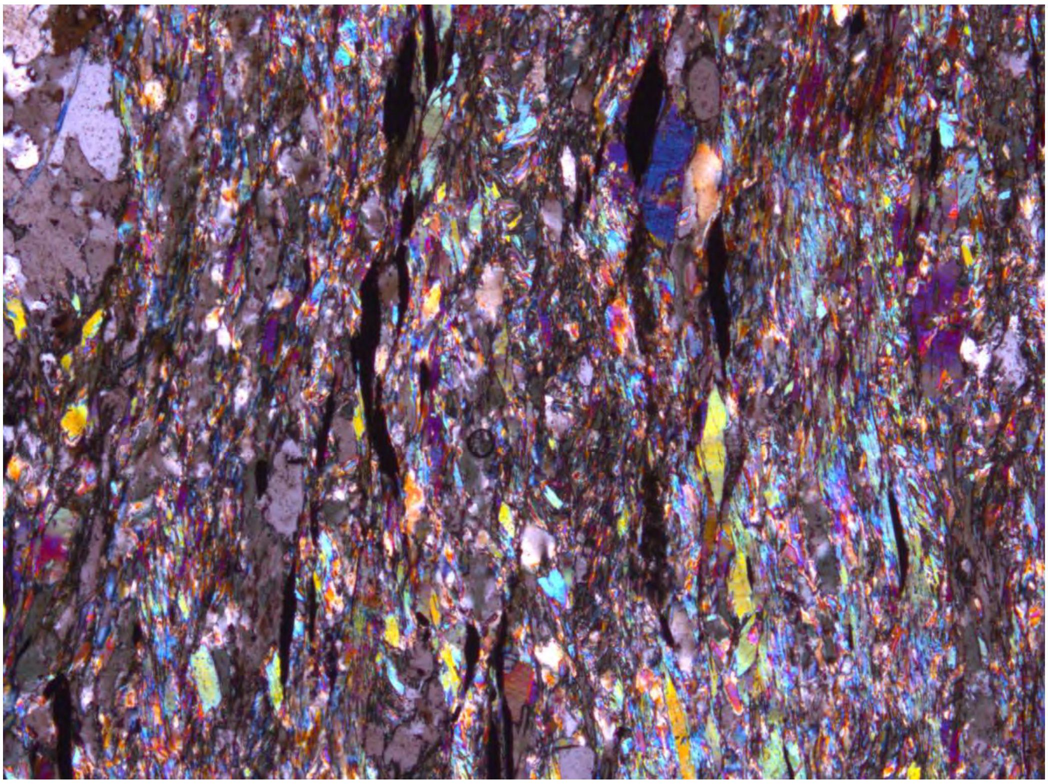

Figure 40: Thin section 4: Crossed-polarized light (XPL), 5× objective, turned.

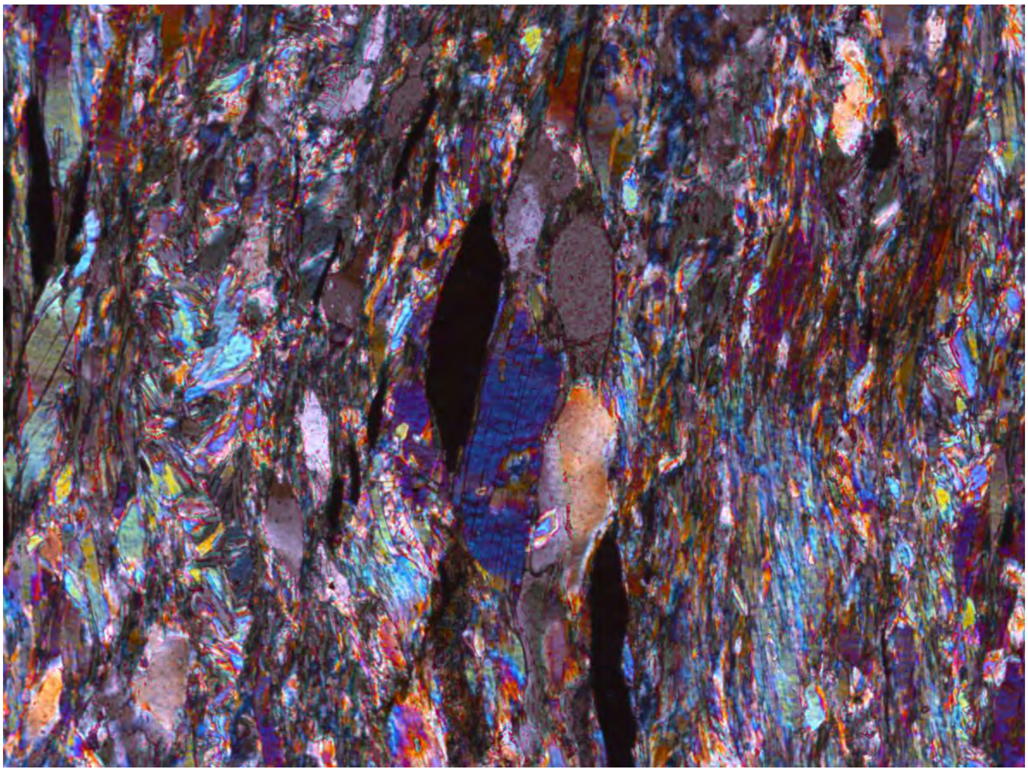

Figure 41: Thin section 4: Crossed-polarized light (XPL), 10× objective.

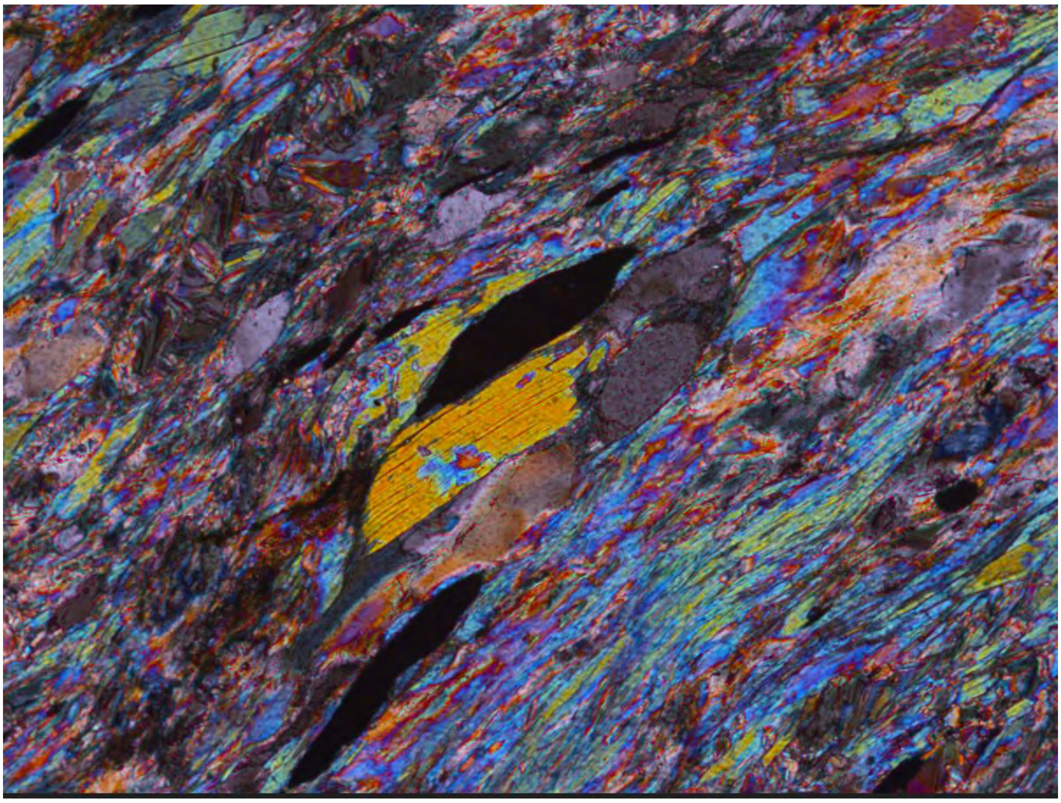

Figure 42: Thin section 4: Crossed-polarized light (XPL), 10× objective, turned.

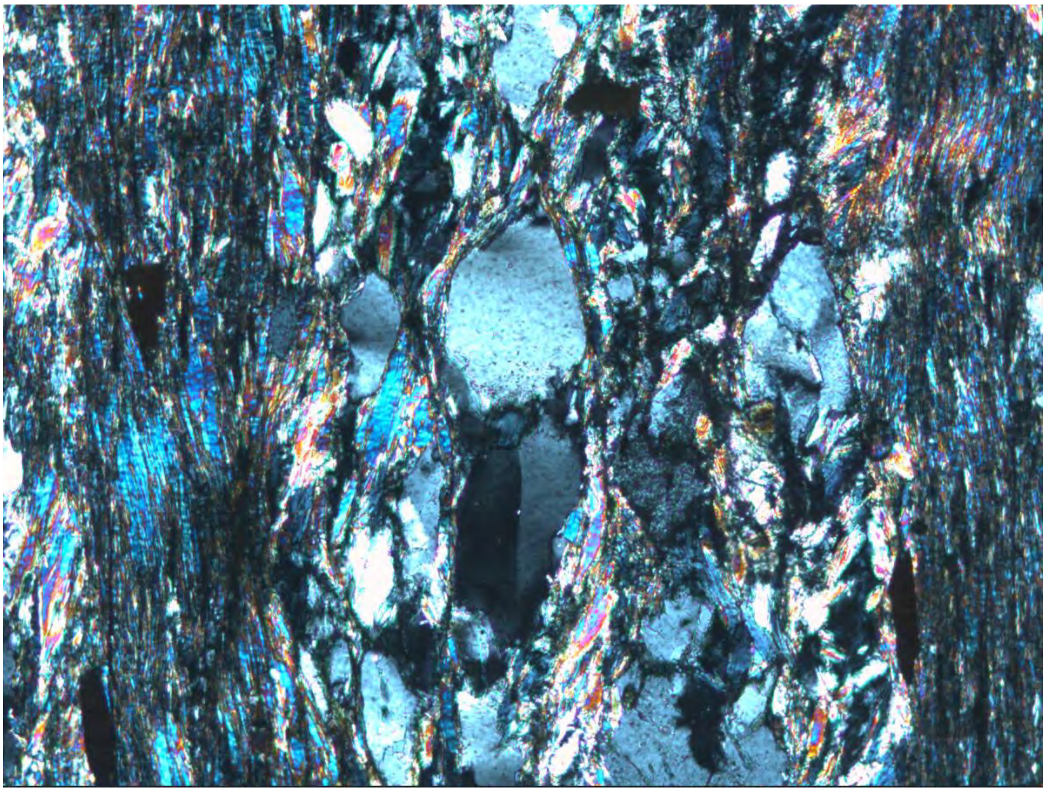

Figure 43: Thin section 4: Crossed-polarized light (XPL), 10× objective, Albit twin.

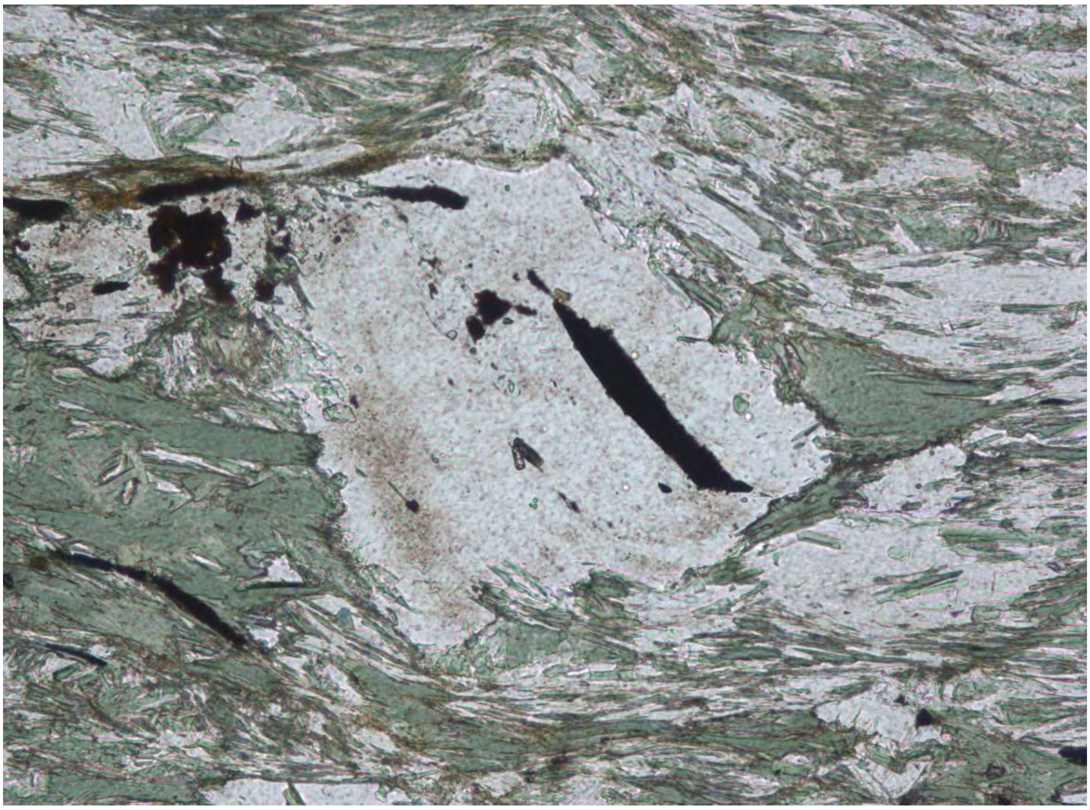

Figure 44: Thin section 4: Plane-polarized light (PPL), 10× objective, clast(sinistral).

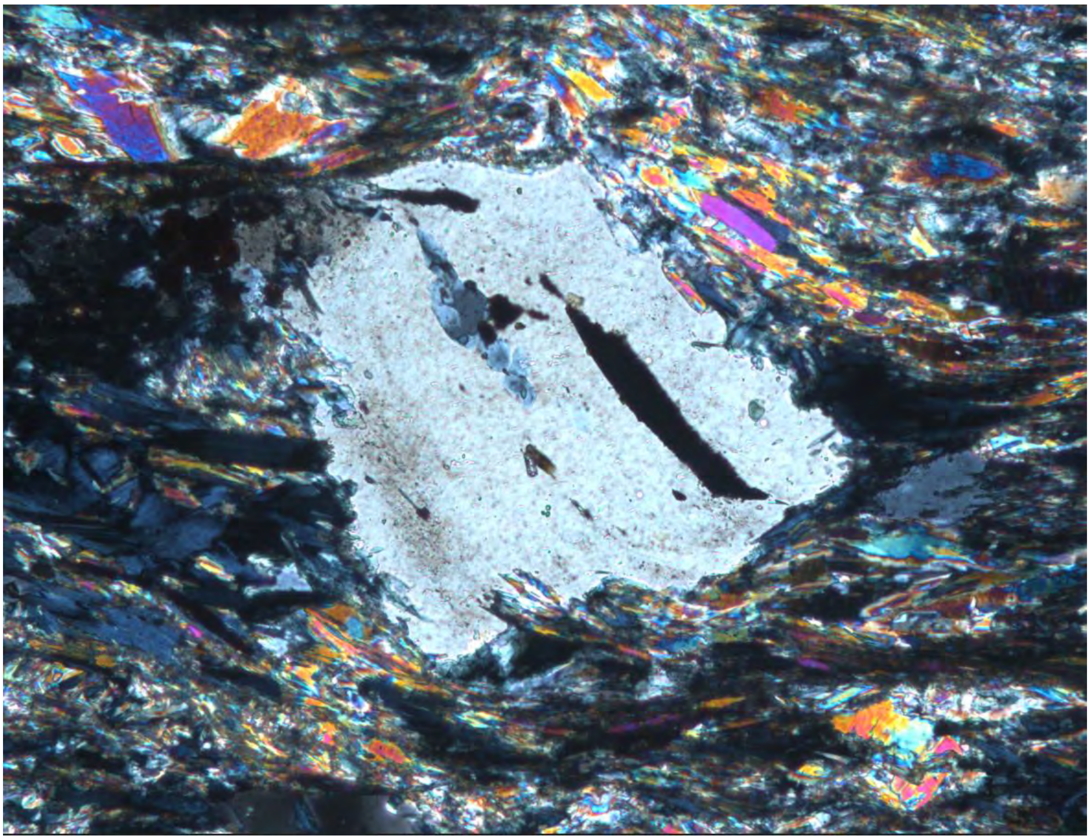

Figure 45: Thin section 4: Crossed-polarized light (XPL), 10× objective, clast(sinistral).

1. Sample Overview

The thin section represents a fine-grained, well-foliated phyllite dominated by Fe/Mg-rich chlorite, white mica, quartz, and albite. Accessory minerals include titanite, ilmenite, pyrite, tourmaline, zircon, apatite, and minor biotite. The rock shows a pronounced schistosity and a compositional banding consisting of quartz–feldspar layers and sheet-silicate layers.
No carbonate is present, in contrast to the previous sample (thin section 1).

2. Texture and Fabric

2.1 Schistosity

The rock displays a well-developed **schistose fabric**, defined by the alignment of:

- chlorite
- white mica
- biotite (minor)
- elongate quartz grains
- aligned albite crystals

2.2 Compositional banding

Two principal bands occur:

1. **Quartz–feldspar bands**
    - Quartz-rich, with albite and minor titanite/opaques.
    - Represent the more competent layers.
2. **Sheet-silicate bands (former S-surfaces)**
    - Chlorite + white mica ± biotite.
    - Represent the weaker, micaceous layers.

2.3 Additional textural features

- Schistosity-parallel microfractures.
- Zircon grains disrupt chlorite layers (reaction halos or microfracture trails).
- Albite porphyroclasts show internal alignment and define the main foliation with ilmenite.
- Very limited carbonate (effectively absent compared to previous thin section).

3. Mineral Constituents

3.1 Major minerals

- **Chlorite (Fe–Mg rich)**
    - Green in plane-polarized light (PPL), intense blue interference colors in crossed polars (XPL).
    - Locally hosts zircon inclusions with reaction halos.
- **White mica (muscovite/sericite)**
    - Colorless in PPL; low- to moderate-order interference colors in XPL.
- **Quartz**

    - Fine-grained, elongate grains aligned with foliation.
    - Occurs primarily in the quartz–feldspar compositional layers.
- **Plagioclase (albite)**
    - Colorless in PPL; exhibits polysynthetic twinning.
- **Minor biotite**
    - Strong pleochroism from light brown → dark brown.
    - Indicates temperatures approaching the biotite stability field (~350–400 °C).

3.2 Accessory minerals

- **Titanite (sphere)** – high relief, wedge-shaped, orange–brown interference colors.
- **Ilmenite** – opaque, black; locally altered to **leucoxene** (brownish).
- **Pyrite** – yellowish metallic reflectance.
- **Rutile** – high relief, reddish-brown tint; fine needles or prisms.
- **Tourmaline** – pleochroic (N∥ typically darker, N⊥ lighter); inverse pleochroic pattern compared to common silicates.
- **Zircon** – small rounded grains, often with pleochroic halos in chlorite.
- **Apatite** – small, round, colorless grains.

3.3 Secondary phases

- **Limonite** – brownish oxidation product, visible in fractures and alteration zones.

4. Metamorphic Conditions

The mineral assemblage suggests:

- Chlorite stability field
- Biotite present, indicating temperatures near or above ~350–400 °C
- Absence of garnet or amphibole → lower greenschist facies

Fe/Mg-rich chlorite + white mica + quartz + albite is typical of low- to medium-grade regional metamorphism.

5. Interpretation

5.1 Protolith

Likely a fine-grained sediment (e.g., pelitic to semi-pelitic mudstone/siltstone), lacking significant carbonate. The abundance of albite may indicate minor volcaniclastic input.

5.2 Deformation

- Foliation and alignment reflect ductile deformation**.**
- Quartz and Albite show preferred orientation and recrystallization.
- Schistosity-parallel fractures suggest late-stage strain.

5.3 Metamorphic evolution

- Development of biotite indicates heating above typical chlorite-only assemblages.
- Oxidation to limonite represents late retrograde alteration.

6. Petrographic Classification

Biotite-bearing chlorite phyllite with compositional banding and strong schistosity.

5. Thin section 5 (sinistral, Top E)

Figure 46: Thin section 5: scan. Top left E, top right W.

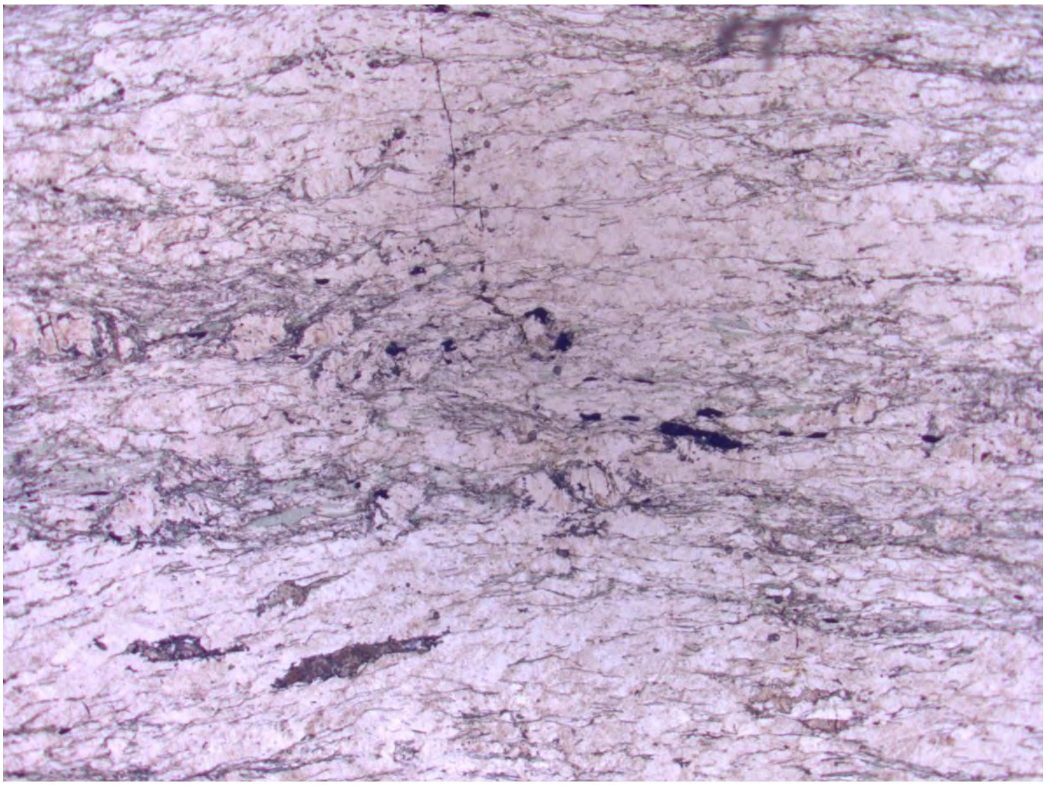

Figure 47: Thin section 5: Plane-polarized light (PPL), 1.25× objective.

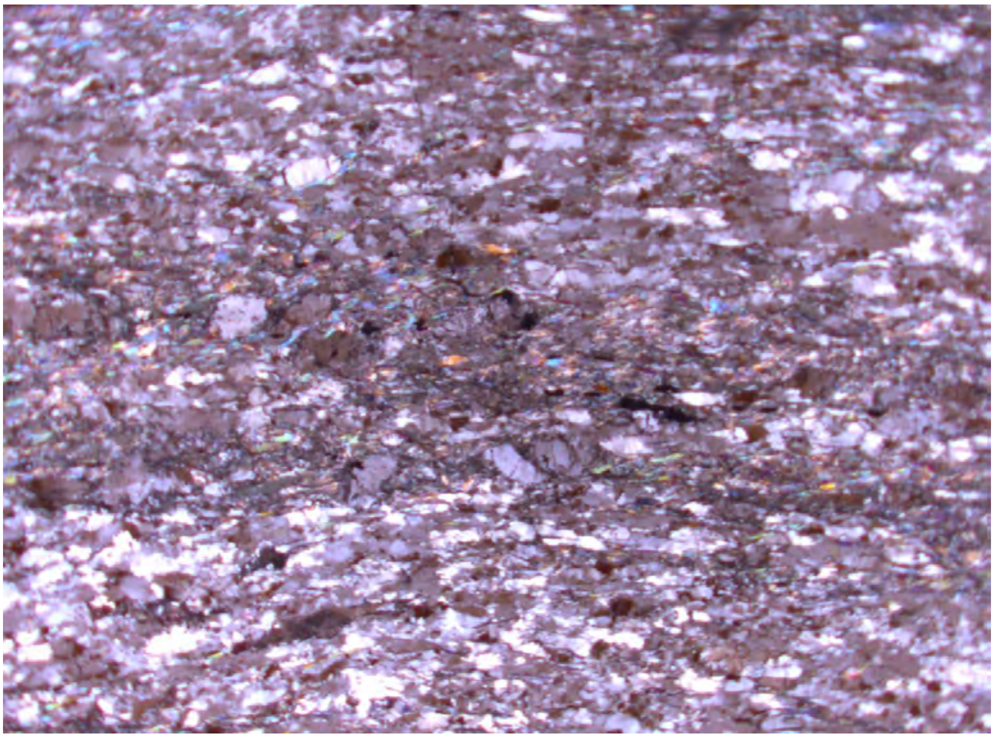
Figure 48: Thin section 5: Crossed-polarized light (XPL), 1.25× objective.

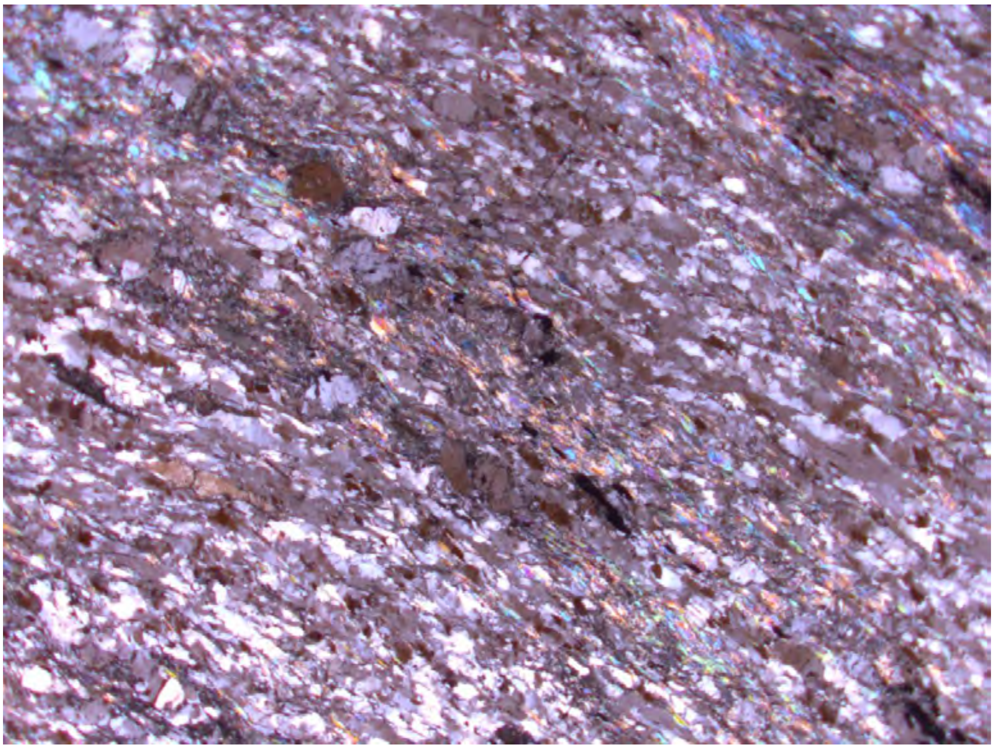
Figure 49: Thin section 5: Crossed-polarized light (XPL), 1.25× objective, turned.

Figure 50: Thin section 5: Plane-polarized light (PPL), 5× objective, Albit (twin), white mica, chlorite.

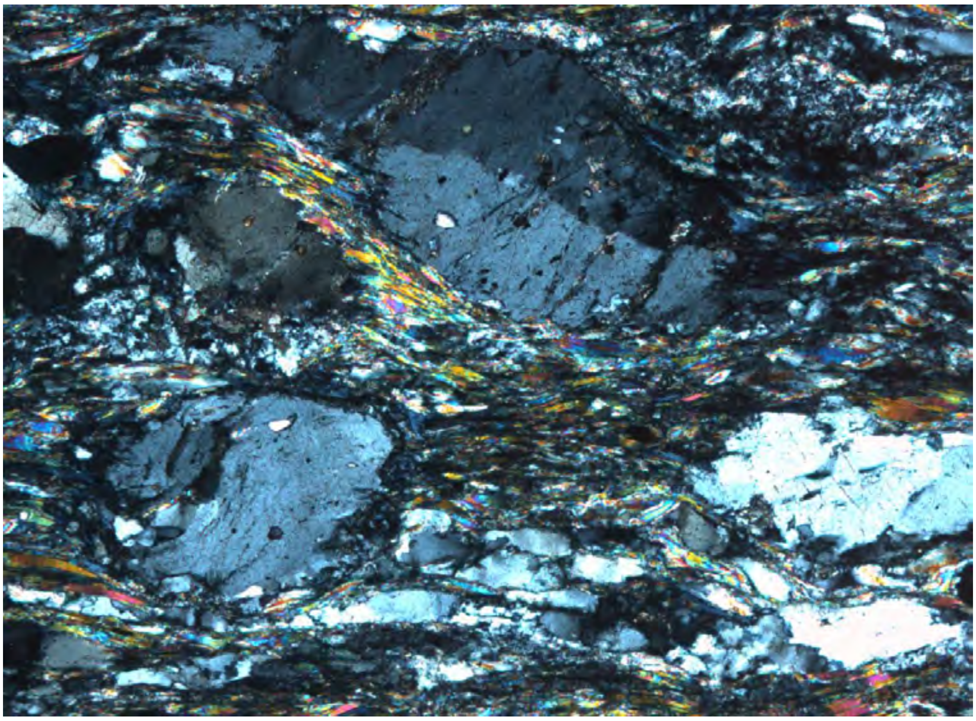

Figure 51: Thin section 5: Crossed-polarized light (XPL), 5× objective, Albit (twin), white mica (colored), chlorite (blue).

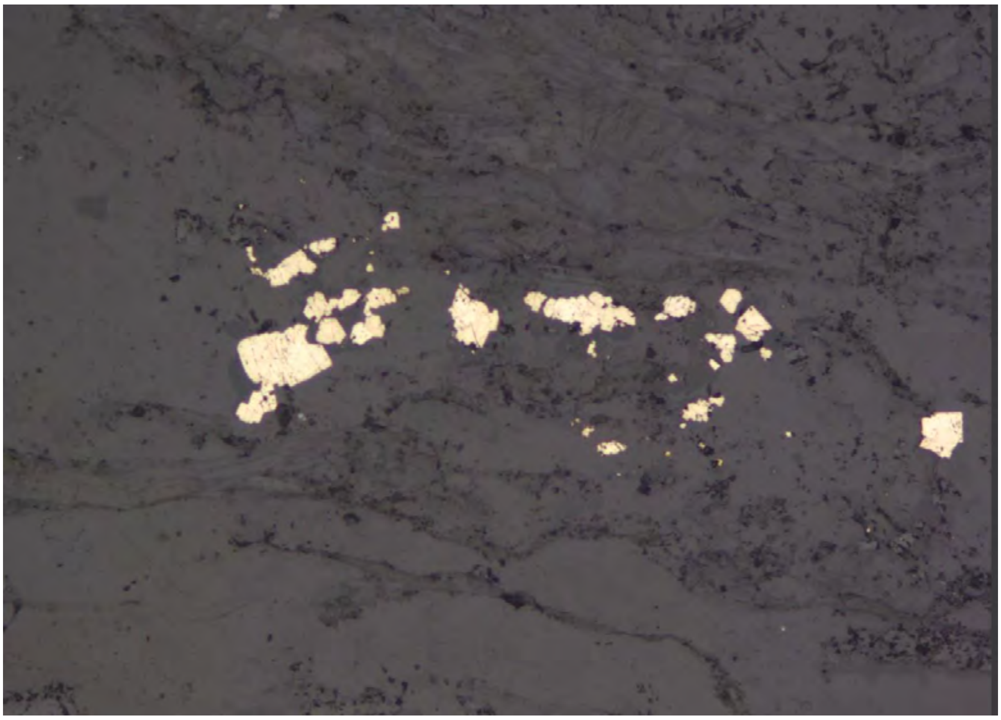

Figure 52: Thin section 5, Reflected light, 10x objective, pyrit.

1. Sample Overview

This thin section represents a medium- to fine-grained schist strongly enriched in sheet silicates and characterized by a well-developed foliation and compositional banding. The rock consists primarily of quartz, albite, subordinate microcline, carbonate, Fe-rich chlorite, and white mica. Accessory phases include ilmenite (partly altered toward leucoxene), tourmaline, and minor epidote. Secondary limonite occurs along fractures and alteration zones.

2. Texture and Fabric

2.1 Compositional banding

The thin section shows a pronounced compositional layering**,** consisting of:

1. **Quartz–feldspar–carbonate layers**
   - More competent, lighter-colored domains.
   - Dominated by quartz and albite
2. **Sheet-silicate bands (former S-surfaces)**
   - Chlorite + white mica
   - Weaker, phyllosilicate-rich layers

These bands are parallel to the main foliation.

2.2 Foliation

The **main foliation** is defined by:

- aligned sheet silicates (chlorite, white mica)
- aligned feldspar plates

The fabric is schistose and continuous, indicating ductile deformation.

2.3 Grain orientation

- Feldspar (especially albite), sheet silicates and quartz grains display preferred orientation.

3. Mineral Constituents

3.1 Major minerals

- **Quartz**
  - Fine- to medium-grained; elongated and aligned parallel to foliation.
  - Locally recrystallized, forming polygonal mosaics.
- **Albite (plagioclase)**
  - Common; colorless in PPL, polysynthetic twinning diagnostic.
  - Some grains occur as larger plates that reinforce foliation.
- **Microcline (subordinate)**
  - Identified by characteristic cross-hatched twinning.
  - Less abundant than albite.
- **Carbonate**
  - Present in moderate amounts; occurs in discrete patches or layers.
  - Likely metamorphic (calcareous sediment component).
- **Chlorite (Fe-rich)**
  - Blue interference colors in XPL; green in PPL.
  - Contributes significantly to the sheet-silicate layers.
- **White mica (muscovite)**
  - Colorless in PPL; low-order interference colors.
  - Well aligned along the foliation, forming continuous micaceous bands.

3.2 Accessory minerals

- **Ilmenite**
  - Opaque, black in PPL.
  - Partially altered to **leucoxene** (brownish alteration product).
- **Tourmaline**
  - Prismatic; pleochroic from dark to lighter tones depending on orientation.
- **Epidote (minor)**
  - Pistachio-green color; high relief; moderate interference colors.

3.3 Secondary phases

- **Limonite**
  - Brown, amorphous oxidation product.
  - Occurs along microfractures and grain boundaries.

4. Metamorphic Conditions

The mineral assemblage (chlorite + muscovite + albite + quartz + carbonate) indicates:

- low- to mid-greenschist facies metamorphism
- temperatures likely below the biotite-stability threshold (< ~350–380 °C), as biotite is absent
- epidote suggests a slightly calcareous or Fe-rich metamorphic environment

5. Interpretation

5.1 Protolith

Likely a feldspar-bearing siliciclastic sediment (e.g., an arkosic siltstone) given:

- presence of albite and microcline
- moderate carbonate content
- compositional heterogeneity

5.2 Deformation

- Foliation indicates ductile deformation.
- Former sedimentary has likely been transposed into the S-fabric.

5.3 Alteration

- Limonite reflects late-stage oxidation.
- Ilmenite → leucoxene alteration indicates subsolidus Ti-mobilization.

6. Petrographic Classification

Quartz–feldspar–chlorite schist with compositional banding and albite, carbonate-bearing layers.

6. Thin section 6 (unclear)

Figure 53: Thin section 6: scan. Top left E, top right W

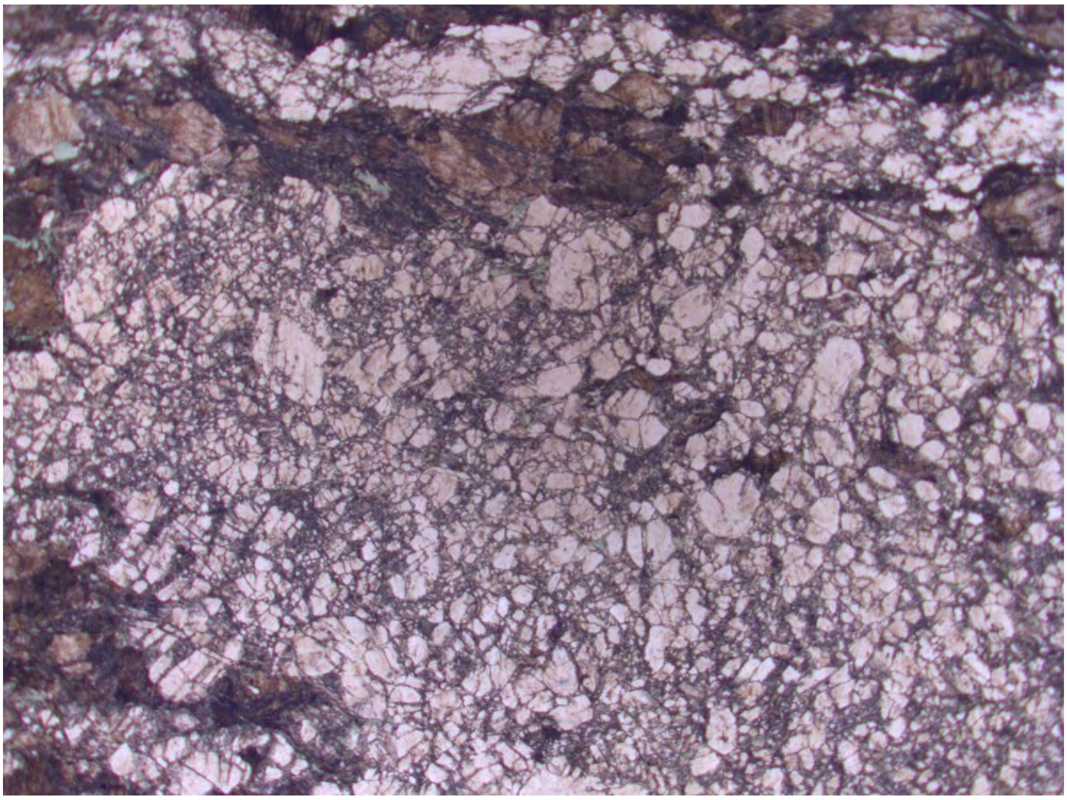

Figure 54: Thin section 6: Plane-polarized light (PPL), 1.25× objective.

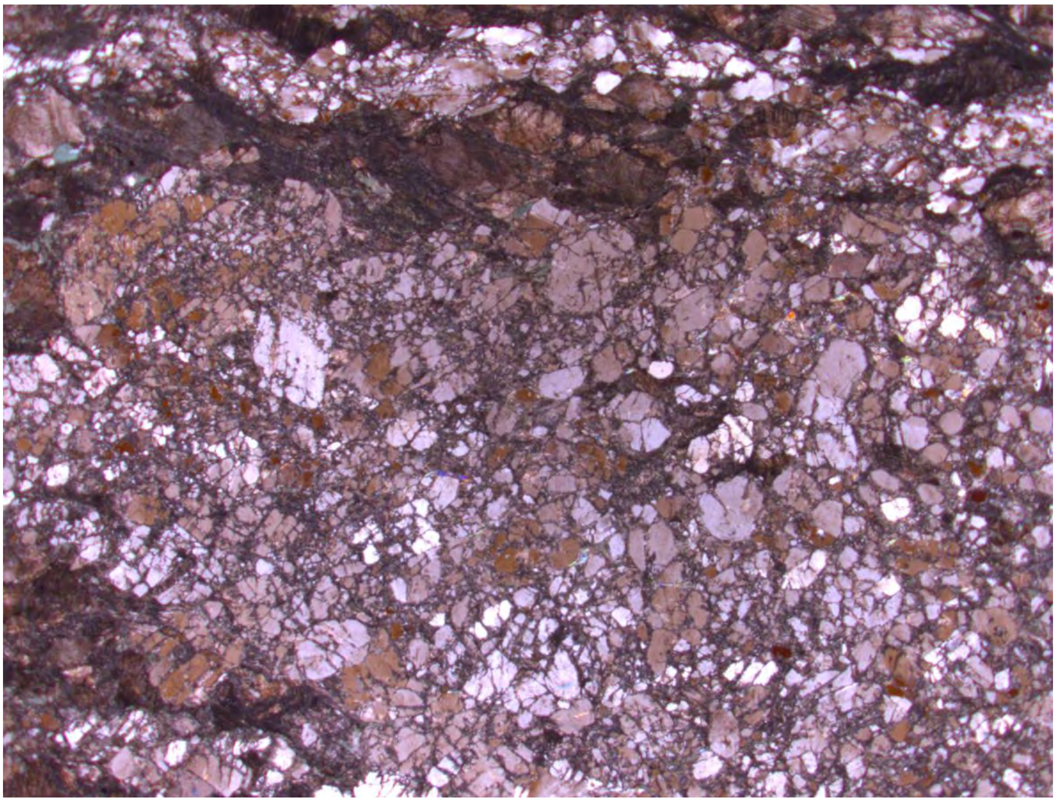
Figure 55: Thin section 6: Crossed-polarized light (XPL), 1.25× objective.

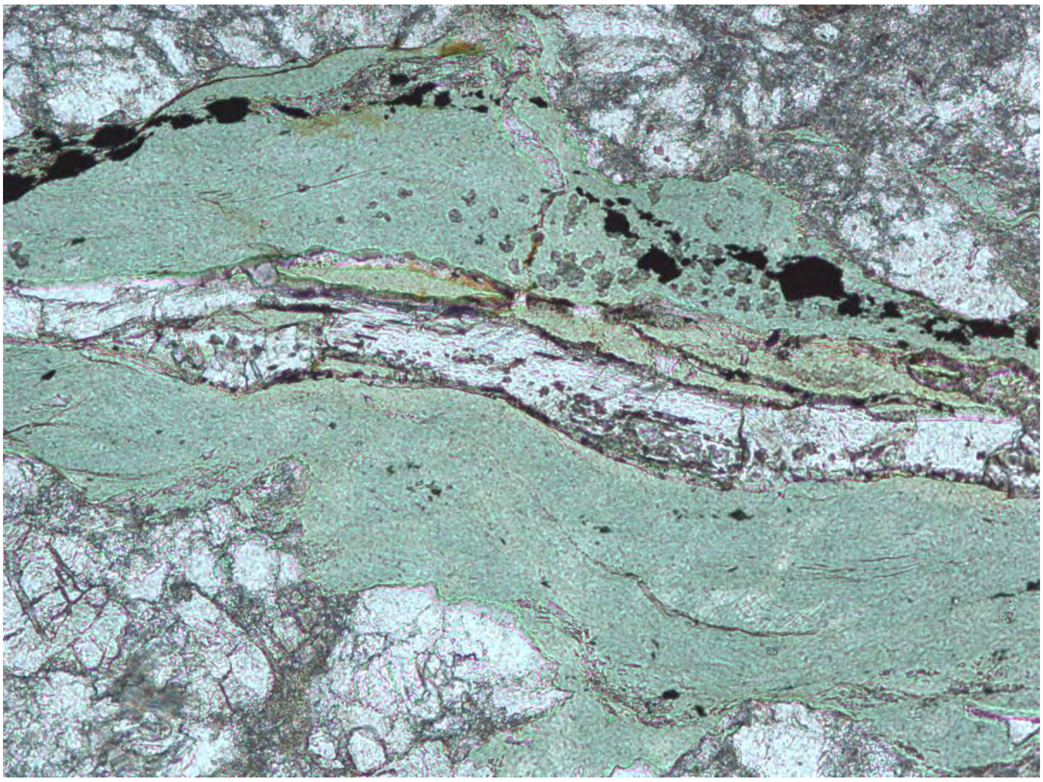
Figure 56: Thin section 1: Plane-polarized light (PPL), 10× objective, Chlorite (Fe/Mg rich).

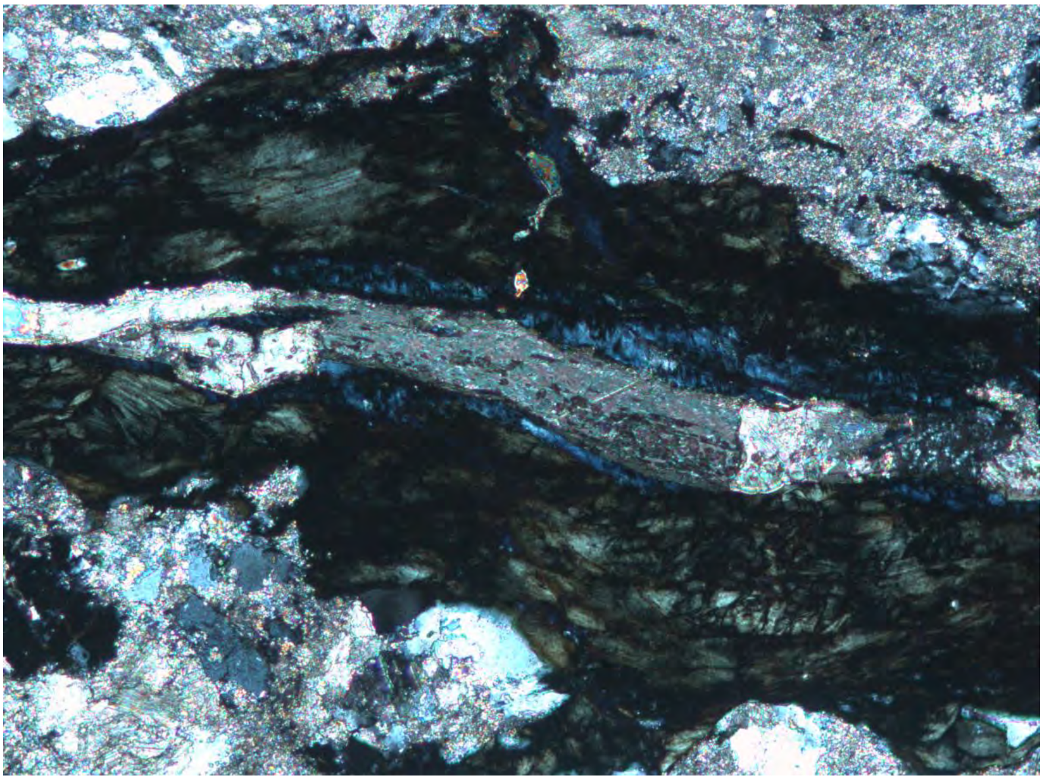
Figure 57: Thin section 6: Crossed-polarized light (XPL), 10× objective, chlorite (Fe/Mg rich).

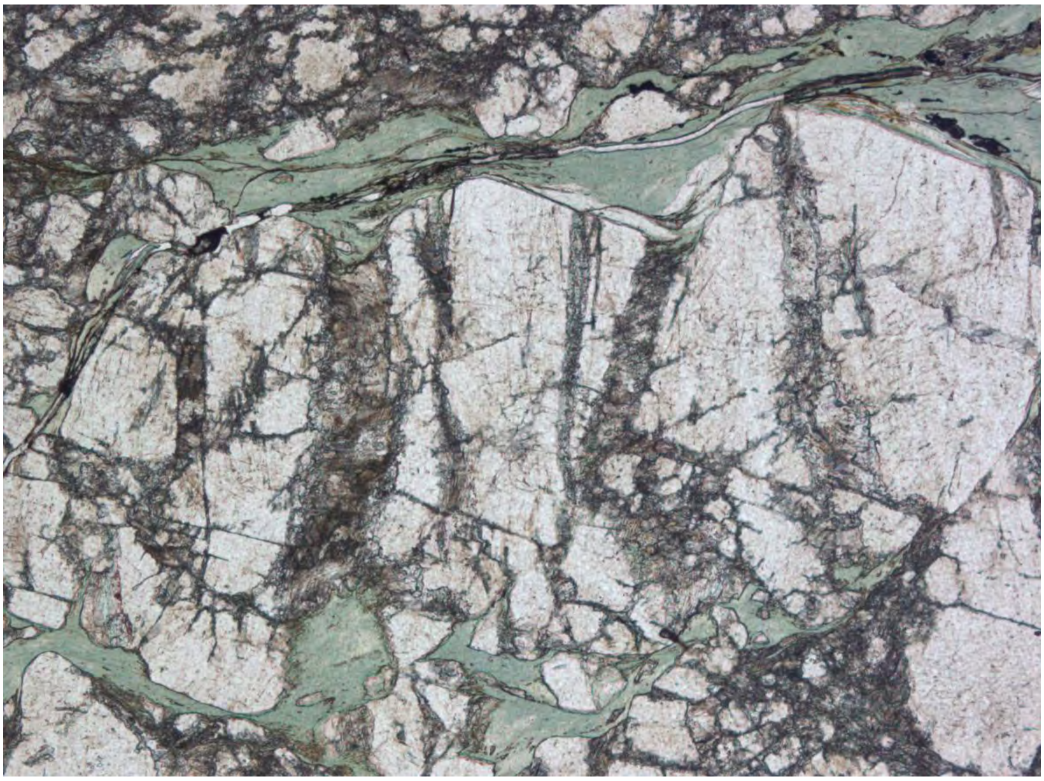
Figure 58: Thin section 6: Plane-polarized light (PPL), 5× objective, displaces broken grain (dextral).

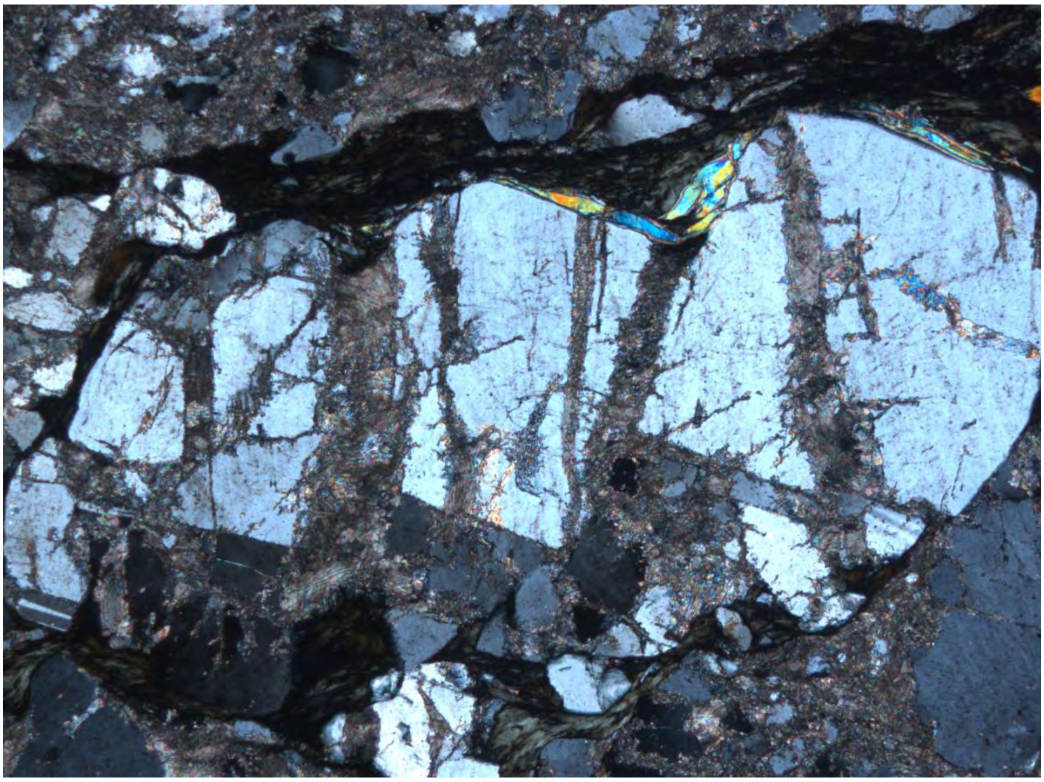

Figure 59: Thin section 6: crossed-polarized light (XPL), 5× objective, displaces broken grain (dextral).

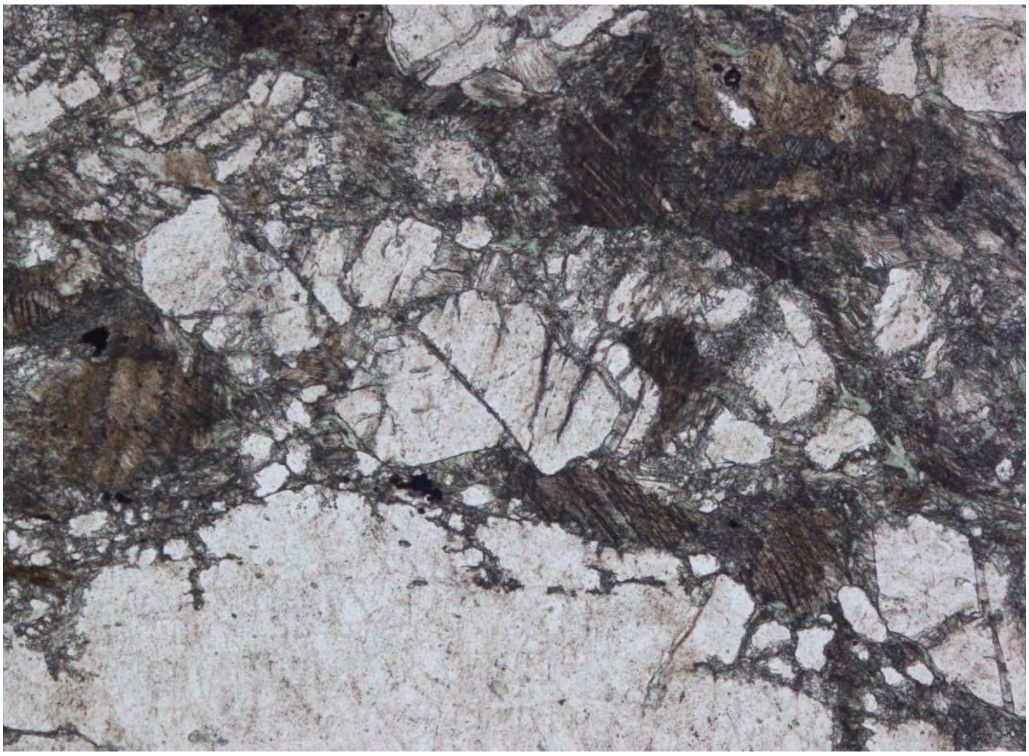

Figure 60: Thin section 6: Plane-polarized light (PPL), 5× objective, displaces broken grain (sinistral).

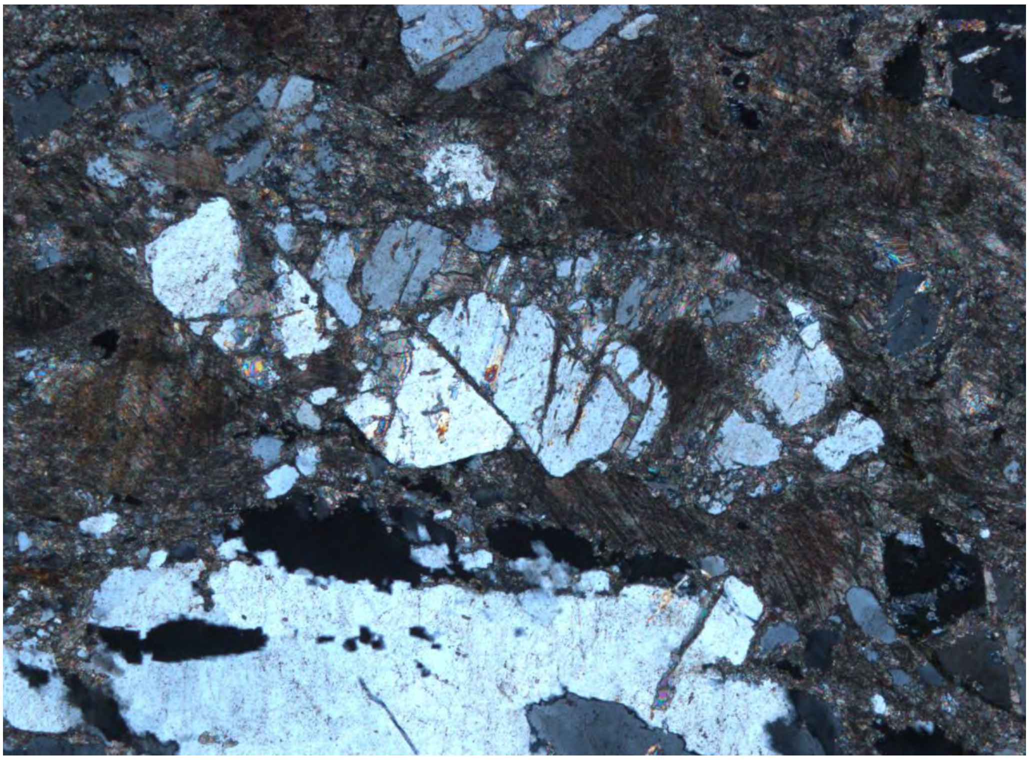
Figure 61: Thin section 6: crossed-polarized light (XPL), 5× objective, displaced broken grain (sinistral).

1. Sample Overview

The thin section represents a calc-silicate metamorphic rock characterized by abundant carbonates, quartz, feldspar, and multiple chlorite varieties. The mineral assemblage indicates low-grade metamorphism (lower greenschist facies), supported by the coexistence of Fe-rich and Mg-rich chlorite, the absence of biotite, and the presence of streaked quartz (undulatory/mylonitic lamellae) but no strained feldspar.
The rock exhibits irregular compositional layering and lensing, with a foliation parallel to these layers. Carbonate clasts and feldspar aligned. Cataclastic deformation.

2. Texture and Fabric

2.1 Compositional layering

The rock shows irregular, discontinuous layers and lenses**,** consisting of:

1. **Quartz–feldspar–carbonate layers**
    - More competent, light-colored bands.
    - Contain mylonitic quartz and aligned feldspar plates.
2. **Sheet-silicate layers**
    - Dominated by chlorite (Mg- and Fe-rich), with minor white mica.

2.2 Foliation

- Foliation is parallel to the compositional layering**.**
- Defined by alignment of carbonates, feldspar plates.

2.3 Mylonitic quartz fabric

- Quartz displays streaking/lamellae and incipient ribbon textures.
- These textures form at ~280 °C and above**.**
- Feldspar does not show comparable streaking (which begins > 450 °C).
  → Together, this constrains metamorphic temperature between **~**280–400 °C**.**

3. Mineral Constituents

3.1 Major minerals

- **Carbonates**
  - Large clasts.
  - Alignment relative to foliation.
- **Quartz**
  - Abundant.
  - Exhibits **streaked/mylonitic lamellae**, indicating temperatures ≥ ~280 °C.
  - Forms quartz-rich domains.
- **Feldspar**
  - **Microcline (K-feldspar):**
    - Cross-hatched twinning; moderate abundance.
  - **Plagioclase (albite-rich):**
    - Polysynthetic twinning; clear in PPL.
  - Present within feldspar–quartz bands and aligned within the foliation.
- **Chlorite (multiple varieties)**
  - Coexistence of **Mg-rich** and **Fe-rich** chlorite.
  - Blue interference colors in XPL.
  - Their presence side-by-side indicates **low-temperature metamorphism** (< ~350 °C).
  - Occurs in sheet-silicate layers and discontinuous lenses.
- **White mica (muscovite)**
  - Minor component.
  - Contributes slightly to the phyllosilicate layers.
- **Epidote**
  - High relief, yellowish/greenish; bright 3rd-order interference colors.
  - Occurs in scattered grains and small clusters.

3.2 Accessory and opaque minerals

- **Ilmenite**
  - Opaque, black; primary oxide phase.
  - No pyrite observed.

4. Metamorphic Conditions

The mineralogical evidence suggests:

4.1 Temperature

- Quartz streaking → ≥ **280 °C**
- Absence of feldspar streaking → ≤ **450 °C**
- Absence of biotite → ≤ **~400 °C**
- Coexisting chlorite varieties → **low-temperature greenschist facies (~300–350 °C)**

4.2 Pressure

- Typical of low- to medium-pressure regional metamorphism.

Overall metamorphic grade

Lower greenschist facies**.**

5. Interpretation

5.1 Protolith

Likely a calcareous sediment **or** impure limestone with siliciclastic or volcaniclastic input.
Evidence:

- Abundant carbonates
- Quartz + feldspar
- Epidote + chlorite suggests Ca-, Fe- and Mg-rich composition
- Irregular layering consistent with pre-metamorphic sedimentary structures

5.2 Deformation

- Carbonate clasts, feldspar grains, and quartz fibers show preferred orientation**.**
- Mylonitic quartz indicates significant shear deformation at low temperatures.
- Shear sense can not be determined (evidence of sinistral and dextral (displaced broken grain).

5.3 Chemical and metamorphic evolution

- Coexistence of Fe/Mg chlorite phases suggests variable fluid composition or incomplete metamorphic equilibration.
- Ilmenite is primary; absence of pyrite indicates oxidizing or sulfate-poor conditions.

6. Petrographic Classification

Calc-silicate chlorite schist / chlorite-bearing calc-silicate rock
with mylonitic quartz fabrics and compositional banding.

7. Thin section7 (sinistral, top W)

Figure 62: Thin section 7: scan. Top left W, top right E.

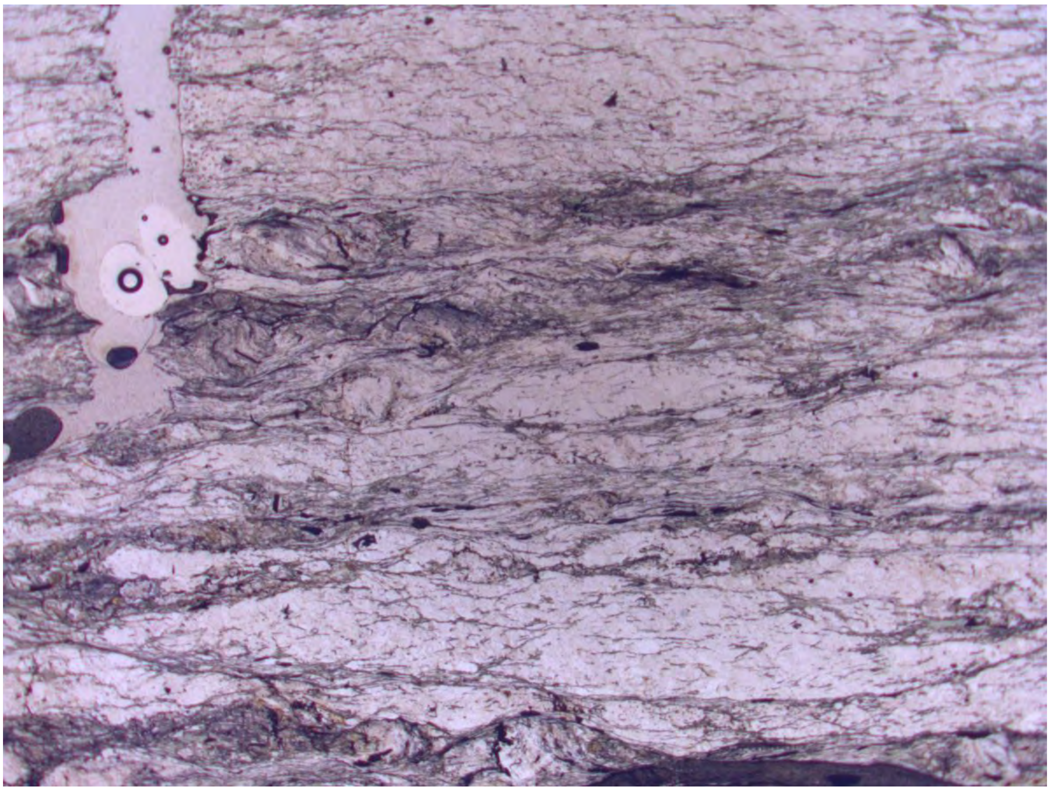

Figure 63: Thin section 7: Plane-polarized light (PPL), 1.25× objective.

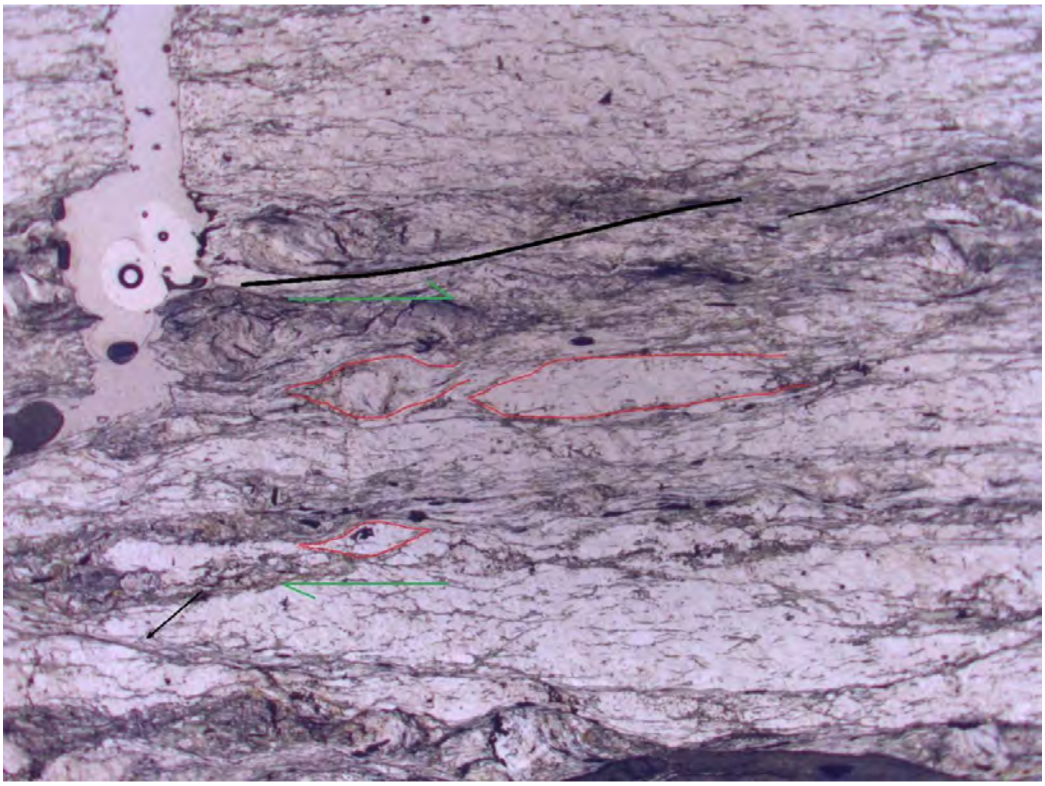

Figure 64: Thin section 7: Plane-polarized light (PPL), 1.25× objective, marked.

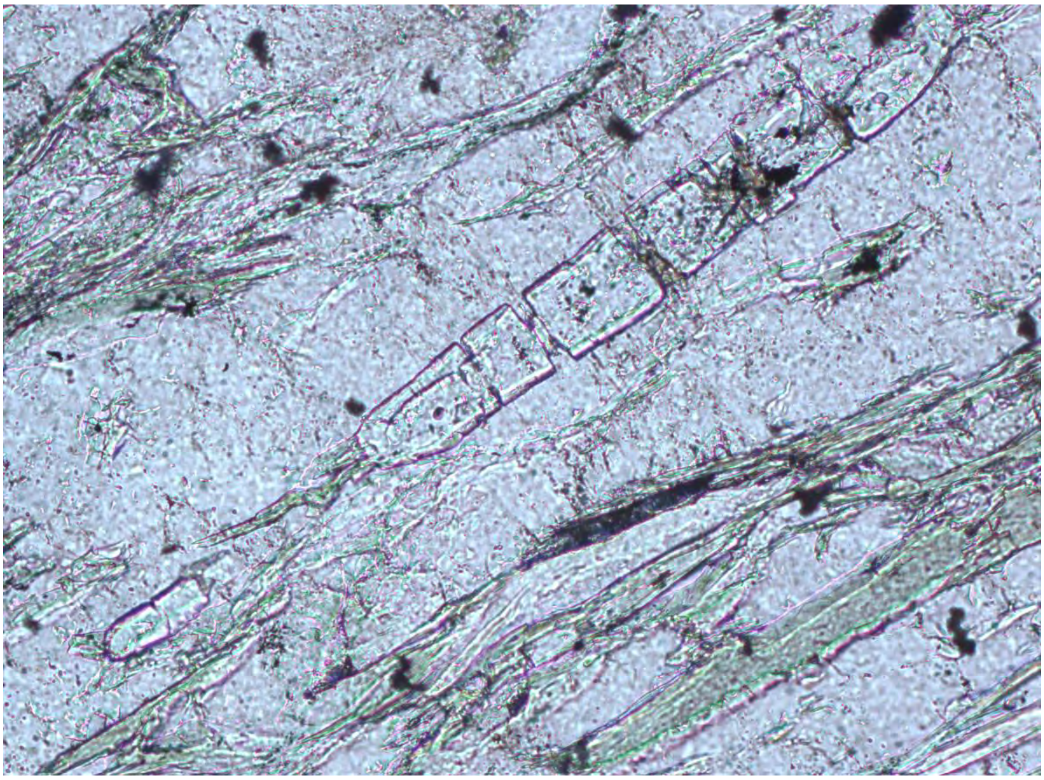

Figure 65: Thin section 7: Plane-polarized light (PPL), 20× objective, fractured apatite.

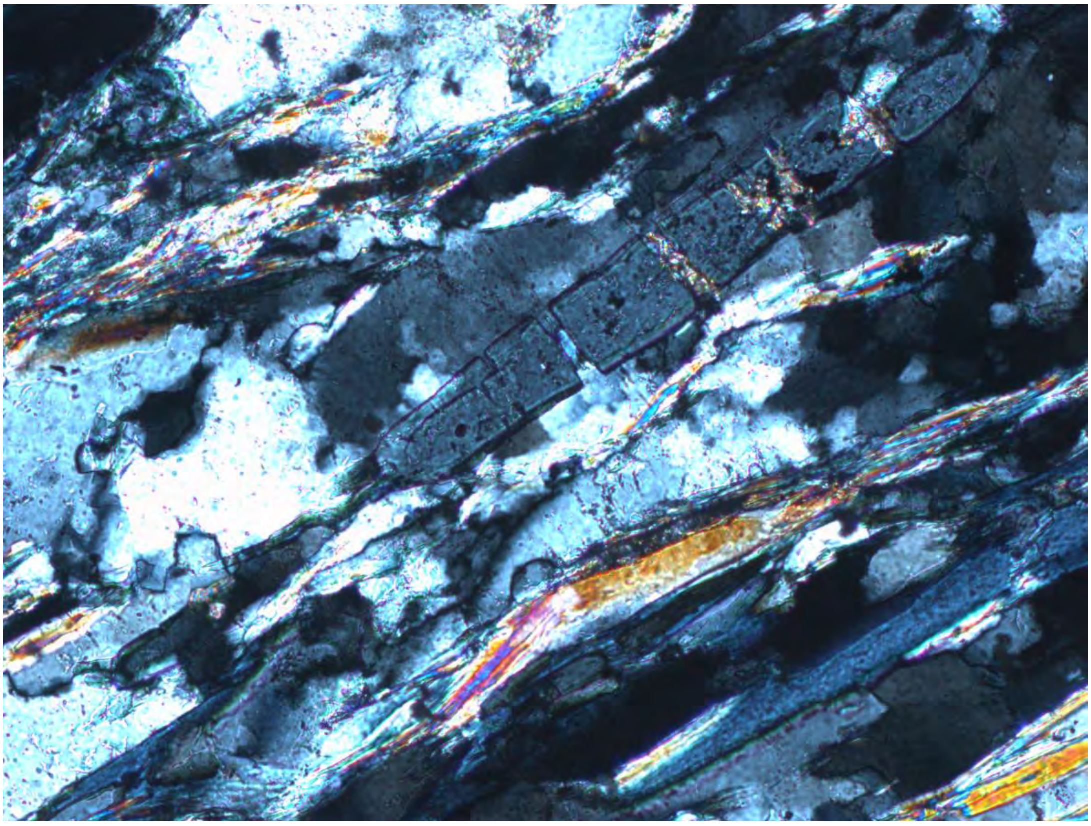

Figure 66: Thin section 7: Crossed-polarized light (XPL), 20× objective, fractured apatite.

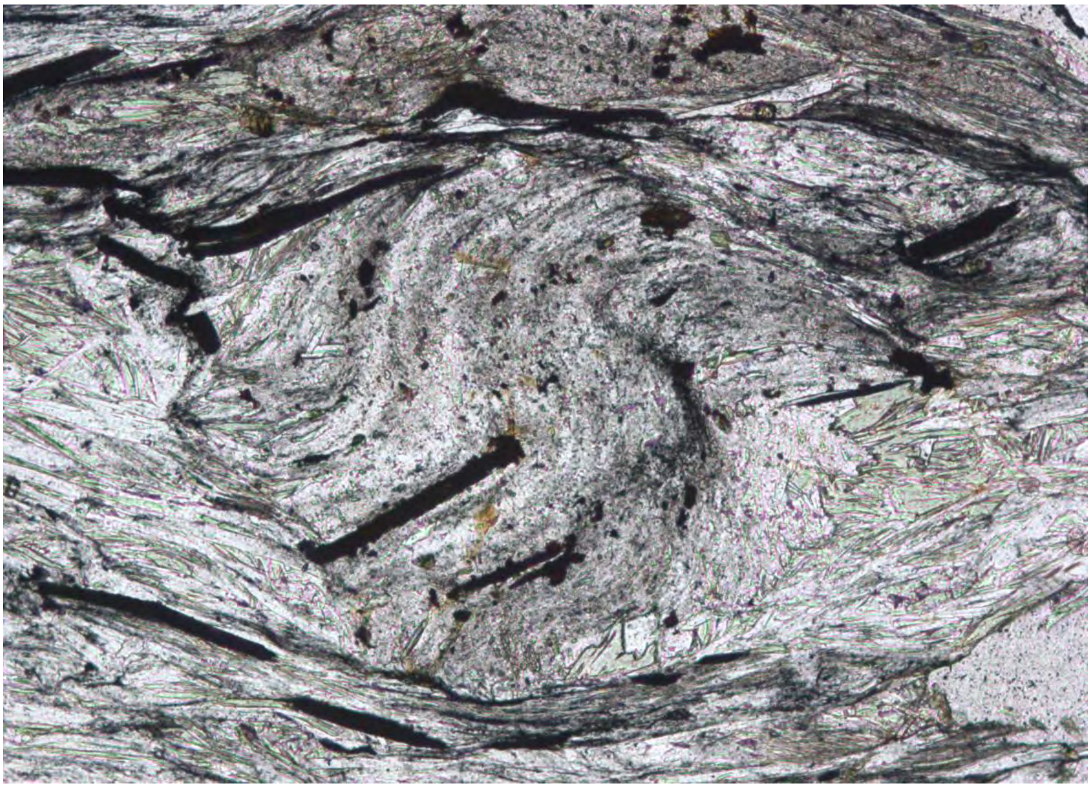

Figure 67: Thin section 7: Plane-polarized light (PPL), 10× objective, clast (sinistral).

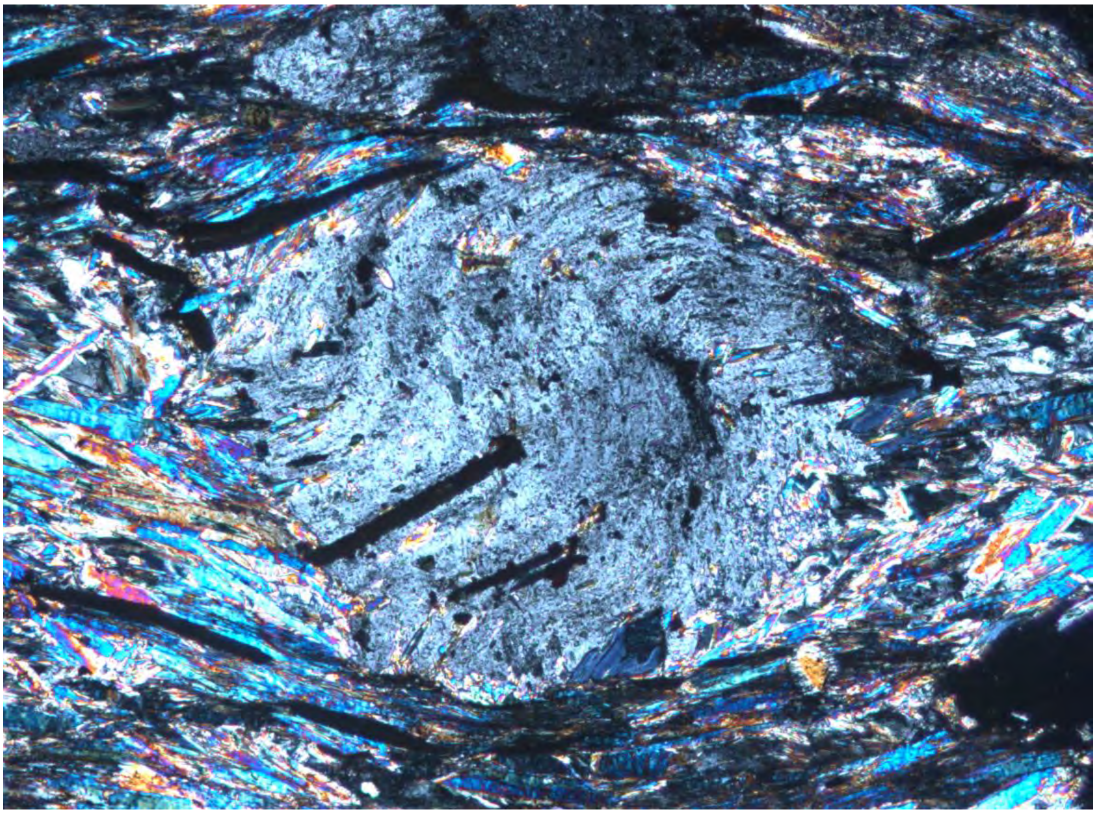
Figure 68: Thin section 7: Crossed-polarized light (XPL), 10× objective, clast (sinistral).

1. Sample Overview

This thin section represents a schist (not a phyllite)**,** distinguished by its relatively coarse-grained white mica plates (up to ~2 mm), large, well-shaped feldspar crystals, and a quartz-dominated matrix. The rock shows pronounced compositional layering and lensing, including quartz–feldspar layers and sheet-silicate (chlorite–mica) layers. The mineralogy and textures are broadly similar to Thin Section 5, but the coarser mica and feldspar grains and the stronger schistosity classify this sample as a schist rather than a phyllite**.**
The assemblage includes quartz, albite, chlorite (Fe-rich), minor carbonates, and accessory minerals such as tourmaline, apatite, ilmenite, pyrite, and epidote.

2. Texture and Fabric

2.1 Schistosity

The rock shows a strong schistose fabric, formed by:

- coarse white mica plates
- aligned albite crystals
- elongate quartz grains
- aligned chlorite flakes

This fabric is significantly coarser and more pronounced than in phyllite-grade rocks.

2.2 Compositional layering and lenses

Two principal compositional domains occur:

1. **Quartz–feldspar layers**

- Dominant component.
- Competent layers with strong mineral stretching.

2. **Sheet-silicate layers**
   - Chlorite-rich with subordinate white mica.

These produce a banded and lensoidal structure, common in low-grade metamorphic schists.

2.3 Grain alignment

- Albite crystals oriented along the foliation.
- Quartz shows preferred elongation and subgrain development.

3. Mineral Constituents

3.1 Major minerals

- **Quartz**
  - Dominant phase.
  - Occurs in both continuous bands and lenticular domains.
- **Feldspar (albite)**
  - Occurs as large, well-shaped (form-defined) crystals.
  - Polysynthetic twinning diagnostic of albite.
  - Aligned within foliation.
  - Microcline (K-feldspar) is absent.
- **Chlorite**
  - Fe-rich chlorite showing blue interference colors in XPL.
  - Occurs in micaceous layers and lenses.
- **White mica (muscovite)**
  - Long, coarse flakes (up to ~2 mm).
  - Colorless in PPL with bright interference colors.

3.2 Accessory minerals

- **Carbonate** (minor)
  - Present in small patches or thin layers.
  - Less abundant than in earlier thin sections.
- **Tourmaline**
  - Occurs as isolated prismatic grains.
  - Indicative of sedimentary (boron-rich) protoliths or metamorphic fluid involvement.
- **Apatite**
  - Small rounded grains scattered throughout.
- **Ilmenite**
  - Opaque, black.
  - Commonly altered to leucoxene (brown), reflecting oxidation or breakdown.
- **Pyrite**
  - Minor opaque phase with yellowish metallic luster.

- **Epidote**
    - Pistachio-green color; high relief.
    - Occurs in small amounts.

3.3 Secondary phases

- **Limonite**
    - Brown, amorphous alteration product.
    - Represents late-stage oxidation.
    - Leucoxene is derived from ilmenite breakdown, common in all thin sections.

4. Metamorphic Conditions

The mineralogy indicates:

- Greenschist facies, likely at low to moderate temperatures (~280–400 °C).
- The presence of Fe-rich chlorite and absence of biotite suggests temperatures near the lower end of the greenschist stability field.
- Coarse muscovite indicates higher strain and more advanced recrystallization compared to phyllite-grade rocks.
- Shear sense: sinistral (based on clasts, left-dipping shear bands).

5. Interpretation

5.1 Protolith

Likely a **feldspathic or siliceous sedimentary rock** (e.g., arkosic siltstone or graywacke), with:

- quartz dominance
- albite-rich feldspar
- minor carbonate
- accessory boron-bearing tourmaline

5.2 Deformation

- Foliation and elongation of quartz and feldspar indicate significant ductile deformation.
- Compositional layering suggests transposition of earlier bedding or primary sedimentary structures.

5.3 Alteration

- Limonite and leucoxene represent oxidation and ilmenite breakdown.
- Some accessory minerals (e.g., epidote) reflect Ca–Fe mobility during metamorphism.

6. Petrographic Classification

Quartz–feldspar–chlorite schist with coarse muscovite and compositional banding.

Appendix B: Structural data

Longitude	Latitude	DipDirection	Dip	Type	Location	Height (m)	Description
10.115510	46.564500	345	26	bedding	Valley 1	2031	C
10.115510	46.564500	0	26	bedding	Valley 1	2031	S
10.115510	46.564500	263	11	lineation	Valley 1	2031	
10.115695	46.564434	15	29	bedding	Valley 1	2052	
10.115553	46.564476	279	10	bedding	Valley 1	2054	
10.115510	46.564500	346	22	bedding	Valley 1	2054	
10.115510	46.564500	339	33	bedding	Valley 1	2054	
10.115510	46.564500	277	19	bedding	Valley 1	2054	
10.115489	46.564445	150	12	bedding	Valley 1	2054	
10.115373	46.564529	349	28	bedding	Valley 1	2056	
10.113600	46.566490	335	53	bedding	Valley 1	2081	
10.113600	46.566490	340	53	bedding	Valley 1	2081	
10.113600	46.566490	22	24	bedding	Valley 1	2081	
10.113600	46.566490	12	23	bedding	Valley 1	2081	
10.113600	46.566490	80	14	lineation	Valley 1	2081	
10.113600	46.566490	299	8	lineation	Valley 1	2081	
10.113600	46.566490	290	13	lineation	Valley 1	2081	
10.113600	46.566490	305	8	lineation	Valley 1	2081	
10.113600	46.566490	303	13	lineation	Valley 1	2081	
10.113828	46.566403	5	20	bedding	Valley 1	2100	
10.113703	46.566399	20	21	bedding	Valley 1	2100	
10.113633	46.566428	15	22	bedding	Valley 1	2101	
10.113633	46.566428	80	14	lineation	Valley 1	2101	
10.113600	46.566490	28	18	bedding	Valley 1	2101	
10.113600	46.566490	80	14	lineation	Valley 1	2101	
10.113599	46.566578	15	28	bedding	Valley 1	2101	
10.113600	46.566490	338	56	bedding	Valley 1	2101	
10.113562	46.566512	18	22	bedding	Valley 1	2103	
10.125882	46.554475	118	69	bedding	Valley 1	1860	
10.125722	46.554291	113	71	bedding	Valley 1	1860	
10.125670	46.554370	121	70	bedding	Valley 1	1860	
10.124669	46.554243	301	31	bedding	Valley 1	1864	
10.124648	46.554153	93	32	bedding	Valley 1	1864	
10.124530	46.554090	300	31	bedding	Valley 1	1864	
10.124530	46.554090	89	37	bedding	Valley 1	1864	
10.124530	46.554090	121	14	bedding	Valley 1	1864	
10.124530	46.554090	72	47	bedding	Valley 1	1864	
10.124530	46.554090	116	8	bedding	Valley 1	1864	
10.124398	46.554166	295	18	bedding	Valley 1	1864	
10.124203	46.554166	145	39	bedding	Valley 1	1864	
10.122200	46.555340	70	29	bedding	Valley 1	1873	

10.122200	46.555340	4	10	lineation	Valley 1	1873	
10.122313	46.555461	18	84	bedding	Valley 1	1880	
10.122248	46.555507	97	15	bedding	Valley 1	1880	
10.122248	46.555507	100	83	bedding	Valley 1	1880	
10.122177	46.555507	191	81	bedding	Valley 1	1880	
10.122071	46.555577	140	83	bedding	Valley 1	1880	
10.122066	46.555603	156	21	bedding	Valley 1	1880	
10.122039	46.555519	141	27	bedding	Valley 1	1880	
10.122671	46.555135	180	15	lineation	Valley 1	1881	
10.122671	46.555135	171	23	bedding	Valley 1	1881	
10.122650	46.555200	180	15	lineation	Valley 1	1881	
10.122650	46.555200	100	30	bedding	Valley 1	1881	
10.122650	46.555200	128	26	bedding	Valley 1	1881	
10.122650	46.555200	299	13	bedding	Valley 1	1881	Shear Band
10.122650	46.555200	103	25	bedding	Valley 1	1881	
10.122650	46.555200	180	15	lineation	Valley 1	1881	
10.122650	46.555200	101	46	bedding	Valley 1	1881	
10.122590	46.555250	103	25	bedding	Valley 1	1881	
10.122546	46.555570	168	33	foliation	Valley 1	1881	
10.122532	46.555561	236	16	bedding	Valley 1	1881	
10.122520	46.555228	102	17	bedding	Valley 1	1881	
10.122468	46.555367	104	25	foliation	Valley 1	1881	
10.122468	46.555367	88	21	lineation	Valley 1	1881	
10.122354	46.555464	62	15	bedding	Valley 1	1881	
10.122348	46.555483	150	32	foliation	Valley 1	1881	
10.122345	46.555456	16	7	foliation	Valley 1	1881	
10.122340	46.555440	170	24	bedding	Valley 1	1881	
10.122340	46.555440	210	15	bedding	Valley 1	1881	
10.122340	46.555440	94	21	lineation	Valley 1	1881	
10.122340	46.555440	205	22	bedding	Valley 1	1881	
10.122340	46.555440	168	23	bedding	Valley 1	1881	
10.122340	46.555440	210	15	bedding	Valley 1	1881	
10.122340	46.555440	94	21	lineation	Valley 1	1881	
10.122303	46.555495	17	8	foliation	Valley 1	1881	
10.122303	46.555495	119	17	foliation	Valley 1	1881	
10.122303	46.555495	130	16	foliation	Valley 1	1881	
10.122303	46.555495	113	30	foliation	Valley 1	1881	
10.122303	46.555495	118	30	foliation	Valley 1	1881	
10.122303	46.555495	78	30	foliation	Valley 1	1881	
10.122303	46.555495	141	16	lineation	Valley 1	1881	
10.122303	46.555495	148	11	lineation	Valley 1	1881	
10.122303	46.555495	78	23	lineation	Valley 1	1881	
10.122303	46.555495	125	18	foliation	Valley 1	1881	
10.122303	46.555495	124	26	foliation	Valley 1	1881	
10.122303	46.555495	131	15	foliation	Valley 1	1881	

10.122303	46.555495	118	15	foliation	Valley 1	1881	
10.122303	46.555495	94	16	foliation	Valley 1	1881	
10.122303	46.555495	128	34	foliation	Valley 1	1881	
10.122303	46.555495	64	31	foliation	Valley 1	1881	
10.122303	46.555495	141	16	lineation	Valley 1	1881	
10.122303	46.555495	148	11	lineation	Valley 1	1881	
10.122303	46.555495	98	20	lineation	Valley 1	1881	
10.122287	46.555442	125	18	foliation	Valley 1	1881	
10.122273	46.555410	2	6	lineation	Valley 1	1881	
10.122273	46.555410	85	36	foliation	Valley 1	1881	
10.122224	46.555551	74	25	lineation	Valley 1	1881	
10.122206	46.555514	76	26	bedding	Valley 1	1881	
10.122206	46.555514	95	26	bedding	Valley 1	1881	
10.122206	46.555514	70	26	bedding	Valley 1	1881	
10.122206	46.555514	74	25	lineation	Valley 1	1881	
10.122206	46.555514	41	26	bedding	Valley 1	1881	
10.122199	46.555500	92	25	bedding	Valley 1	1881	
10.122141	46.555506	158	20	foliation	Valley 1	1881	
10.122139	46.555445	140	8	foliation	Valley 1	1881	
10.122128	46.555500	84	30	bedding	Valley 1	1881	
10.122087	46.555607	102	26	foliation	Valley 1	1881	
10.122210	46.555580	68	18	bedding	Valley 1	1882	
10.122210	46.555580	178	8	lineation	Valley 1	1882	
10.122210	46.555580	86	18	bedding	Valley 1	1882	
10.122190	46.555490	167	16	bedding	Valley 1	1882	
10.122190	46.555490	152	21	bedding	Valley 1	1882	
10.121959	46.555577	178	8	lineation	Valley 1	1882	
10.122644	46.555158	150	14	lineation	Valley 1	1883	
10.122590	46.555250	150	14	lineation	Valley 1	1883	
10.122590	46.555250	150	14	lineation	Valley 1	1883	
10.124226	46.554652	131	65	bedding	Valley 1	1891	
10.124190	46.554570	150	40	bedding	Valley 1	1891	
10.124190	46.554570	156	64	bedding	Valley 1	1891	
10.124190	46.554570	150	45	bedding	Valley 1	1891	
10.124190	46.554570	166	30	bedding	Valley 1	1891	
10.124080	46.554587	161	62	bedding	Valley 1	1891	
10.121435	46.556034	127	21	bedding	Valley 1	1899	
10.121417	46.555929	60	35	bedding	Valley 1	1899	
10.121330	46.556000	50	40	lineation	Valley 1	1899	
10.121330	46.556000	107	20	bedding	Valley 1	1899	
10.121306	46.556041	65	41	bedding	Valley 1	1899	
10.121226	46.555952	104	23	bedding	Valley 1	1899	
10.119350	46.559430	49	39	bedding	Valley 1	1946	
10.119350	46.559430	120	10	lineation	Valley 1	1946	
10.119350	46.559430	50	39	bedding	Valley 1	1946	

10.119350	46.559430	120	10	lineation	Valley 1	1946	
10.119350	46.559430	120	10	lineation	Valley 1	1946	
10.119148	46.559482	44	41	bedding	Valley 1	1946	
10.117230	46.561370	0	0	lineation	Valley 1	1979	
10.117220	46.561714	127	22	bedding	Valley 1	1984	
10.117220	46.561714	318	2	lineation	Valley 1	1984	
10.116950	46.561720	120	24	bedding	Valley 1	1984	
10.116950	46.561720	318	2	lineation	Valley 1	1984	
10.116950	46.561720	115	22	bedding	Valley 1	1984	
10.116950	46.561720	318	2	lineation	Valley 1	1984	
10.117006	46.561784	87	7	bedding	Valley 1	1992	
10.117006	46.561784	102	25	lineation	Valley 1	1992	
10.116879	46.561892			bedding	Valley 1	1992	
10.116831	46.561983	40	22	bedding	Valley 1	1992	
10.116830	46.561920			bedding	Valley 1	1992	
10.116830	46.561920	295	5	bedding	Valley 1	1992	
10.116830	46.561920	100	9	bedding	Valley 1	1992	
10.116830	46.561920	102	25	lineation	Valley 1	1992	
10.116830	46.561920	251	10	bedding	Valley 1	1992	
10.116830	46.561920	222	9	bedding	Valley 1	1992	
10.116830	46.561920	52	16	bedding	Valley 1	1992	
10.116830	46.561920	137	20	bedding	Valley 1	1992	
10.116830	46.561920	93	15	lineation	Valley 1	2003	
10.116950	46.562440	173	15	bedding	Valley 1	2003	
10.116950	46.562440	93	15	lineation	Valley 1	2003	
10.116902	46.562487	93	15	lineation	Valley 1	2003	
10.116902	46.562487	143	8	bedding	Valley 1	2003	
10.116868	46.562487	91	14	bedding	Valley 1	2003	
10.116769	46.563145	101	15	lineation	Valley 1	2010	
10.116604	46.563128	100	20	lineation	Valley 1	2010	
10.116580	46.563050	73	10	foliation	Valley 1	2010	
10.116580	46.563050	100	20	lineation	Valley 1	2010	
10.116580	46.563050	101	15	bedding	Valley 1	2010	
10.116580	46.563050	100	20	lineation	Valley 1	2010	
10.116580	46.563050	101	15	lineation	Valley 1	2010	
10.116021	46.563050	102	8	foliation	Valley 1	2010	
10.116021	46.563050	100	24	foliation	Valley 1	2010	
10.116248	46.563364	114	20	lineation	Valley 1	2017	
10.116248	46.563364	78	48	bedding	Valley 1	2017	
10.116190	46.563284	55	40	bedding	Valley 1	2017	
10.116140	46.563320	55	40	bedding	Valley 1	2017	
10.116140	46.563320	54	40	bedding	Valley 1	2017	
10.116140	46.563320	114	20	lineation	Valley 1	2017	
10.116021	46.563305	46	30	bedding	Valley 1	2017	
10.115976	46.564095	307	10	lineation	Valley 1	2018	

10.115940	46.563983	289	6	bedding	Valley 1	2018	
10.115870	46.564020	282	21	bedding	Valley 1	2018	
10.115870	46.564020	307	10	lineation	Valley 1	2018	
10.115870	46.564020	291	17	bedding	Valley 1	2018	
10.115870	46.564020	284	18	bedding	Valley 1	2018	
10.115870	46.564020	307	10	lineation	Valley 1	2018	
10.116114	46.563511	306	13	bedding	Valley 1	2020	
10.115960	46.563530	350	11	bedding	Valley 1	2020	
10.115960	46.563530	360	11	bedding	Valley 1	2020	
10.116033	46.563352	147	48	bedding	Valley 1	2024	
10.116020	46.563280	154	56	bedding	Valley 1	2024	
10.116020	46.563280	133	58	bedding	Valley 1	2024	
10.115932	46.563253	161	50	bedding	Valley 1	2024	
10.116043	46.564341	196	88	foliation	Valley 1	2024	
10.115760	46.564280	10	80	foliation	Valley 1	2024	
10.115760	46.564280	135	22	lineation	Valley 1	2024	
10.115760	46.564280	314	3	lineation	Valley 1	2024	
10.115760	46.564280	9	78	foliation	Valley 1	2024	
10.115760	46.564280	135	22	lineation	Valley 1	2024	
10.115760	46.564280	135	22	lineation	Valley 1	2024	
10.115695	46.564434	314	3	lineation	Valley 1	2024	
10.114035	46.396169	280	30	lineation	Valley 1	2024	
10.113989	46.396022	218	51	foliation	Valley 1	2024	
10.113930	46.396000	345	51	foliation	Valley 1	2024	
10.113930	46.396000	221	61	foliation	Valley 1	2024	
10.113930	46.396000	280	30	lineation	Valley 1	2024	
10.113930	46.396000	347	58	foliation	Valley 1	2024	
10.113930	46.396000	219	66	foliation	Valley 1	2024	
10.113930	46.396000	280	30	lineation	Valley 1	2024	
10.113824	46.395924	352	63	foliation	Valley 1	2024	
10.115272	46.565691	130	25	lineation	Valley 1	2051	
10.115192	46.565763	59	27	bedding	Valley 1	2051	
10.115175	46.565781	118	26	bedding	Valley 1	2051	
10.115130	46.565690	118	28	bedding	Valley 1	2051	
10.115130	46.565690	128	22	bedding	Valley 1	2051	
10.115130	46.565690	101	24	bedding	Valley 1	2051	
10.115130	46.565690	130	25	lineation	Valley 1	2051	
10.115130	46.565690	116	27	bedding	Valley 1	2051	
10.115130	46.565690	139	22	bedding	Valley 1	2051	
10.115107	46.565738	107	37	bedding	Valley 1	2051	
10.115090	46.565698	142	12	bedding	Valley 1	2051	
10.115090	46.565698	130	25	lineation	Valley 1	2051	
10.115046	46.565832	118	25	bedding	Valley 1	2051	
10.114984	46.565687	135	26	bedding	Valley 1	2051	
10.115086	46.565535	63	23	bedding	Valley 1	2051	

10.114794	46.566074	9	21	bedding	Valley 1	2067	
10.114762	46.566095	13	24	bedding	Valley 1	2067	
10.114740	46.566070	153	25	bedding	Valley 1	2067	
10.114740	46.566070	12	24	bedding	Valley 1	2067	
10.114761	46.565921	150	26	bedding	Valley 1	2067	
10.113605	46.566653	36	43	bedding	Valley 1	2079	
10.113580	46.566520	5	40	bedding	Valley 1	2079	
10.113580	46.566520	40	40	bedding	Valley 1	2079	
10.113580	46.566520	358	33	bedding	Valley 1	2079	
10.113580	46.566520	359	40	bedding	Valley 1	2079	
10.113580	46.566520	12	38	bedding	Valley 1	2079	
10.113580	46.566520	346	39	bedding	Valley 1	2079	
10.113580	46.566520	357	34	bedding	Valley 1	2079	
10.113578	46.566634	43	37	bedding	Valley 1	2079	
10.113788	46.566848	328	38	bedding	Valley 1	2081	
10.113692	46.566884	343	31	bedding	Valley 1	2081	
10.113670	46.566740	342	33	bedding	Valley 1	2081	
10.113670	46.566740	351	30	bedding	Valley 1	2081	
10.113670	46.566740	355	35	bedding	Valley 1	2081	
10.113670	46.566740	344	22	bedding	Valley 1	2081	
10.113670	46.566740	358	49	bedding	Valley 1	2081	
10.113670	46.566740	19	23	bedding	Valley 1	2081	
10.113670	46.566740	357	28	bedding	Valley 1	2081	
10.113580	46.566643	22	37	bedding	Valley 1	2081	
10.114220	46.567284	334	35	bedding	Valley 1	2100	
10.114147	46.567394	331	22	bedding	Valley 1	2100	
10.114090	46.567270	320	25	bedding	Valley 1	2100	
10.114090	46.567270	354	35	bedding	Valley 1	2100	
10.114090	46.567270	343	25	bedding	Valley 1	2100	
10.114090	46.567270	328	26	bedding	Valley 1	2100	
10.114063	46.567289	322	31	bedding	Valley 1	2100	
10.114044	46.567438	0	25	bedding	Valley 1	2100	
10.114042	46.567252	15	47	bedding	Valley 1	2100	
10.112280	46.566942	23	8	bedding	Valley 1	2102	
10.112240	46.566920	25	13	bedding	Valley 1	2102	
10.112240	46.566920	42	15	bedding	Valley 1	2102	
10.112240	46.566920	16	15	bedding	Valley 1	2102	
10.114219	46.567603	299	23	bedding	Valley 1	2107	
10.114209	46.567599	337	39	bedding	Valley 1	2107	
10.114178	46.567516	334	29	bedding	Valley 1	2107	
10.114080	46.567510	336	31	bedding	Valley 1	2107	
10.114080	46.567510	337	30	bedding	Valley 1	2107	
10.113954	46.567488	350	34	bedding	Valley 1	2107	
10.113943	46.567561	334	28	bedding	Valley 1	2107	
10.113858	46.567489	308	26	bedding	Valley 1	2107	

10.110738	46.567560	5	26	bedding	Valley 1	2147	
10.110670	46.567581	3	25	bedding	Valley 1	2147	
10.110530	46.567550	3	26	bedding	Valley 1	2147	
10.110530	46.567550	5	26	bedding	Valley 1	2147	
10.110530	46.567550	14	39	bedding	Valley 1	2147	
10.110487	46.567685	48	21	bedding	Valley 1	2147	
10.110401	46.567595	5	26	bedding	Valley 1	2147	
10.110514	46.567392	20	20	bedding	Valley 1	2147	
10.122206	46.555514	79	26	foliation	Valley 1	1881	TS 1 oben
10.122206	46.555514	74	24	lineation	Valley 1	1881	TS 1 Lineation
10.115510	46.564500	0	26	bedding	Valley 1	2054	TS 2 oben S plane
10.115510	46.564500	263	11	lineation	Valley 1	2054	TS 2 Lineation
10.115960	46.563530	350	11	bedding	Valley 1	2020	TS 3 oben
10.115960	04.656353	260	3	lineation	Valley 1	2020	TS 3 lineation
10.116140	04.656332	55	40	bedding	Valley 1	2017	TS 4 oben
10.116140	04.656332	114	20	lineation	Valley 1	2017	TS 4 oben lineation
10.116950	04.656244	83	15	bedding	Valley 1	2003	TS 5 oben
10.116950	04.656244	93	15	lineation	Valley 1	2003	TS 5 oben lineation
10.116950	04.656172	120	24	bedding	Valley 1	1984	TS 6 oben
10.116950	04.656172	318	2	lineation	Valley 1	1984	TS 6 oben lineation
10.119350	04.655943	49	39	foliation	Valley 1	1946	TS 7 oben
10.119350	04.655943	120	10	lineation	Valley 1	1946	TS 7 oben lineation
10.121959	46.555577	80	26	bedding	Valley 1	1882	
10.122276	46.555509	110	16	bedding	Valley 1	1881	
10.122644	46.555158	101	46	bedding	Valley 1	1881	
10.116232	46.555787	8	29	bedding	Valley 1 - Valley 2	2040	
10.116020	46.555820	20	26	bedding	Valley 1 - Valley 2	2040	
10.116020	46.555820	18	26	bedding	Valley 1 - Valley 2	2040	
10.113772	46.556070	53	37	bedding	Valley 1 - Valley 2	2076	
10.113700	46.555940	53	38	bedding	Valley 1 - Valley 2	2076	
10.113700	46.555940	30	51	bedding	Valley 1 - Valley 2	2076	
10.113600	46.555990	17	21	bedding	Valley 1 - Valley 2	2079	
10.113531	46.555968	94	6	bedding	Valley 1 - Valley 2	2079	

10.113496	46.556009	31	32	bedding	Valley 1 - Valley 2	2079	
10.113580	46.556062	130	41	bedding	Valley 1 - Valley 2	2084	
10.113550	46.556020	123	34	bedding	Valley 1 - Valley 2	2084	
10.113504	46.555914	126	37	bedding	Valley 1 - Valley 2	2084	
10.109330	46.559060	96	21	bedding	Valley 1 - Valley 2	2250	
10.109330	46.559060	103	13	bedding	Valley 1 - Valley 2	2250	
10.109289	46.559127	86	25	bedding	Valley 1 - Valley 2	2250	
10.108050	46.559650	320	8	bedding	Valley 1 - Valley 2	2289	
10.107983	46.559675	316	15	bedding	Valley 1 - Valley 2	2289	
10.107907	46.559652	204	1	bedding	Valley 1 - Valley 2	2289	
10.106718	46.561657	135	14	bedding	Valley 1 - Valley 2	2299	
10.106710	46.561600	104	26	bedding	Valley 1 - Valley 2	2299	
10.106710	46.561600	113	32	bedding	Valley 1 - Valley 2	2299	
10.106941	46.561648	108	26	bedding	Valley 1 - Valley 2	2300	
10.106750	46.561690	119	67	bedding	Valley 1 - Valley 2	2300	
10.106750	46.561690	103	20	bedding	Valley 1 - Valley 2	2300	
10.106748	46.561776	34	84	bedding	Valley 1 - Valley 2	2300	
10.106705	46.561577	33	64	bedding	Valley 1 - Valley 2	2300	
10.106494	46.561872	90	10	bedding	Valley 1 - Valley 2	2300	
10.105878	46.562818	320	35	bedding	Valley 1 - Valley 2	2334	
10.105710	46.562830	55	46	bedding	Valley 1 - Valley 2	2334	
10.105710	46.562830	348	41	bedding	Valley 1 - Valley 2	2334	
10.105710	46.562830	55	33	bedding	Valley 1 - Valley 2	2334	

10.105588	46.562788	50	49	bedding	Valley 1 - Valley 2	2334	
10.105648	46.563003	340	30	bedding	Valley 1 - Valley 2	2334	
10.103208	46.560714	187	17	bedding	Valley 1 - Valley 2	2396	
10.103160	46.560850	206	21	bedding	Valley 1 - Valley 2	2396	
10.103123	46.560860	149	24	bedding	Valley 1 - Valley 2	2396	
10.102400	46.561140	161	51	bedding	Valley 1 - Valley 2	2418	
10.102400	46.561140	162	53	bedding	Valley 1 - Valley 2	2418	
10.102400	46.561140	153	53	bedding	Valley 1 - Valley 2	2418	
10.101809	46.562157	143	19	bedding	Valley 1 - Valley 2	2450	
10.101793	46.562073	131	15	bedding	Valley 1 - Valley 2	2450	
10.101730	46.562100	160	20	bedding	Valley 1 - Valley 2	2450	
10.101730	46.562100	148	25	bedding	Valley 1 - Valley 2	2450	
10.101730	46.562100	187	8	bedding	Valley 1 - Valley 2	2450	
10.101713	46.562193	151	24	bedding	Valley 1 - Valley 2	2450	
10.100834	46.561551	94	38	bedding	Valley 1 - Valley 2	2477	
10.100670	46.561450	86	35	bedding	Valley 1 - Valley 2	2477	
10.100287	46.561543	104	43	bedding	Valley 1 - Valley 2	2477	
10.100520	46.561500	143	63	bedding	Valley 1 - Valley 2	2482	
10.100520	46.561500	146	56	bedding	Valley 1 - Valley 2	2482	
10.100452	46.561549	146	78	bedding	Valley 1 - Valley 2	2482	
10.100597	46.561908	35	17	bedding	Valley 1 - Valley 2	2492	
10.100410	46.561790	51	4	bedding	Valley 1 - Valley 2	2492	
10.100410	46.561790	62	30	bedding	Valley 1 - Valley 2	2492	

10.100410	46.561790	99	4	bedding	Valley 1 - Valley 2	2492	
10.100410	46.561790	37	28	bedding	Valley 1 - Valley 2	2492	
10.100333	46.561748	45	41	bedding	Valley 1 - Valley 2	2492	
10.100390	46.562000	59	24	bedding	Valley 1 - Valley 2	2498	
10.100390	46.562000	62	33	bedding	Valley 1 - Valley 2	2498	
10.100277	46.562058	60	23	bedding	Valley 1 - Valley 2	2498	
10.097682	46.554154	130	20	bedding	Valley 2	1881	
10.097682	46.554154	162	14	bedding	Valley 2	1881	
10.097637	46.554055	166	15	bedding	Valley 2	2126	
10.097682	46.554154	102	27	bedding	Valley 2	2129	
10.097682	46.554154	196	26	bedding	Valley 2	2129	
10.097682	46.554154	208	39	bedding	Valley 2	2129	
10.097633	46.554167	208	12	bedding	Valley 2	2130	
10.097567	46.554229	135	26	bedding	Valley 2	2132	
10.097888	46.554183	90	6	bedding	Valley 2	2133	
10.097925	46.554159	61	24	bedding	Valley 2	2135	
10.098044	46.554149	130	23	bedding	Valley 2	2136	
10.097370	46.555970	97	11	bedding	Valley 2	2170	
10.097137	46.555956	66	29	bedding	Valley 2	2185	
10.097370	46.555970	98	11	bedding	Valley 2	2186	
10.097381	46.555966	118	25	bedding	Valley 2	2191	
10.096315	46.556907	210	81	bedding	Valley 2	2212	
10.096249	46.556902	220	80	bedding	Valley 2	2212	
10.092537	46.561445	60	58	bedding	Valley 2	2608	
10.092537	46.561445	80	51	bedding	Valley 2	2608	
10.096315	46.556907	212	83	bedding	Valley 2	2211	
10.096315	46.556907	226	76	bedding	Valley 2	2617	
10.096315	46.556907	55	51	bedding	Valley 2	2617	
10.098250	46.552000	26	84	bedding	Valley 2	2075	
10.098250	46.552000	19	66	bedding	Valley 2	2075	
10.098206	46.552093	218	85	bedding	Valley 2	2075	
10.098154	46.551891	26	76	bedding	Valley 2	2075	
10.098385	46.552419	193	40	bedding	Valley 2	2077	
10.098423	46.552568	197	44	bedding	Valley 2	2077	
10.098286	46.552581	191	44	bedding	Valley 2	2077	
10.098126	46.552672	183	31	bedding	Valley 2	2077	
10.097782	46.553870	123	14	bedding	Valley 2	2120	
10.097768	46.554291	154	8	bedding	Valley 2	2120	
10.097756	46.554160	130	14	bedding	Valley 2	2120	

10.097722	46.554225	176	18	bedding	Valley 2	2120	
10.097710	46.554195	133	22	bedding	Valley 2	2120	
10.097590	46.554200	128	20	bedding	Valley 2	2120	
10.097590	46.554200	151	42	bedding	Valley 2	2120	
10.097683	46.554433	128	24	bedding	Valley 2	2120	
10.098461	46.552684	6	77	bedding	Valley 2	2124	
10.098458	46.552572	204	88	bedding	Valley 2	2124	
10.098401	46.552625	31	85	bedding	Valley 2	2124	
10.098340	46.552700	25	90	bedding	Valley 2	2124	
10.098340	46.552700	35	86	bedding	Valley 2	2124	
10.098340	46.552700	26	86	bedding	Valley 2	2124	
10.098340	46.552700	28	85	bedding	Valley 2	2124	
10.098340	46.552700	25	89	bedding	Valley 2	2124	
10.098340	46.552700	32	65	bedding	Valley 2	2124	
10.098340	46.552700	26	82	bedding	Valley 2	2124	
10.098340	46.552700	36	81	bedding	Valley 2	2124	
10.098340	46.552700	10	72	bedding	Valley 2	2124	
10.098340	46.552700	216	85	bedding	Valley 2	2124	
10.098340	46.552700	211	82	bedding	Valley 2	2124	
10.098289	46.552752	33	88	bedding	Valley 2	2124	
10.098023	46.552661	221	80	bedding	Valley 2	2124	
10.097916	46.554230	141	18	bedding	Valley 2	2127	
10.097837	46.554119	121	19	bedding	Valley 2	2127	
10.097783	46.554225	174	27	bedding	Valley 2	2127	
10.097766	46.554267	151	35	bedding	Valley 2	2127	
10.097750	46.554200	140	16	bedding	Valley 2	2127	
10.097750	46.554200	138	19	bedding	Valley 2	2127	
10.097750	46.554200	138	20	bedding	Valley 2	2127	
10.097750	46.554200	153	19	bedding	Valley 2	2127	
10.097750	46.554200	153	12	bedding	Valley 2	2127	
10.097750	46.554200	128	17	bedding	Valley 2	2127	
10.097750	46.554200	121	20	bedding	Valley 2	2127	
10.097750	46.554200	126	20	bedding	Valley 2	2127	
10.097925	46.554864	144	15	bedding	Valley 2	2132	
10.097800	46.554790	95	19	bedding	Valley 2	2132	
10.097800	46.554790	84	18	bedding	Valley 2	2132	
10.097672	46.554881	84	18	bedding	Valley 2	2132	
10.097940	46.554480	158	17	bedding	Valley 2	2135	
10.097940	46.554480	158	15	bedding	Valley 2	2135	
10.097940	46.554480	150	16	bedding	Valley 2	2135	
10.097927	46.554276	160	18	bedding	Valley 2	2135	
10.097800	46.554780	92	33	bedding	Valley 2	2139	
10.097800	46.554780	77	37	bedding	Valley 2	2139	
10.097800	46.554780	100	39	bedding	Valley 2	2139	
10.097760	46.554760	116	20	bedding	Valley 2	2139	

10.097760	46.554760	112	18	bedding	Valley 2	2139	
10.097749	46.554678	122	22	bedding	Valley 2	2139	
10.097730	46.554860	93	30	bedding	Valley 2	2139	
10.097673	46.554905	116	15	bedding	Valley 2	2139	
10.097750	46.554200	141	15	bedding	Valley 2	2165	
10.097040	46.555180	187	15	bedding	Valley 2	2165	
10.097040	46.555180	201	19	bedding	Valley 2	2165	
10.097439	46.556098	110	17	bedding	Valley 2	2170	
10.097432	46.556028	99	12	bedding	Valley 2	2170	
10.097370	46.555970	121	15	bedding	Valley 2	2170	
10.097127	46.555860	75	13	bedding	Valley 2	2170	
10.096123	46.556899	180	17	bedding	Valley 2	2165	
10.096295	46.556849	190	15	bedding	Valley 2	216	
10.097325	46.555990	100	30	bedding	Valley 2	2191	

Appendix C Instrumentation

Microscopy:

Leica DM2500P

Kamera LEICA DFC750 C

C-Mount 0.70x

Objektiv	**1 Teileinheit**				**Gesamtlänge**				**Untere Bildkante (Photo)**	
1.25	0,16000	mm	160,00	µm	2880,00	µm	2,88	mm	9,86	mm
5	0,04000	mm	40,00	µm	720,00	µm	0,72	mm	2,49	mm
10	0,02000	mm	20,00	µm	360,00	µm	0,36	mm	1,24	mm
20	0,01000	mm	10,00	µm	180,00	µm	0,18	mm	0,62	mm
65	0,00308	mm	3,08	µm	55,38	µm	0,0554	mm	0,21	mm
100	0,00100	mm	1,00	µm	18,00	µm	0,018	mm	0,124	mm

Table can be used for size determination in the thin section with different magnification.

Geological Software:

Allmendinger, R. W. (2026). Stereonet 11. [Software]. Available at: rickallmendinger.net.

QGIS Development Team (2026). *QGIS Geographic Information System*. QGIS Association. http://www.qgis.org

Acknowledgements

First and foremost, I would like to express my sincere gratitude to my supervisor, Prof. Dr. Uwe Ring, for his invaluable guidance, academic support, and insightful comments throughout this project.

I am also very grateful to Prof. Dr. Leander Franz from the University of Basel for his significant contribution to this research. His expert assistance with the thin section analysis was indispensable, and I am especially thankful for the opportunity to utilize the specialized laboratory facilities and microscopy equipment at his department to document the deformation structures.

Furthermore, I would like to thank Stockholm University for providing the opportunity to study Geology through their distance learning program.